Preparation and optical characterization of nanoporous templates as a basis for nanocontact arrays

Von der Fakultät für Elektrotechnik, Informationstechnik, Physik
der Technischen Universität Carolo-Wilhelmina
zu Braunschweig
zur Erlangung des Grades einer
Doktorin der Naturwissenschaften
(Dr. rer.nat.)
genehmigte
Dissertation

von **Hongdan Yan**
aus Rongcheng, China

1. Referentin oder Referent: Prof. Dr. Peter Lemmens
2. Referentin oder Referent: Prof. Dr. Winfried Daum
3. Referentin oder Referent: Prof. Dr. Bernd Güttler
eingereicht am: 22, June 2012
mündliche Prüfung (Disputation) am: 07, August 2012
2012
(Druckjahr)

Vorveröffentlichungen der Dissertation

Teilergebnisse aus dieser Arbeit wurden mit Genehmigung der Fakultät für Elektrotechnik, Informationstechnik, Physik, vertreten durch die Mentorin oder den Mentor/die Betreuerin oder den Betreuer der Arbeit, in folgenden Beiträgen vorab veröffentlicht:

Publikationen

- Yan, H., Lemmens, P., Dierke, H., White, S. C., Ludwig, F. & Schilling, M. Iron/Nickel nanowire growth in anodic aluminum oxide templates: Transfer of length scales and periodicity. J. Phys.: Conf. Series, 145, 012079-1-4 (2009).

- Makhal, A., Yan, H., Lemmens & P., Pal, S. K. Light Harvesting Semiconductor Core-Shell nanocrystals: Ultrafast Charge Transport Dynamics of CdSe-ZnS Quantum Dots. The Journal of Physical Chemistry C, 114, issue 1, 627-632 (2010).

- Yan, H., Lemmens, P., Wulferding, D., Shi, J., Becker, K. D., Lin, C. T., Lak, A. & Schilling, M. Tailoring defect structure and optical absorption of porous anodic aluminum oxide membranes. J. Mat. Chem. Phys., 135, 206-211 (2012).

- Makhal, A., Sarkar, S., Yan, H., Lemmens, P., Wulferding, D., Cetin, F.& Pal, S. K. Ultrafast excited state deactivation of doped porous anodic alumina membranes. Nanotechnology, (in print), (2012).

Tagungsbeiträge

Präsentation

- *Artificial magnetic materials grown in nanoscale templates*, International Workshop "Materials for Frustrated Magnetism" within the ESF-Network Highly Frustrated Magnetism, Grenoble, France, 3-5th, March (2008).

- *Preparation and functionalization of porous anodic aluminum oxide templates*, DPG spring meeting, Berlin, 25-29th, February (2008).
- *Optical properties of nanopore arrays based on porous alumina*, DPG spring meeting, Regensburg. 21-26th, of March (2010).
- *Gold-Aluminate Nanostructures: Preparation and Characterization*, NTH Autumn workshop, Hameln, (2010).
- *Preparation of nanostructured materials*, NTH Summer school, Hannover, (2010).

Poster

- *Artificial magnetic and molecular materials grown in nanoscale templates*, the 4th International conference on Highly Frustrated Magnetism, Braunschweig, September, 2008.
- *Transfer of length scales and periodicity of nanowires grown in templates*, DPG spring meeting, Dresden, 22-27th, March, 2009.
- *Nanoscale Porous Alumina Templates: Properties and spectroscopic investigations*, IGSM summer school, 2010.
- *Light - Matter Interaction and molecular emitters in nanotemplates* , 4th International Summer School "Physics of Functional Micro- and Nanostructures" , Hamburg, 13-25th, September, 2010.
- *Plasmon - Polariton modes of dense Au nanowire arrays*, DPG spring meeting, 2011.
- *Tailoring defect structure in nano porous alumina templates*, DPG spring meeting, 2011.
- *Plasmons touch molecules: Spectroscopic investigations*, NTH autumn school, Hannover, 2011.
- *Coupling of plasmons to molecular excitons*, DPG spring meeting, Berlin, 2012.
- *Organophosphonate monolayer functionalization of planar and nano-porous aluminum oxide*, DPG spring meeting, Berlin, 2012.

Contents

List of Figures

List of Tables

Abstract

This thesis describes the preparation and characterization of anodic alumina oxide (AAO) templates and complex nanostructures based on such templates. The aim of our investigation is to achieve materials that allow a pronounced energy transfer following the concept of nanocontacts between the oxide framework, plasmonic metal and molecular components. For this reason free standing as well as ultra thin AAO templates are prepared by a well-controlled, two step anodization process. Hexagonal pore arrangements with honeycomb-like boundaries are formed via a self-organized oxidation process. The effect of tuning parameters, such as temperature, composition and geometry of the etching cell, are systematically investigated. In this way the pore diameter is tunable from 20 nm to 200 nm and template thicknesses from 150 nm to 20 μm are achieved. The physical and chemical properties of the AAO templates evidently influence the characteristics of the resulting nanocomposites and are therefore investigated as function of preparation methods and conditions. The relation between photoluminescence and optical absorption has been studied in detail. The absorption spectra of annealed AAO can be divided into several Gaussian bands located at 4.3 eV, 4.9 eV and 5.4 eV, respectively. These absorption bands originate from different oxygen vacancies (color centers, F^+ and F_2) that also lead to a related photoluminescence (PL). The Stokes shift between these two processes is rather large and attributed to the amorphous structure of the templates. Via annealing the concentration of oxygen vacancies can be controlled leading to nonmonotonical changes of absorption with temperature and time. Nanowire arrays from plasmonic Au wires as well as magnetic materials are grown by electrochemical deposition of metals or oxides in the AAO template. The wire arrays are decorated by molecular species such as Mg-phtalocyanine or Aza-BODIPY. We observe Förster resonance energy transfer (FRET) between AAO and the molecules using the color centers of AAO as a donor. The quenching of PL is further studied using picosecond and femtosecond resolved luminescence measurements. The characteristic life times are tuned by doping with Benzoquinone and CdSe quantum dots. We demonstrate a tailoring of the dynamic optical properties of the complex nanostructures using geometry as well as characteristic energies of the constituents.

Überblick

Die vorliegende Arbeit beschreibt die Herstellung und Charakterisierung von nanoporösen Matrizen, basierend auf anodisiertem Aluminiumoxid (AAO), und komplexen Nanostrukturen. Das Ziel unserer Untersuchungen ist es, Materialien herzustellen, die einen gezielten Energietransfer zwischen nanoskaligen Metallstrukturen, Molekülen, und der umgebenden AAO Matrix erlauben. Daher werden sowohl freistehende als auch ultradünne AAO Matrizen über einen wohl kontrollierten, zwei-Schritt Anodisierungsprozess hergestellt. Hexagonale Porenanordnungen mit wabenförmigen Grenzeflächen werden über eine selbst organisierte Oxidation erreicht. Der Einfluss von Parametern wie Temperatur, Zusammensetzung und Geometrie der Anodisierungskammer auf die Probeneigenschaften wird systematisch untersucht. Auf diese Weise können Nanoporen mit Durchmessern in einem Bereich von 20 nm bis 200 nm und AAO Schichtdicken von 150 nm bis 20 μm erzielt werden. Die physikalischen und chemischen Eigenschaften der AAO Matrizen haben einen starken Einfluss auf die Eigenschaften der daraus resultierenden Nanokomposite und werden daher als Funktion von Herstellungsparametern untersucht. Insbesondere der Zusammenhang zwischen der Photolumineszenz und der optischen Absorption wird im Detail untersucht. Das Absorptionsspektrum von getempertem AAO kann in mehrere Gauss-Banden bei 4.3 eV, 4.9 eV und 5.4 eV aufgeteilt werden. Diese Absorptionsbanden rühren von unterschiedlichen Sauerstoffdefiziten (Farbzentren, F^+ und F_2), die wiederum zu einer Photolumineszenz (PL) führen. Die Stokes-Verschiebung zwischen diesen Prozessen ist relativ groß, was mit der amorphe Struktur der Matrizen erklärt wird. Durch Tempern kann die Konzentration der Sauerstoffdefekte gesteuert werden, was zu nicht-monotonen Änderungen der Absorption mit Temperatur und Zeit führt. Plasmonische Gold-Nanodrähte sowie Nanodrähte aus magnetischen Materialien werden durch elektrochemische Abscheidung von Metallen gezüchtet. Die resultierenden Anordnungen werden mit Molekülen wie Mg-Phtalocyanin oder Aza-BODIPY belegt. Wir können einen Förster-Resonanz-Energie-Transfer Prozess (FRET) zwischen AAO und den Molekülen unter Ausnutzung der AAO Farbzentren beobachten. Weiterhin wird ein Quenchen des Photolumineszenz-Signals beobachtet und mit piko- und femtosekunden aufgelösten Lumineszenz-Messungen erfolgreich charakterisiertn. Die daraus resultierenden Lebensdauern werden durch Dotierung mit Benzoquinon und CdSe-Quantenpunkten gezielt verändert. Wir demonstrieren

ein gezieltes Maßschneidern der dynamischen optischen Eigenschaften von komplexen Nanostrukturen mithilfe der zugrundeliegenden Geometrie sowie der charakteristischen Energien ihrer Bestandteile.

Chapter 1

Introduction

Nanoscale materials and phenomena are fascinating because of their unique properties and functionalities based on, e.g. size effects [1]. Interactions and processes on smallest (i.e. atomic) and mesoscopic length scales can be controlled and manipulated to design novel bulk materials and surfaces. This allows for a systematic preparation of attractive materials instead of discovering them by trial and error. As Nobel prize winner Prof. Roald Hoffmann famously said: "Nanotechnology is the way of ingeniously controlling the building of small and large structures, with intricate properties; it is the way of the future, with incidentally, environmental benignness [sic] built in by design." [1] In this sense, the main goal of nanoscience is the intentional and precise control of structural elements and their interplay.

Nanoporous materials are a prime example of this relation because of their high surface to volume ratio and large porosity. In addition the pore walls may be functionalized. Nanoporous materials of different pore size, porosity, pore distribution, and composition are developed for different potential applications, as [1]:

- High efficiency filtration and separation membranes
- High efficient catalysis
- Porous electrodes
- Hydrogen and energy storage
- Templates for preparation of complex nanostructures.

Periodically ordered nanostructures have attracted a vast amount of scientific attention because of the perfect hexagonal pore arrangement that may be achieved at the surface by comparably inexpensive techniques. The preparation of ordered nanopore and wire arrays allows to form more complex materials, e.g.

core shell and decorated matrices, that have properties which cannot be achieved with simpler systems.

Anodized aluminum oxide (AAO) templates have been studied since 1950, with pioneering work done by Keller et al., who reported the structural features of porous alumina using an electron microscope [2]. In 1995, Masuda and Fukuda have developed a two-step anodization process which results in highly ordered pores [3]. Since then, the formation mechanism and physical properties of AAO and derived materials have been broadly investigated. Used techniques include scanning electron microscopy (SEM), optical absorption spectroscopy, and photoluminescence spectroscopy. AAO as templates offer the possibility to prepare macroscopic amounts of nanoscale materials, such as quantum dots, nanowires and nanotubes [4, 5, 6].

In this thesis we demonstrate the preparation of nanoporous oxidic templates and more complex nano materials with the aim of establishing arrays with coupled molecular/plasmonic degrees of freedom.

The outline of this thesis is as follows:

Following chapter 1, chapter 2 presents the AAO growth mechanism, basic theory of surface plasmons, and molecular excitons.

Chapter 3 focuses on the preparation, characterization of AAO and nanostructured arrays with the AAO as a template. The experimental setups for preparing AAO, quantum dots, and nanowires are introduced as well. Additionally, the characterization techniques for morphology of various AAO and nanostructured arrays are described. Finite element method (FEM) simulation is presented as it describes plasmonic properties of Au nanowire arrays.

Chapter 4 presents the optical properties of porous alumina depending on the annealing temperatures. New results are given for photoluminescence and absorption spectra of annealed AAO based on time resolved studies in the picosecond to femtosecond time range. The formation mechanism of oxygen defects and recrystallization process in AAO are discussed in detail in this chapter.

Chapter 5 presents experimental and simulation results of surface plasmon resonance (SPR) of Au nanowire arrays. Absorption spectroscopy is used to detect the SPR of Au nanowire arrays. The results relate the SPR signals to the size, arrangement, or environment of Au nanowires. We realize these changes by annealing and chemical etching. SPR simulation results of Au nanowire arrays are comparable to the actual experimental results.

Chapter 6 concerns organic molecular states located close to Au nanowires. This results in a coupling by the SPR of Au nanowires. Mg-phtalocyanine and Aza-BODIPY are used in the experiment to detect the related energy transfer.

Chapter 2

Basic theory

2.1 Electrochemical preparation of nanoporous templates

In this chapter we will describe theoretical aspects of the electrochemical preparation of nanostructured materials. This includes chemical reaction paths and the description of parameters that determine the morphology and perfectness of structures. We will describe the properties of surface plasmons and their coupling to external light fields as well as their coupling to molecular excitations of molecular species. Optical properties of oxidic materials and plasmonic structures have been investigated within this thesis. A deeper discussion of the data is given in chapter 3 to 6.

Two types of oxide layers can form on the surface of aluminum depending on the anodizing conditions: a compact barrier type layer and a porous oxide layer. The electrolyte plays a key role in determining which type of layer is formed [2, 7]. The barrier type layer grows in air or in a neutral solution (pH = 5 - 7), such as boric acid, aqueous phosphate solutions and some organic electrolyte [9, 10, 11, 12].

The following equations describe the anodic reaction that takes place in the air:

$$4\mathrm{Al} + 3\mathrm{O_2} \rightarrow 2\mathrm{Al_2O_3} \tag{2.1}$$

$$2\mathrm{Al} + 3\mathrm{H_2O} \rightarrow \mathrm{Al_2O_3} + 3\mathrm{H_2} \quad . \tag{2.2}$$

The porous oxide layer can only grow in a strong acidic electrolyte with an anodizing reaction, for instance, sulfuric, oxalic, phosphoric and chromic acid [2, 8]. The following equations show the reactions on different electrodes.

On the anode, the reaction is given by:

$$2\mathrm{Al} + 3\mathrm{H_2O} = \mathrm{Al_2O_3} + 6\mathrm{H^+} + 6\mathrm{e^-} \quad . \tag{2.3}$$

On the cathode, the reaction equation is given by:

$$6\mathrm{H^+} + 6\mathrm{e^-} = 3\mathrm{H_2} \quad . \tag{2.4}$$

In general, the barrier type layer is extremely thin with a uniform thickness and is dielectrically compact. The porous oxide layer grows from the barrier layer [9, 10, 13, 14, 15], and is in part soluble in the electrolyte. The formation of anodic alumina oxide layers also has been studied in some mixed electrolytes, such as fluorine-containing oxalic acid [16], phosphoric and hypophosphorous acid [17], as well as sulfuric and oxalic acid [18]. These results show the simplicity of achieving a transition between the barrier type layer and the porous oxide layer. In this section, the growth mechanism of anodic alumina oxide layers with highly ordered nanopores is discussed.

Figure 2.1 is an idealized model of an anodic alumina oxide (AAO) template. The cells are hexagonally ordered with uniform size, each cell containing a pore which grows perpendicular to the film surface. A dense barrier layer is located between the porous layer and the aluminum base. In general, the structure is characterized by parameters such as pore size, inter pore distance, pore depth and barrier layer thickness. Depending on experimental results, these parameters are mainly determined by anodizing conditions.

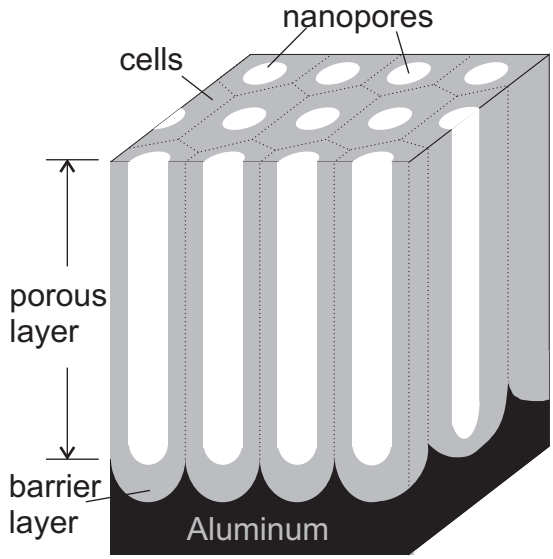

Figure 2.1: The AAO includes three layers: the porous alumina, a barrier layer and an aluminum metal base.

Over the last fifty years, the preparation and application techniques of AAO have been successfully developed, but the formation and growth mechanisms of the pores are still controversial. Several theories have been proposed and developed. For instance, Baumman reported that oxygen ions are generated on the bottom of the pores at the gas/electrolyte interface. Meanwhile, the dissolution of the oxide layer leads to the pore's growth [19, 20]. Keller developed a theory where by a homogeneous barrier film is formed at the beginning of the anodizing process and the dissolution is caused by current, meanwhile the current raises

the local temperature which can enhance the dissolution of the oxide [2]. Murphy and Michelson developed another theory for the oxidation process. They reasoned that the outer side of the barrier layer is transformed into hydroxide and hydrate compounds because of the contact with the electrolyte. This layer can absorb or bond anions from the electrolyte to create a gel-form matrix. The inner layer is a dense oxide layer. Transmission of oxygen anions towards the metal base leads to the oxidation between the inner and the outer layer, and initial pores are formed at defect sites [21].

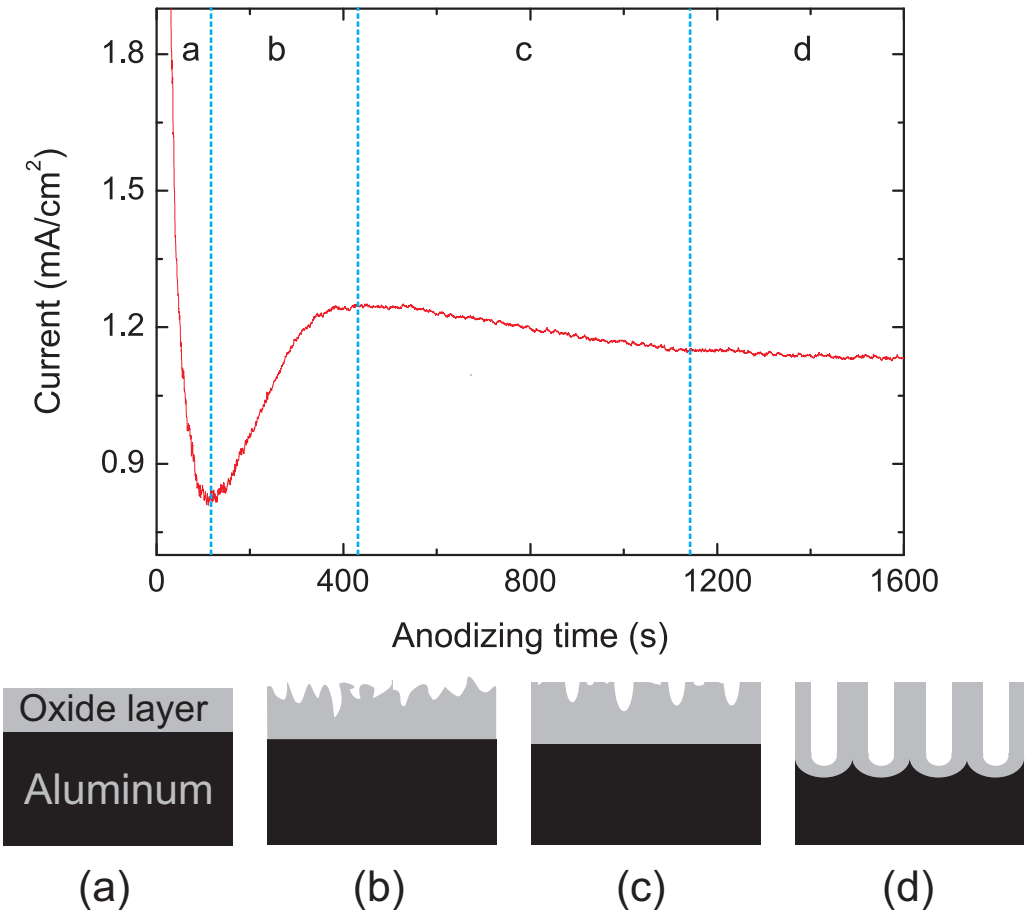

Figure 2.2: A typical anodizing current density achieved in this thesis as a function of time. It is divided into 4 parts corresponding to the anodizing process as shown in the lower schematics. (a) formation of a barrier layer on the aluminum surface; (b) random formation of pore centers; (c) pores deepen and form a new barrier layer on the interface between the metal and the oxide; (d) stable growth of pores.

Figure 2.2 shows a typical anodizing current density as a function of time during the anodization of aluminum in 0.3 M oxalic acid with 40 V anodic voltage

at 0°C.

The evolution of current with time is divided into 4 parts according to different stages of pore formation. When a constant voltage is applied on the surface of the aluminum (stage a), the current decreases with time until the local minimum is reached. Simultaneously a barrier layer grows on the interface of the electrolyte and aluminum, which is non porous with a homogeneous thickness. Subsequently the current increases gradually to a steady point, and pore precursors form on the oxide layer (barrier layer) surface, which can be dissolved in the electrolyte (stage b). The formation of these pore precursors is random, and usually occurs around a defect. Further anodizing and etching results in the growth of pores (stage c), and the aluminum is constantly anodized under an electric field, pores are widened, and at the same time the growth of the barrier layer is increasingly stable. Finally, the growth and the dissolution of the oxide layer reach an equilibrium on the electrolyte-oxide interface and oxide-metal interface [8]. In this stage, the current density is constant (stage d). Anodizing conditions determine the current parameters, such as the minimum current value, the rate of current decrease, and the time after which the steady state forms.

For thermal assisted and field-assisted mechanisms, it is generally accepted that the growth of the barrier film occurs due to the high field ionic conduction, and the porous structures develop from the barrier film [9, 22]. The field strength shows local variations at the surface with defects and impurities. These non-uniform current distributions and local temperatures induce an enhancement of the field-assisted dissolution of the oxide and an increase of the oxide film thickness [22, 23]. With the formation of pores, the current focuses on their base, which can increase pore curvature. Simultaneously, new pores are produced to maintain a uniform field strength across the barrier layer.

The outward migration of Al^{3+} from the metal-oxide interface, and the inward migration of O^{2-} and OH^{-} from the oxide-electrolyte interface lead to the growth of porous alumina. Figure 2.3 shows the migration of elements through the barrier layer [24].

The generation of Al^{3+} mainly contributes to anodic current:

$$Al \rightarrow Al^{3+} + 3e^{-} \quad . \tag{2.5}$$

The formation of O^{2-} and OH^{-} is from the decomposition of water during the anodic process. The O^{2-} can also be from the electrolyte-oxide interface where OH^{-} ions are absorbed by the oxygen vacancies [24],

$$H_2O + 2e^{-} \rightarrow 2OH^{-} + H_2 \quad , \tag{2.6}$$

$$O_2 + 2H_2O + 4e^{-} \rightarrow 4OH^{-} \quad . \tag{2.7}$$

The amorphous alumina grows according to the following equations [8]:

$$2Al^{3+} + 3H_2O \rightarrow Al_2O_3 + 6H^{+} + 6e^{-} \quad , \tag{2.8}$$

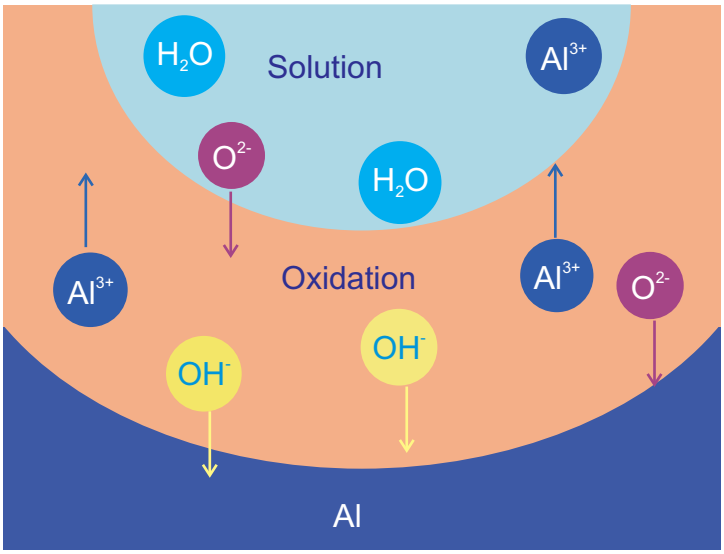

Figure 2.3: The migration of ions through the barrier layer. Al^{3+} ions migrate to the electrolyte; O^{2-} and OH^{-} ions migrate into the barrier layer. [24]

$$2Al + 6OH^{-} \rightarrow Al_2O_3 + 3H_2O + 3e^{-} \quad , \tag{2.9}$$

$$2Al + 3O^{2-} \rightarrow Al_2O_3 + 6e^{-} \quad . \tag{2.10}$$

Masuda and Satoh discovered a two-step anodization process for the preparation of highly ordered arrangements of nanopores in sulfuric, oxalic and phosphoric acid [25]. Before anodization, a series of pretreatment steps are necessary to improve the surface of the aluminum foils. An annealing process reduces stresses between the grains and increases the average grain size [26, 27]. Typical annealing conditions are 400°C - 500°C for 3 - 5 h in air, argon or nitrogen atmosphere. Another important pre-treatment step is polishing the aluminum foil. For different aims, different polishing techniques can be used. Mechanical polishing leads to a smooth surface before anodizing [28, 29, 30], while chemical polishing leads to highly ordered nanostructures [31, 32]. The most commonly used electrolyte for chemical polishing is 60% $HClO_4$: $C_2H_2O_5$ (1 : 4 volume), and the anodizing potential is 18 - 20 V for 4 - 5 min.

For specifically sized nanopores, specific anodizing parameters are required. Table 2.1 includes general electrolytes and experimental conditions [33, 38].

The pore diameter heavily depends on the anodizing potential in a specific electrolyte [8]. The pore diameter is homogeneous at the bottom of the pores, while the diameter close to the surface is larger because of random initial growth

Table 2.1: Anodizing conditions for different pore parameters.

Acid	Anodizing potential range (V)	Optimum potential (V)	Pore diameter (nm)
0.3 M H_2SO_4	10 - 25	25	25
0.3 M $H_2C_2O_4$	30 - 100	40	60
1% H_3PO_4	160 - 195	195	200

of the pores. The pores reorganize in a hexagonal arrangement with increasing anodizing time, but the diameter of pores does not change with anodizing time [2, 14]. According to O'Sullivan and Wood [8], the following equations describe the relation between pore diameter and a constant anodizing potential:

$$\mathrm{D_p} = \mathrm{D_c} - 2 \cdot \mathrm{W} = \mathrm{D_c} - 1.42 \cdot \mathrm{B} = \mathrm{D_c} - 2 \cdot \mathrm{W_u} \cdot \mathrm{U} \ , \tag{2.11}$$

$\mathrm{D_p}$ is the pore diameter, $\mathrm{D_c}$ is the cell diameter, B is the barrier layer thickness, and $\mathrm{W_u}$ is the wall thickness per volt. U is the anodizing potential. The wall thickness is about 71% of barrier layer thickness. Experimentally obtained equations describe the relationship between the interpore distance and anodizing potentials [39, 40]:

$$\mathrm{H_2SO_4}: \ \mathrm{D_c} = 12.1 + 1.99\mathrm{U} \ (\mathrm{U} = 3 - 18\mathrm{V}) \ , \tag{2.12}$$

$$\mathrm{C_2H_2O_4}: \ \mathrm{D_c} = 14.5 + 2\mathrm{U} \ (\mathrm{U} \leq 20\mathrm{V}) \ , \tag{2.13}$$

$$\mathrm{C_2H_2O_4}: \ \mathrm{D_c} = -1.70 + 2.81\mathrm{U} \ (\mathrm{U} \geq 20\mathrm{V}) \ . \tag{2.14}$$

The diameter of pores formed under optimum self-ordering conditions results in an inregular hexagonal arrangement of pores [41]. A high anodizing temperature and the use of a strong acidic solution may enhance the chemical dissolution of the oxide [9, 14], which results in a widening of the pores. Recently, the relationship between pore diameter and anodizing temperature was reported in detail for sulfuric acid [42].

Table 2.2: The pore diameter as a function of anodizing temperature in sulfuric acid at 15 - 25 V. [42]

Potential U (V)	Temperature (°C)	$\mathrm{D_c}$ (nm)
15 - 25	-8	1.06 + 0.8 U
	1	12.35 + 0.53 U
	10	9.34 + 0.72 U

A barrier layer is formed at the pore bottom. It is a dense and compact dielectric layer like an oxide film formed in the atmosphere. The dissolvability and thickness of the barrier layer is very important, because it is related to the further application of the porous nanostructures. For instance, the growth of metal nanowires into pores with a barrier is impossible by electrochemical deposition. Generally, the thickness depends on the anodizing potential (1.15 nm·V^{-1}) [43]. Both wall and barrier thickness can be easily altered by chemically etching, this is known as the pore widening process. Usually, alumina with through pores is prepared by chemically dissolving the barrier layer after removing the remaining aluminum metal.

The porosity is defined as the ratio of the surface area occupied by pores to the whole surface area [44]. The following equation defines the porosity of a nanostructure with hexagonally arranged cells:

$$\alpha = \frac{\pi}{2\sqrt{3}} \cdot \left(\frac{\mathrm{D_p}}{\mathrm{D_c}}\right)^2 = 0.907 \cdot \left(\frac{\mathrm{D_p}}{\mathrm{D_c}}\right)^2 \quad . \tag{2.15}$$

The most important factors influencing the porosity of the structure are the anodizing potential and the pH value of the electrolyte. Increasing the anodization potential results in the decrease of the porosity in sulfuric acid, oxalic acid, phosphoric acid and chromic acid [38, 39, 40, 45, 46]. Increasing the anodizing temperature also results in the decrease of the porosity in oxalic acid [47], while the opposite effect has been reported in sulfuric acid [42].

It is reported that for a perfect hexagonal arrangement of nanopores prepared under optimum anodizing conditions, the ratio between pore diameter and interpore distance is about 0.33 - 0.34 [41], which means the porosity is about 10%. The optimum anodizing potentials for sulfuric, oxalic and phosphoric acids are 25, 40 and 195 V, respectively.

2.2 Surface plasmons and molecular excitons

The collective properties of electrons determine many physical and chemical properties of matter. For instance, noble metals have attracted attention since early times because of their specific properties. Their particles were used as pigments to decorate church windows and other goods appliances [48, 49, 50]. Faraday et al. first pointed out that the colors result from colloidal metallic particles. This started scientific research about interaction between free electrons in metals and electromagnetic radiation [51]. In chemistry, when a molecule absorbs a quantum of energy which results in a transition from one electronic state to another excited state, this process is called an exciton. Especially in dye modecules, this transition may lead to an energy transfer between two molecules [52]. In this part, we will introduce the basics of surface plasmons and molecular excitons, as well as the coupling between them.

2.2.1 Theory of surface plasmons

The propagation of a surface plasmon on the metal-dielectric interface is supported by the localized charge density oscillation along the interface [53], which is called surface plasmon polariton (SPP), shown in Figure 2.4. It has attracted great interest in the field of near-field optical spectroscopy [54]. We consider an idealized model consisting of two semi-infinite nonmagnetic media, one metal layer and one dielectric layer. The wavevector of the SPP should be a complex number like in a metal, $k = k_r + ik_i$, since the dielectric constant $\varepsilon(\omega) = \varepsilon_r(\omega)+i\varepsilon_i(\omega)$ is complex, where ε_r is the real part of the dielectric function and ε_i is the imaginary part. Depending on the solution of Maxwell's equations with an absence of a light source [55, 56],

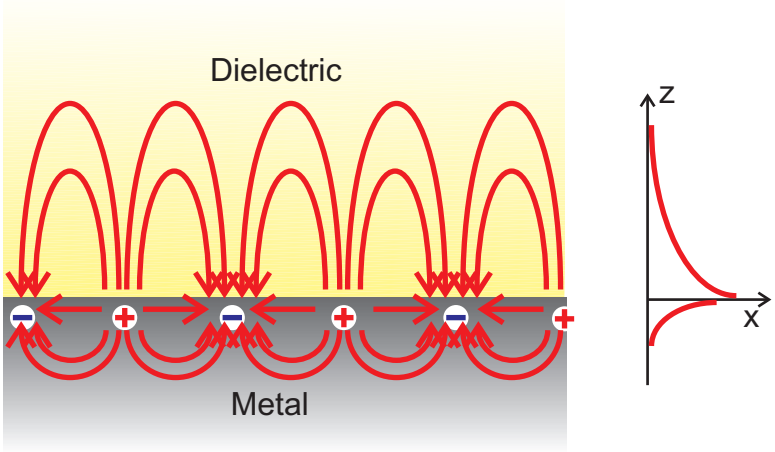

Figure 2.4: The surface charge and electric field distributions associated with the SPP mode. The right figure shows the penetration depth of the field into the dielectric material and into the metal.

$$k = \frac{\omega}{c}\sqrt{\frac{\varepsilon_r\varepsilon_d}{\varepsilon_r+\varepsilon_d}} + i\frac{\omega}{c}\sqrt{\frac{\varepsilon_r\varepsilon_d}{\varepsilon_r+\varepsilon_d}}\frac{\varepsilon_i\varepsilon_d}{2\varepsilon_r(\varepsilon_r+\varepsilon_d)} \quad , \tag{2.16}$$

where ε_d is the dielectric constant of the dielectric medium, the energy position of SPP is determined by k_r, and the propagation length of the SPP along the interface is decaying exponentially and is determined by k_i. The penetration depth of the electromagnetic field into the dielectric medium is of the order of $\lambda/2$ of the wavelength in this medium, however, the depth is given by the skin depth in the metal [55, 56], as seen the left diagram in figure 2.4.

Figure 2.5 shows the dispersion curve of the surface plasmon polaritons. The surface mode is close to the light line at low frequencies and the mode moves further away from the light line upon approaching the surface plasmon resonance frequency ω_{sp}. Directly exciting surface plasmons is impossible because k_{spp} is always larger than k_c. In this case, surface plasmons polaritons can be excited

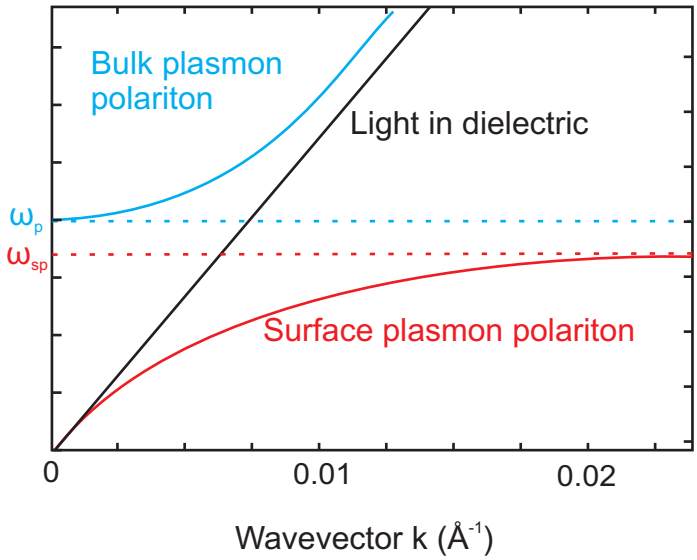

Figure 2.5: The blue line is the dispersion curve of a bulk plasmon polariton, the red line is the dispersion curve of a surface plasmon polariton, and the black line is the dispersion curve of light in a dielectric.

by high energy electrons or by a structure known as a Kretschmann-Raether coupler [57]. Figure 2.6 shows that a metal layer is deposited on the top of a dielectric prism by vapor deposition. The angle of incidence is larger than the angle of total internal reflection. At a certain angle θ, the component of the incident wave vector on the prism-metal interface matches with the SPP wave vector on the air-metal interface, as the wave vector of incident light increases in the prism with a high refractive index n.

For nanoparticles, the polarizability of a sphere α with volume V under an incident light is given by the Clausius-Mossotti relation [58, 59]:

$$\alpha = 3\varepsilon_0 \mathrm{V} \left(\frac{\varepsilon - \varepsilon_\mathrm{d}}{\varepsilon + 2\varepsilon_\mathrm{d}} \right) \ , \tag{2.17}$$

where ε_0 is the dielectric constant of a vacuum and ε_d is the dielectric constant of the surrounding material. ε is the complex dielectric function of the metal. Depending on these equations, the polarizability is infinite when ε_r = -2ε_d [60, 61]. In this case, the charge of nanoparticles creates a density oscillation with the incident light, and results in a resonance with the electromagnetic field of the light, which is termed surface plasmon resonance (SPR). For noble metals (gold, silver and copper) SPR takes place in the visible frequency region [48, 49]. The electromagnetic fields are strongly enhanced around the particles due to the plasmon resonance, and this plasmonic near-field can affect the properties of materials in close proximity to the particles. For instance, it was used in surface enhanced Raman spectroscopy (SERS) [62, 63]. The parameters size, shape and surrounding

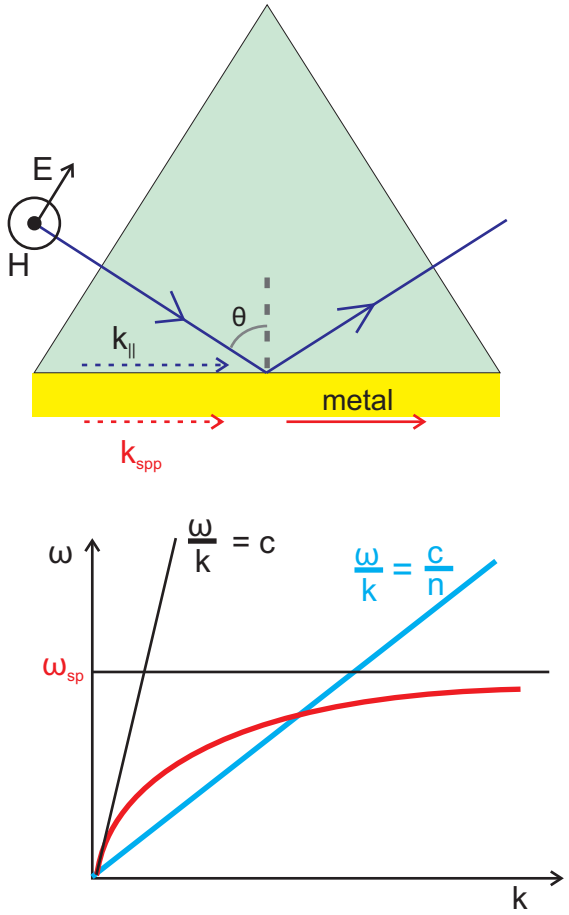

Figure 2.6: Kretschmann configuration of an attenuated total reflection setup for coupling surface plasmon. The plasmons propagate along the interface of metal and dielectric medium. The lower graph shows the increase of the wave vector of the incident light with the assistance of high refractive index of prism.

medium strongly influence the oscillation energy [65, 66, 67] in optical spectra. It also means that the optical properties of plasmonic nanoparticles can be tuned by changes in their size, shape and morphology.

The charge oscillations under an incident electromagnetic field induce a separation between free electrons and the ionic metal core, which results in a restoring Coulomb force. In UV-Vis spectroscopy, the SPR oscillation shows a strong absorption of light at specific energies, which is the origin of the color of the particles as explained by Mie [68]. In the case of nanorods, electron oscillations can take place in two directions, depending on the incident light: transverse (T-mode) and longitudinal (L-mode).

The dielectric constant of a metal is described according to the Drude-Sommerfeld model [69]:

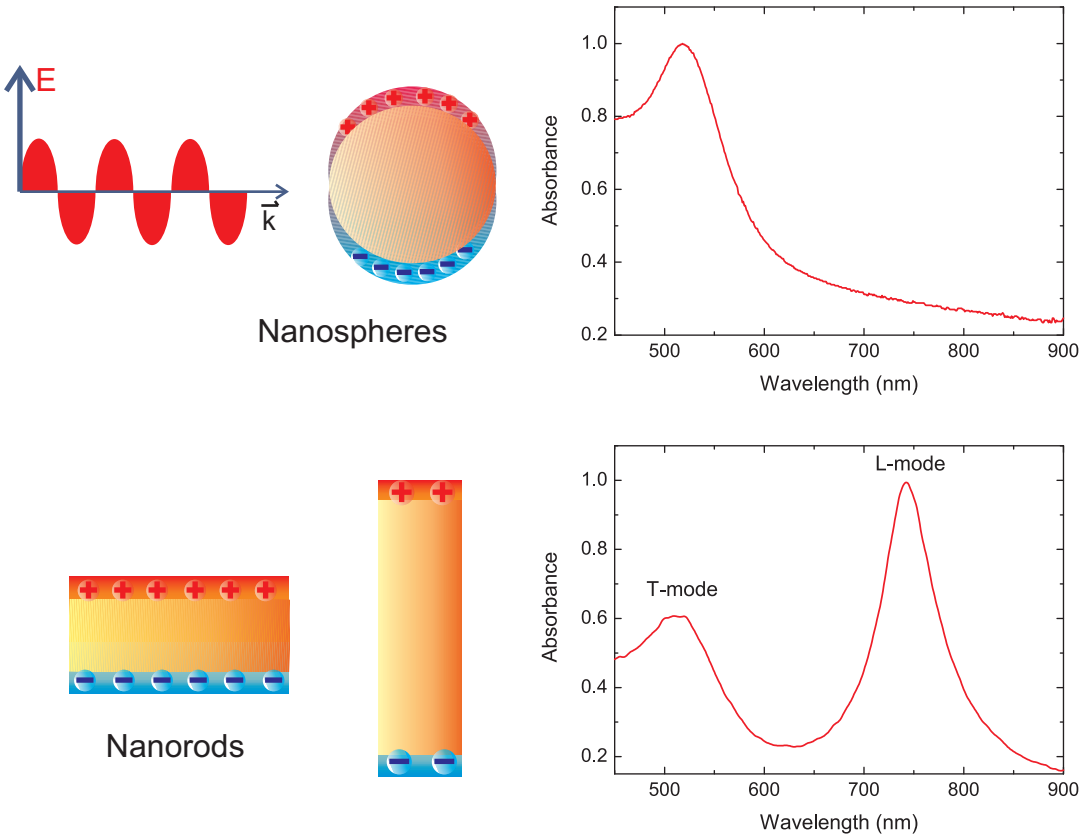

Figure 2.7: Left side: Electronic coherent surface plasmon resonance (SPR) oscillation on the surface of Au nanospheres and nanorods. Right side:F Absorbance spectra of nanospheres and nanorod arrays. Details of geometry and measurement techniques are given in chapter 5.

$$\varepsilon(\omega) = 1 - \frac{\omega_p^2}{\omega^2 + \gamma^2} + i\frac{\gamma\omega_p^2}{\omega(\omega^2 + \gamma^2)} \quad , \tag{2.18}$$

where ω_p is the volume plasma frequency [70, 71], and γ is the damping constant. For bulk gold $\omega_p = 13.8 \cdot 10^{15}\ s^{-1}$ and $\gamma = 1.075 \cdot 10^{14}\ s^{-1}$ [51].

$$\omega_p = \sqrt{\frac{ne^2}{m_e \varepsilon_0}} \quad , \tag{2.19}$$

The real part of the dielectric constant is negative and the value is decreasing with decreasing frequency ω. The surface plasmon absorption band for gold nanoparticles with a diameter of 14 nm is at around 520 nm and for silver nanoparticles with a diameter of 16 nm it is at around 410 nm. The surface plasmon resonance frequency is given by the following equation [72]:

$$\omega_{\mathrm{sp}} = \sqrt{\frac{\mathrm{Ne}^2}{\mathrm{m_e}\varepsilon_0(\varepsilon_\infty + 2\varepsilon_\mathrm{m})}} \quad . \tag{2.20}$$

It is determined by the real part of the dielectric function, while the absorption contribution and line width of the surface plasmon resonance band are determined by the imaginary part of the dielectric constant [72]. The mean free path of electrons in metallic nanoparticles is much smaller than in the bulk. Therefore, the scattering of the electrons by the nanoparticles surface plays an important role in the study of surface plasmon resonance [61]. For instance, when particles are smaller than 10 nm, the resonance line is broadened. The width is inversely proportional to the size diameter [61, 73]. The following equation gives the linewidth of the surface plasmon resonance of a metallic nanoparticle [73]:

$$\Delta\omega_{\frac{1}{2}} \approx \frac{2\varepsilon_\mathrm{i}\mid_{\mathrm{sp}}}{(\mathrm{d}\varepsilon_\mathrm{r}/\mathrm{d}\omega)\mid_{\mathrm{sp}}} \quad . \tag{2.21}$$

Hence, the imaginary part of the dielectric function represents a metal dependent "loss factor" [73]. The plasmonic quality is used to describe the combined effect of the real and imaginary part of the dielectric function. It is given by the energy position of the plasmon resonance divided by its linewidth. Silver has a higher plasmon quality than gold, because much stronger plasmon fields are produced in silver [74]. However, gold is very often chosen in order to study the surface plasmon experimentally, because of its higher stability against oxidation.

The size of nanoparticles has a strong influence on the SPR behavior. As the size increases, the number of electrons increases proportionaly to the volume, and higher-order oscillation modes are excited when the size is comparable to the incident wavelength [58]. The plasmon resonance is significantly broadened by the higher order modes because of a reduction in the phase coherence [61]. Meanwhile, the scattering contribution increases as the particle size increases, while the plasmon lifetime decreases [58]. These effects are shown in the absorption spectra where the plasmon resonance band shows a red shift and a broadening [61, 75].

The maximum peak position of the SPR in the absorption spectra depends not only on the dielectric constant of the metal and its environment, but also on the particle's shape. There is a restoring Coulomb force between a displacement of the conduction electron cloud [58] and the positive metallic lattice under the influence of the electromagnetic field. The magnitude of this restoring force is related to the shape of the electron cloud and the incident polarization. Considering an ellipsoidal particle, the restoring force on the electron cloud along the light polarization direction is weaker than that of a sphere. The shape polarizability is given by [53]:

$$\alpha = \frac{\varepsilon_0 \mathrm{V}}{\mathrm{L}} \left(\frac{\varepsilon - \varepsilon_\mathrm{m}}{\varepsilon + \left(\frac{1+\mathrm{L}}{\mathrm{L}}\right)\varepsilon_\mathrm{m}} \right) \quad , \tag{2.22}$$

L depends on the shape and is a depolarization factor. In a sphere, L=$\frac{1}{3}$. The plasmon resonance condition is given as [53]:

$$\varepsilon_{\mathrm{r}} = -\left(\frac{1-\mathrm{L}}{\mathrm{L}}\right)\varepsilon_{\mathrm{m}} \quad . \tag{2.23}$$

Ellipsoidal and rod-shaped nanoparticles have a long axis A and a short axis B. This results in two SPR modes along two different directions, as shown in Figure 2.7. The values of the depolarization factors depend on the aspect ratio B given as [76]:

$$\mathrm{L_A} = \frac{1-\mathrm{e}^2}{\mathrm{e}^2}\left(\frac{1}{2\mathrm{e}}\ln\frac{1+\mathrm{e}}{1-\mathrm{e}} - 1\right) \quad , \tag{2.24}$$

$$\mathrm{L_B} = \left(\frac{1-\mathrm{L_A}}{2}\right) \quad , \tag{2.25}$$

with e = $\sqrt{1-(1/B)^2}$. Compared to $\mathrm{L_B}$, $\mathrm{L_A}$ is more sensitive to the aspect ratio. With the increase of B, $\mathrm{L_A}$ decreases sharply, which leads to a red-shift of the longitudinal mode. Hence, the SPR energy is tunable in the visible and near-infrared region by the shape of the nanoparticles [76]. Many applications in biology and chemistry depend on this unique property [77, 78, 79]. The intensity of the electromagenetic field $|\mathrm{E}|^2$ is enhanced strongly by the sharp peaks which support a strong near-field plasmon. For instance, the $|\mathrm{E}|^2$ from silver nanorods with an aspect ratio of 2.8 is 4500, compared to a value of 200 from silver nanosphere with a diameter of 20 nm [80].

For the preparation of the nanostructure, chemical synthetic methods [77, 78] and optical lithography [81] are chosen depending on the specific parameters.

2.2.2 Molecular energy levels

In quantum physics, the Schrödinger equation describes the origin of discrete energy levels of an atom. The Hamiltonian is defined as [82]

$$\mathrm{H} = -\frac{\hbar^2}{2\mathrm{m}}\sum_{\mathrm{j}}\bigtriangledown_{\mathrm{j}}^2 - \mathrm{Ze}^2\sum_{\mathrm{j}}\frac{1}{\mathrm{r_j}} + \sum_{\mathrm{i>j}}\frac{\mathrm{e}^2}{\mathrm{r_{ij}}} \quad , \tag{2.26}$$

It includes three parts, the kinetic energy of the electrons, the Coulomb interaction of the individual electrons, and the Coulomb interaction between the electrons. The quantum numbers take the following values:

The main quantum number

$$n = 1, 2, 3... \quad , \tag{2.27}$$

The orbital momentum

$$l = 0, 1, 2, ...n-1 \quad , \tag{2.28}$$

The magnetic quantum number

$$m = -\mathrm{l}, -\mathrm{l}+1, ...l-1, \mathrm{l} \ , \tag{2.29}$$

Finally, the spin of the electron within each orbital has a possible spin quantum number $\mathrm{m_s} = \pm\frac{1}{2}$.

In an atom with only one electron, i.e., the hydrogen atom, H, there is no Coulomb interaction between the electrons. In a molecular system, however, with many electrons, the solution of the Schrödinger equation is more complex, because the interactions between electrons and the orbitals of increasing energy are populated by pairs of electrons according to the Fermi-Dirac statistics.

The molecular energy E is separated into the following different contributions [83]:

$$\mathrm{E} = \mathrm{E_{trans}} + \mathrm{E_{vib}} + \mathrm{E_{rot}} + \mathrm{E_{elec}} \ , \tag{2.30}$$

$\mathrm{E_{trans}}$ is the translational kinetic energy(i. e. $\frac{1}{2}mv^2$ for the whole molecule); $\mathrm{E_{vib}}$ is the vibrational energy; $\mathrm{E_{rot}}$ is the rotational energy; $\mathrm{E_{elec}}$ is the electronic energy [83]. These contributions are not completely independent from each other, as every electronic state has a number of vibrational levels superimposed on it. Typically the energy hierarchy is given by $\Delta\mathrm{E_{elec}}$>$\Delta\mathrm{E_{vib}}$>$\Delta\mathrm{E_{rot}}$. A photon with an energy equal to the difference in energy between the excited state and the ground state, as shown in Figure 2.8, can excite the electrons. The electronic absorption spectra generally consists of broad bands because there is a range of wavelengths that can lead to a transition.

At room temperature, the majority of the molecules are in the ground state energy S_0. The excited electronic states S_1 and S_2 represent the electronic singlet state and T_1 represents the first electronic triplet state. The energy of the T_1 is lower than the corresponding singlet state S_1. Absorption transitions can occur when the energy of the incident photon is equal to the energy difference between $S_1 \rightarrow S_0$ or $S_2 \rightarrow S_0$. The molecules can be excited to different vibrational levels of the excited state. Vibration relaxation and internal conversion usually follow the excitation process, which leads to the molecular state to the main excited electronic level or an intersystem crossing from the singlet state to the corresponding triplet state. Fluorescence (FL) occurs after the vibrational relaxation; the molecules return to the ground state by emission of a photon. However, most excited molecules lose their excitation energy by heat or through collisions with the surrounding medium to return to the ground state. The intersystem crossing process occurs when the vibrational levels in the singlet and the triplet states overlap. The electrons transfer from an excited singlet to a triplet state. Other radiationless processes contain internal and external conversion. No photons are emitted in these processes, and all the excitation energy transfers to heat.

In the following we describe properties of molecules that have promising optical properties. As this thesis concerns the interaction of plasmonic arrays with molecular electronic degrees of freedom both the mechanism and the interaction

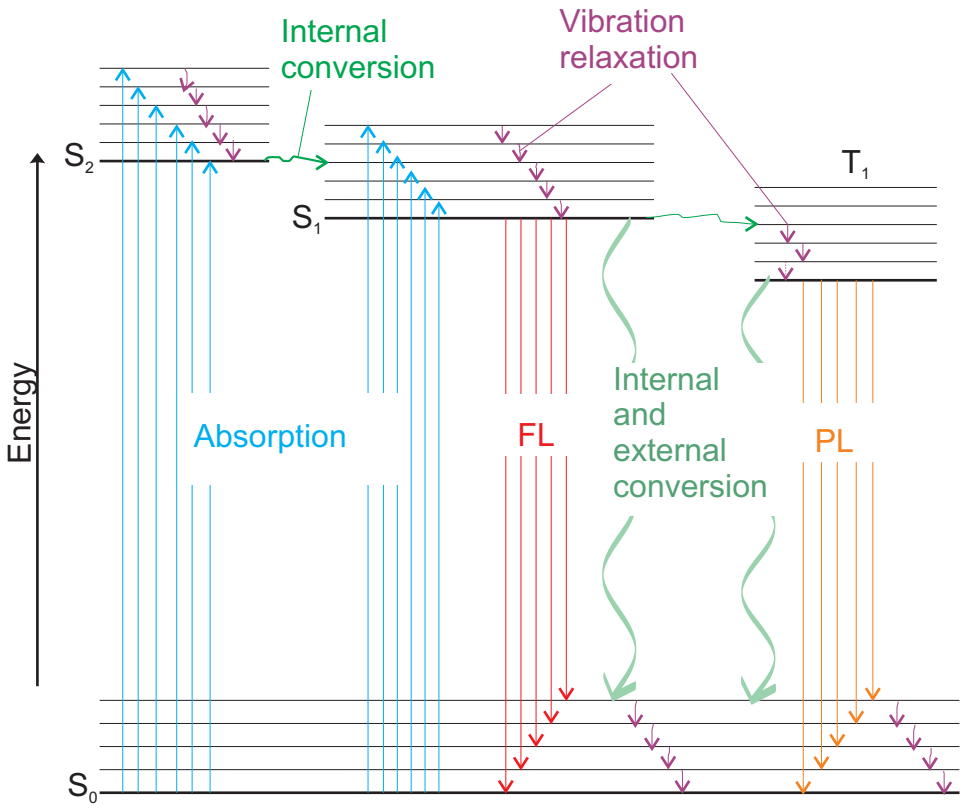

Figure 2.8: Typical diagram for a photoluminescence system. The Jablonski diagram shows a number of possible routes by which an excited molecule can return to its ground or room temperature state.

strength are important. In many cases molecular systems interact with each other or with plasmonic fields via virtual dipole dipole transition. In the field of life science this is often described as Förster resonance energy transfer (FRET). Energy is transferred from a donor to an acceptor molecule. To allow this, the distance should not be too large and a spectral overlap of emission and absorption should exist. Therefore the characteristic energies of molecular systems are very important. The chemical functionality of the molecules can be used to tailor a certain distance in the nanomaterial to be investigated.

As an example we describe here the properties of the dye molecule BODIPY as it has a useful tunability of its excitation levels and is widely available. Samples have been provided by the group of Prof. M. Bröring, IAAC, TU Braunschweig. Other molecules or reactants that have been investigated are Mg-phtalocyanine, benzoquinone, and CdSe quantum dots (Maple red, Evitag). A quantum dot is a nanoscale, crystalline portion of matter with confined excitons. The size of the dot determines the characteristic energy scale of the excitons. They are sometimes called artificial atoms and show a high absorbance at a certain energy.

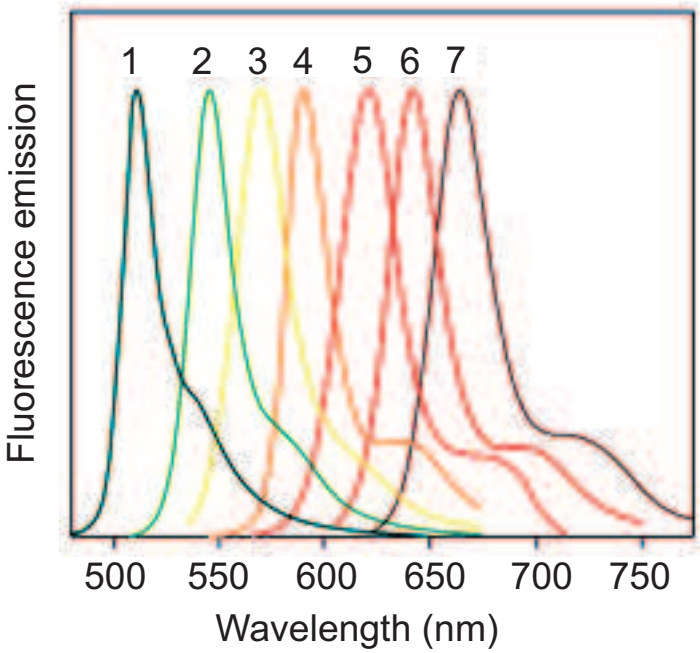

Figure 2.9: Nomalized fluorescence emission spectra of 1) BODIPY FL, 2) BODIPY R6G, 3) BODIPY TMR, 4) BODIPY 581/591, 5) BODIPY TR, 6) BODIPY 630/650, 7) BODIPY 650/665 fluorophores in methanol. [85]

Boron-dipyrromethene (BODIPY) dyes were first discovered by Treibs and Kreuzer in 1968 as a class of fluorescent dyes [84]. Compared to other dyes, BODIPY dyes are extremely versatile because of their specific optical properties can be tuned [85]. Depending on the substituents they can emit in variable fluorescence bands in the visible to near infrared range, as shown in Figure 2.9. The quantum yields can reach up to 100 % even in water. The small linewidth of the emission bands and the high molecular extinction coefficients contribute to overall brightness [85]. BODIPY is used to generate fluorescent conjugates of proteins [86] and fluorescent enzyme substrates [87].

The core structure of the BODIPY fluorophore contains a BF_2 unit, and has green fluorescence. Both fluorescence and absorption spectra shift to lower energies when the suitable substituents allow extended conjugation. Aza-BODIPY (difluoro-bora-1,3,5,7-tetraphenyl-aza-dipyrromethene) dye has been known for more than 15 years [88] as a BODIPY derivative. Their Π systems are affected by introducing heteroaromatic groups in the 1-,3- and 5-,7-positions of the pyrrole ring. Figure 2.10 shows the structures of BODIPY and Aza-BODIPY.

The high chemical stability [89, 90] and tunable infrared absorption [91, 92] of Aza-BODIPY are the key reasons for its wide use in organic solar cell devices [93, 94, 95]. Research on the nature of the interaction between single Aza-BODIPY and inorganic substrates shows the influence of the environment on the

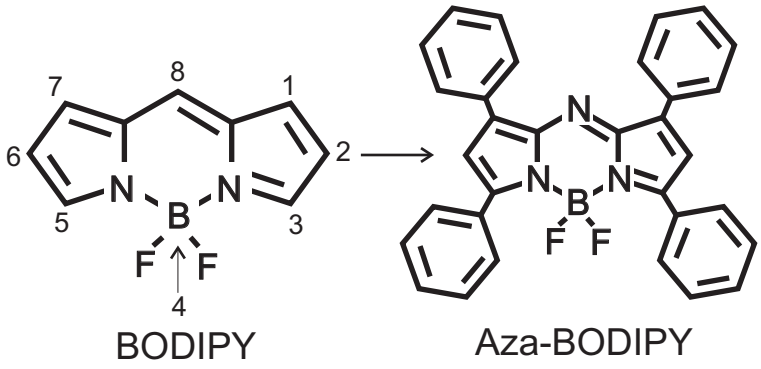

Figure 2.10: Structure of BODIPY and Aza-BODIPY

absorption behavior and the electronic properties of molecules [96]. Scanning tunneling microscopy (STM) investigations show there is no preferred orientation when the Aza-BODIPY is deposited on the Au(111) surface [97]. The unoccupied electronic states in Aza-BODIPY give a broad and intense peak located approximately at 0.7 V [97]. The interaction between the Au surface and molecules results in the phenyl rings rotating, and the BODIPY core is slightly raised compared to the phenyl rings, which leads to conically shaped molecules on the Au surface [97]. DFT-LDA (Density functional theory and Local-density approximation) calculation results prove that charge transformation takes place between Aza-BODIPY and the Au (111) surface, which results in broadened orbitals of the molecules. This is an outstanding property, because Au is a chemically stable metal, usually dye molecules only physisorb on its surface [98, 99].

In this thesis, we deposited Aza-BODIPY on a Au nanowire array. The frequency of the longitudinal plasmon is tuned to the Aza-BODIPY absorption peak at 648 nm via the aspect ratio of Au nanowires. The electromagnetic coupling between molecules and Au nanowires is achieved through a small shift of the longitudinal mode leading to a spectral overlap with the molecular absorption. The overlapping area in the absorption/emission spectra allows a coupling by FRET. We will discuss this effect further in Chapter 4.

Chapter 3

Preparation and characterization: basic techniques

In this chapter we will introduce the preparation techniques of porous alumina based on a two-step anodization process. Vertical and horizontal anodizing cells are compared in terms of their advantages and disadvantages. The preparation processes for free standing and ultra thin AAO templates are individually introduced. Various characterization techniques are introduced in this chapter, which are used to study the morphology and physical properties of AAO. We will also describe the preparation process of nanowires and nanodots based on AAO templates. The SPR simulation method will be introduced at the end of this chapter. Results of the preparation of nanowire arrays in AAO templates have been published [100].

3.1 Experimental setup of template preparation

3.1.1 Vertical anodizing cell

Figure 3.1 shows a vertical anodizing cell. It consists of two glass bottles with a horizontal branch. The bottles are filled with electrolyte and water, respectively. A polished aluminum foil is fixed between the electrolyte and water and used as the anode in the anodizing process. A platinum (Pt) sheet acting as the cathode is inserted in the electrolyte bottle. To stir the electrolytes continuously, a magnetic stirrer is used. This keeps the electrolyte at equilibrium temperature. The whole vertical cell is dipped into a mixture of ice and water, which is constantly at T = 0°C. We connect a computer with a home-made program to the circuit to record the anodizing current and voltage. The used potentiostat/galvanostat has a working range of 0 - 300 V and 0 - 600 mA. The software records voltage and current as a function of time and displays these data on the screen. This record is very important to control the anodization process.

In this cell, the anodizing reaction occurs on the side of the aluminum in con-

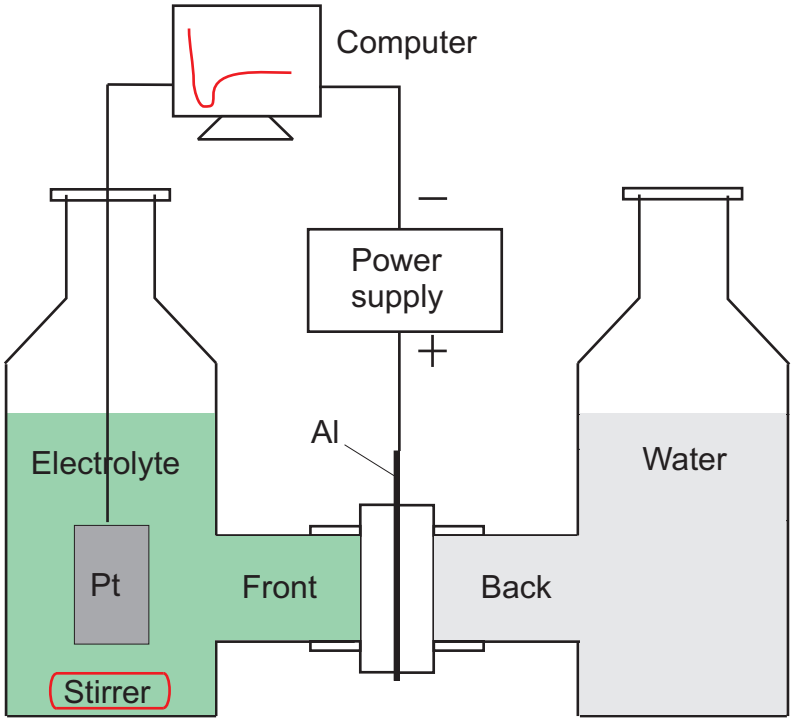

Figure 3.1: Schematic diagram of the vertical anodization cell. The aluminum foil is fixed between two bottles. The left bottle is filled with an electrolyte and the right bottle is filled with water. A platinum sheet is inserted in the electrolyte as a cathode. A magnetic stirrer is used to keep the electrolyte at equilibrium temperature.

tact with the electrolyte, termed "the front side" in our experiment. Before the anodization takes place, the whole cell, with the electrolyte and water is placed in cooling water at 0°C for more than 1 hour to ensure a homogeneous reaction temperature. The platinum plate size is 1 cm×1 cm, and parallel to the aluminum foil to achieve a homogeneous electrical field.

In case of preparing a template with through pores, we have to remove the remaining aluminum and barrier layer on the bottom of the pores. This can be achieved by replacing the water in the right bottle with a dissolving solution, as well as replacing the anodizing electrolyte with distilled water with reagent to keep a constant pressure on both sides of the AAO. When the pores are opened, the water color becomes pink, because the reagent is sensitive to the dissolving acid.

Removing the heat that results from the anodizing reaction is a challenge with the vertical anodizing cell. The junction connecting the two bottles is made from teflon. As a good anti-corrosion material, teflon has a low heat conductance. Huge amounts of heat [32,33] are generated on the bottom of the pores. The templates will burn if the heat removal efficiency is too small. The electrolyte

concentration gradually changes after a long anodization process, even though a magnetic stirrer constantly works during this process. We can clearly see the reagent color changing from the bottom of the bottle to the top. The inhomogeneous electrolyte results in inhomogeneous chemical reactions taking place on the surface of the templates.

3.1.2 Horizontal anodizing cell

We developed a horizontal anodizing cell to overcome the drawbacks of the vertical anodizing cell. Figure 3.2 shows the a sketch of the setup. There are two parts in this apparatus, an anodizing cell and a cooling system. The anodizing cell is filled with the electrolyte, and the polished aluminum foil is fixed on a copper plate. As a cooling system we use a teflon based stirrer driven by a motor to keep the anodizing temperature and electrolyte concentration homogeneous. As a cathode, a platinum mesh is fixed on the opposite side of the aluminum foil. Similar to the vertical anodizing system, a computer is connected with the power supply to record the data during the anodizing process. The cooling system consists of cooling solution, a self-made cooling box and a cooling generator.

As a good thermal conductor, copper can remove the joule heat generated in the reaction effectively. The teflon made cell prohibits a heat exchange with the outside environment. The aluminum foil is installed horizontally to the bottom of the cell, which means that the anodizing temperature and electrolyte concentration are homogeneous on the aluminum surface. For the preparation of large (4 cm$\times$4 cm) porous alumina template with high quality, a horizontal anodizing setup is essential.

3.2 Preparation and morphology of anodic alumina oxide templates

3.2.1 Free standing porous alumina

In our experiments, free standing AAO templates are used to prepare nanowires. The purpose of this section is to describe the preparation conditions of self-assembled porous alumina with variable diameter and aspect ratio.

The preparation of porous alumina is a multistage process consisting of pre-treatment, anodizing, and post-treatment steps. Firstly, the aluminum foil with a high purity of 99.99% is cleaned with acetone in an ultrasonic bath for 30 min to remove contaminations. Then the aluminum foil is annealed in air at 400°C-500°C for 4-5 h to reduce the stress in the material. The electrochemical polishing of the aluminum foil is then carried out in a mixture of $HClO_4$ and C_2H_6O with a volume ratio of 1:4, with polishing parameters of 20 V for 4 min. After polishing, the aluminum surface becomes smooth and shiny.

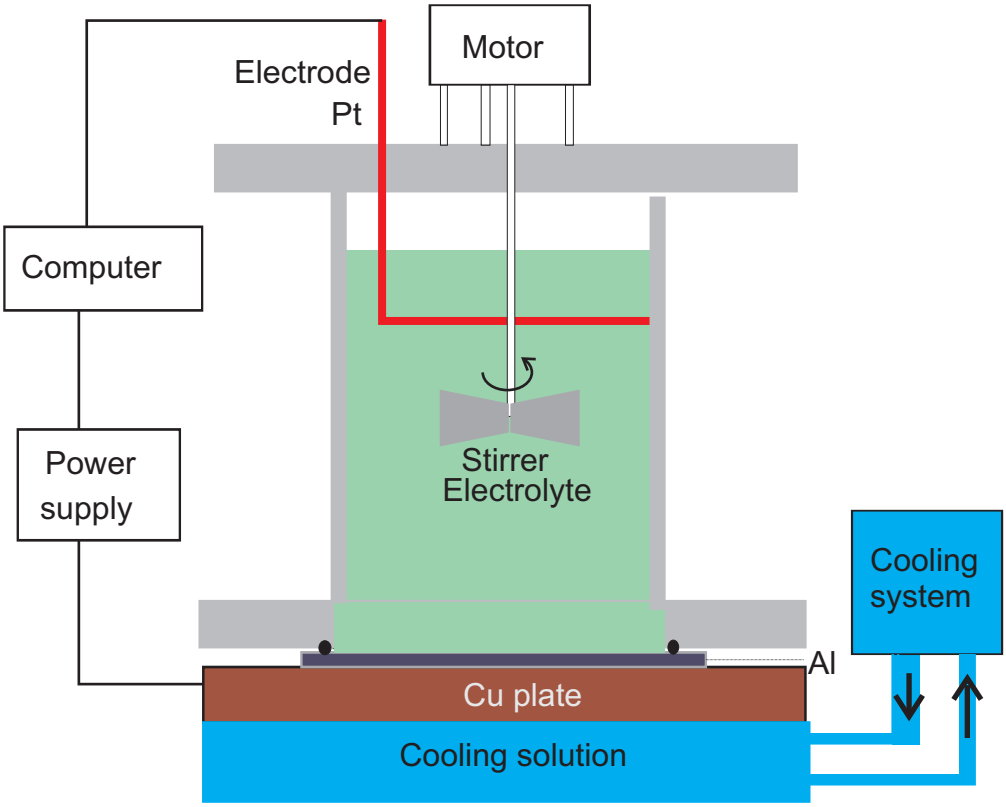

Figure 3.2: Schematic diagram of the horizontal anodizing cell. A motor controlled stirrer is inserted into the electrolyte. As an anode, the aluminum foil is fixed on a Cu plate. The whole cell is fixed on a self-made cooling box which is filled with the cooling solution. A platinum mesh parallel to the aluminum foil acts as the cathode, and a computer is connected to the circuit to record current and voltage.

Before starting the first anodizing process, the electrolyte in the anodizing cell is cooled down to 0°C with the help of our cooling system. In our experiments, sulfuric acid, oxalic acid and phosphoric acid are employed as the anodizing electrolyte. As an example, in the following we will describe the mild anodizing conditions for oxalic acid. The anodizing potential is 40 V. For each electrolyte, there is a certain potential and concentration which can be applied without burning the oxide film. The standard potential and concentration is 25 V for 0.3 M sulfuric acid, and 195 V for 1% phosphoric acid. The self-organized growth of pores happens perpendicular to the surface of the aluminum. The growth rate for the mild anodization process is relatively slow with ≈ 2 nm/s, because of the low current density. However, in a hard anodizing process, the oxide growth rate can reach 1 μm/s, combined with a much higher current density [101]. In this thesis, all templates are prepared by using mild anodization conditions.

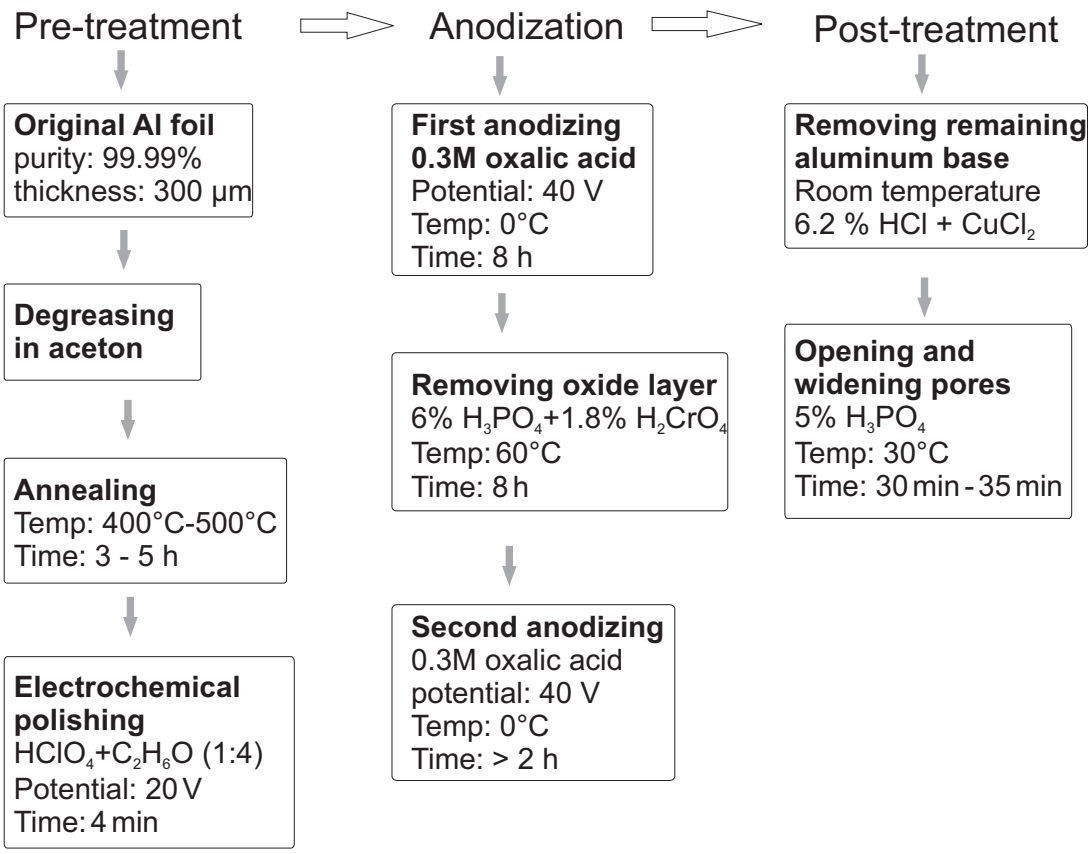

Figure 3.3: Flow diagram of AAO template preparation by a two-step anodization in oxalic acid [102].

In order to get a highly ordered arrangement of pores, the first self-organized porous oxide layer is etched away chemically. This etching process is carried out in a mixed solution containing 6% H_3PO_4 and 1.8% H_2CrO_4 in a water bath at 45°C for 8 hours. The thickness of the oxide layer scales with the etching time. Following the removal of the first oxide layer, the second anodizing process is carried out with the same anodizing potential as a first anodization. The anodizing time varies from 2 - 20 hours depending on the required thickness. For a free-standing template, it usually takes more than 8 hours to finish this process. Otherwise, the template is too thin and fragile to handle. A three-step anodizing procedure can be carried out by repeating the cycles of anodization and removal of the oxide layer [29]. The experimental results show, however, that the order of nanopores is comparable with the two step anodization [29, 102]. Meanwhile, the pore size increases with increasing of anodizing steps [103].

We remove the remaining aluminum base and barrier layer from the non-oxide side to open the pores. This is called the post-treatment process. Firstly, a mixture solution of HCl and $CuCl_2$ is employed to dissolve the aluminum via the

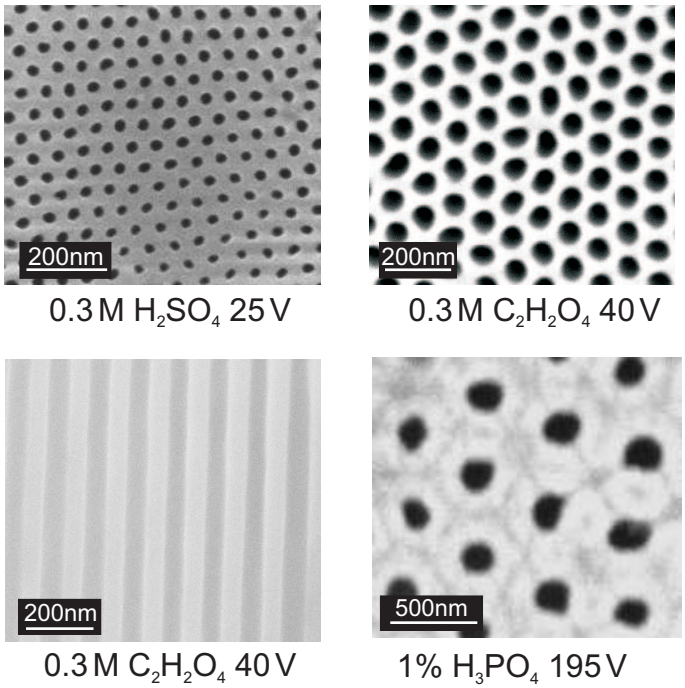

Figure 3.4: SEM pictures of porous alumina. Nanopores were formed by self-organized anodization under different anodizing conditions. The pore diameter and interpore distances are variable depending on the experimental parameters. The lower left picture shows AAO formed in oxalic acid at 40 V.

reaction:

$$3\mathrm{Cu}^{2+} + 2\mathrm{Al} \rightarrow 3\mathrm{Cu} + 2\mathrm{Al}^{3+} \quad . \tag{3.1}$$

The template becomes transparent when all the aluminum is replaced by Cu^{2+}. The barrier layer is removed afterwards with a 5% $\mathrm{H_3PO_4}$ solution. For pores grown in sulfuric, oxalic and phosphoric acid, these processes are carried out at 30°C for 15 min, 30°C for 32 min, and 45°C for 30 min, respectively. In general, with an increasing temperature or etching time, the pores are significantly widened because the walls are dissolved along the horizontal direction. That means that the pore diameters are increasing together with a decrease of inter pore distances. Physical etching techniques, such as Ar^{+} etching can also be employed to remove the barrier layer [104, 105, 106], but the etching time and operation are more complicated than chemical etching.

The structural features of porous alumina anodized in different electrolytes and with varying potentials are shown in Figure 3.4. All SEM measurements were done in Prof. M. Schilling's group, EMG, TU BS. The interpore distance and pore diameter also depend heavily on the anodizing conditions. Adopting the stan-

dard two step anodization process, the pore diameters formed in 0.3 M sulfuric acid, 0.3 M oxalic acid and 1% H_3PO_4 are 20 nm, 60 nm, and 200 nm. Meanwhile, their interpore distances are around 25 nm, 40 nm and 230 nm, respectively. The pores are in a hexagonal arrangement and parallel to each other on the surface, but there are defects at the boundaries between ordered domains [35, 107]. A typical size of domain is 2 μm^2, probably given by domains in the aluminum foil. The defect pores do not have the regular number of six neighboring pores, as correctly formed pores.

3.2.2 Ultra thin porous alumina on Si substrate

In addition to free standing AAO, ultrathin AAO templates are widely used as masks for the preparation of nanoparticle arrays on different substrates [108, 109, 110]. In this thesis, we used two methods to prepare ultra thin AAO on Si substrates in combination with the deposition of nanoparticles.

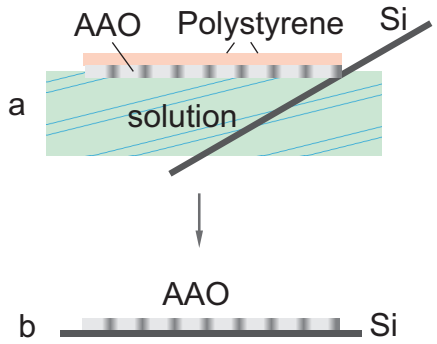

Figure 3.5: Preparation of ultra thin AAO on a Si surface. a) The template is floating on the water surface with the help of polystyrene. The Si substrate is used to take the AAO out; b) the polymer is dissolved by chloroform.

First we will discuss free-standing AAO on a Si substrate. The first anodization process is the same as for the preparation of free standing AAO templates. A highly pure (99.99%) aluminum foil is degreased and annealed in the pretreatment process. Next, the first anodizing process and the removal of the oxidation layer are carried out under different experimental conditions, depending on the requirement for the morphology of nanostructures. The second anodizing process takes a very short time to form an ultra thin oxide layer on the aluminum bases. In order to remove the remaining aluminum metal and barrier layer, a thin layer of polystyrene is spin coated on the surface of the pores. Then the templates can float on the dissolving solution with $CuCl_2$ and HCl. When all aluminum is dissolved, the template becomes transparent and floats. Then the barrier layer is dissolved by the H_3PO_4 solution. The etching time is the same as removing the barrier layer of free standing AAO templates, because the thickness of the barrier

Table 3.1: Anodizing and etching conditions of ultra thin AAO.

Electrolyte	Potential	Anodizing time	Polystyrene concentration	Template thickness
0.3 M H_2SO_4	25 V	90 s -150 s	1.4%	100 nm - 200 nm
0.3 M $C_2H_2O_4$	40 V	120 s - 200 s	1.4%	100 nm - 200 nm
1% H_3PO_4	195 V	20 min	10%	$\approx 1\ \mu$m

layer remains constant when aluminum is anodized at a constant voltage using an acid electrolyte. Following the typical experimental parameters given in Table 3.1 that depend on the anodizing electrolyte.

After opening the pores, the templates are cleaned with distilled water several times and left floating on the water surface. A Si wafer is employed to remove them from the water surface, as shown in Figure 3.5. After the remaining water evaporates in air, the templates stick to the Si surface. Then chloroform is employed to release the pores from the polystyrene film.

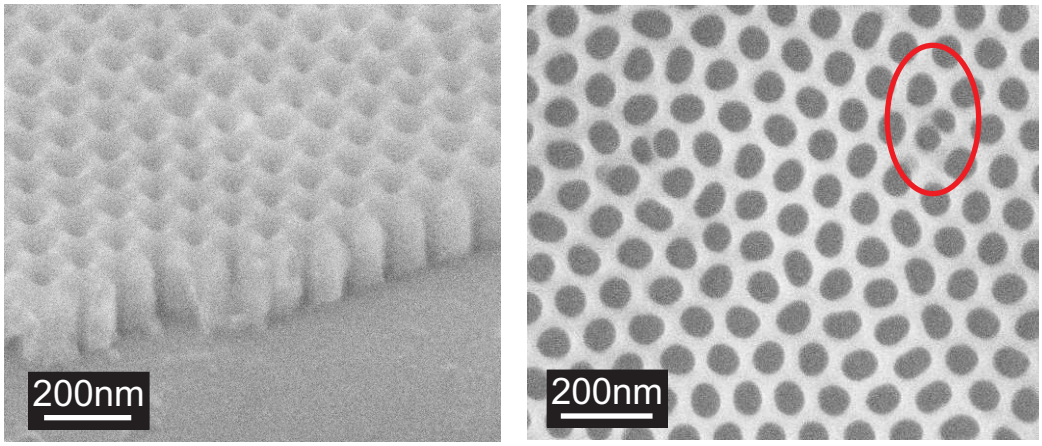

Figure 3.6: SEM pictures of free standing ultra thin AAO on the Si substrate. The template is formed in oxalic acid at 40 V. The left picture shows pores through to the Si substrate with a thickness of around 180 nm. The right picture is a top view of pores on Si, the red circle marks a folded part of the template.

Figure 3.6 shows the morphology of free standing ultra thin AAO on Si substrate. The sample is prepared in 0.3 M oxalic acid at 40 V for 200 s. The top view picture (Figure 3.6 right) shows that the main arrangement of pores is hexagonal as in normal free-standing templates. The disordered pores are caused by not only the boundary of domains, but also the folding of templates as marked by the red line. Because the template is too thin, it might be folded during the rinsing process of dissolving polystyrene. The thickness of this sample is about 180 nm, and the pores are through to the Si surface. Later we will introduce the

preparation of nanodots on a Si substrate by using free standing ultra thin AAO as masks.

Another way to prepare ultra thin AAO on a Si substrate is by directly anodizing AAO on silicon. A highly pure (99.99%) aluminum film is evaporated on the Si(100) surface by electron beam deposition in Prof. A. Waag's group, IHT, TU BS. The thickness of the Al film is 500 nm, which limits the thickness of the AAO. A standard anodizing process is employed. In our experiments, oxalic acid and sulfuric acid are used as the electrolyte, the anodizing potentials are 45 V and 30 V respectively, which is higher than for free standing AAO because of the lower conductivity of the Si wafer. A two-step anodization process is carried out. The time for the first anodization is only 9 minutes, resulting in an aluminum layer of only 500 nm. The second anodization process usually takes around 15 - 20 minutes, until all the metal is anodized. Figure 3.7 shows the anodization current and the anodizing processes in a sketch.

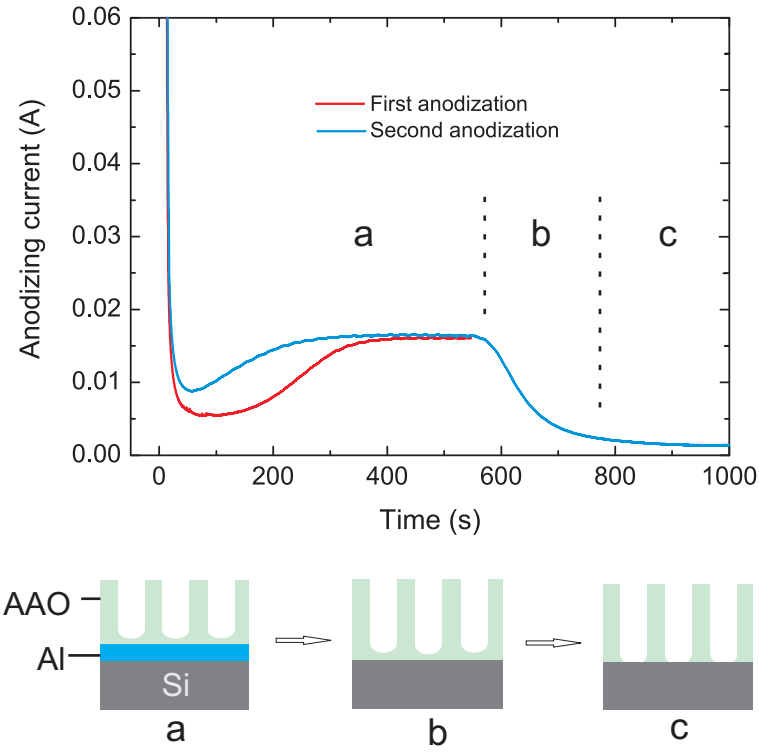

Figure 3.7: The current figure is from the anodization processes of aluminum on a Si substrate: the first (red line) and the second (blue line) are the two anodizing processes. The current evolution from the second anodization process is divided into three parts a, b, c, which correspond to different stages during the anodization process, shown in the lower figure as a sketch.

In the first anodization process (red line), the reaction is stopped when the

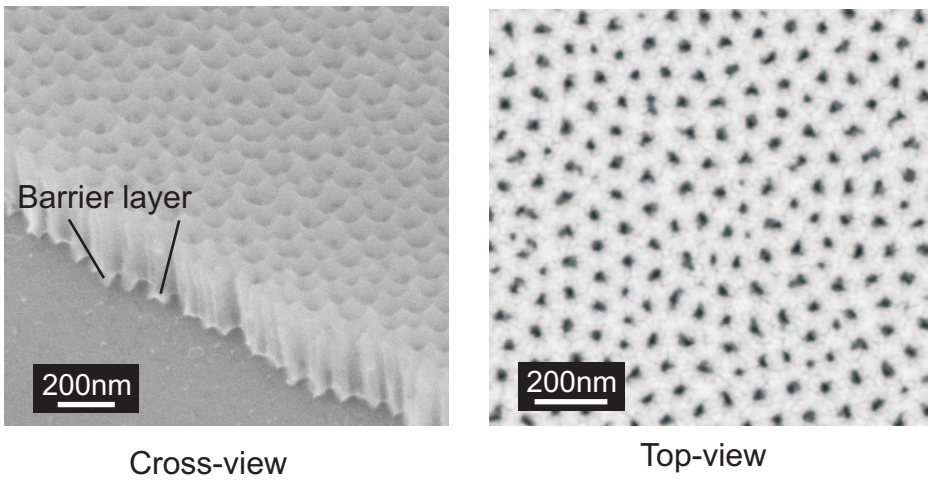

Figure 3.8: The cross view picture shows the thickness of AAO (about 200 nm). The top view shows an inhomogeneous pore arrangement and irregular shapes compared to free standing AAO.

current is constant. In the second anodization process (blue line), the current drops at around 600 s, because all metal is anodized and the barrier layer reaches the Si substrate (process b). The reaction will etch the barrier layer and the pores grow slowly through to the Si wafer (process c). The SEM pictures show the morphology of directly anodized AAO on silicon in Figure 3.8. The thickness of the oxide layer is about 200 nm, the arrangement of the pores is not as ordered as the one in free standing ultra thin AAO. From the cross-view, we can find the remaining barrier layer on the Si surface. The connection between template and Si makes AAO-Si useful for electrochemical deposition techniques. Later we will introduce the preparation of Au nanowires with the directly anodized AAO-Si as a mask.

3.3 Characterization techniques

Several techniques have been used to characterize AAO and nanostructures including metallic and molecular species based on AAO. We mainly used optical spectroscopy (absorption) and electron microscopy (SEM). The optical properties and energy transfer were recorded by the photoluminescence spectra and time resolved photoluminescence. Absorption spectroscopy is used to detect oxygen vacancies in AAO and to investigate surface plasmon excitations of the Au-AAO matrix. Furthermore, Raman spectra and X-ray diffraction were used to investigate the recrystallization processes of AAO and to derive information that allows an improvement of preparation conditions. In addition to scanning electron microscopy also transmission electron microscopy was used to characterize the mor-

phology of the nanostructures. In this section, we will introduce some techniques we have used.

3.3.1 Photoluminescence experiment

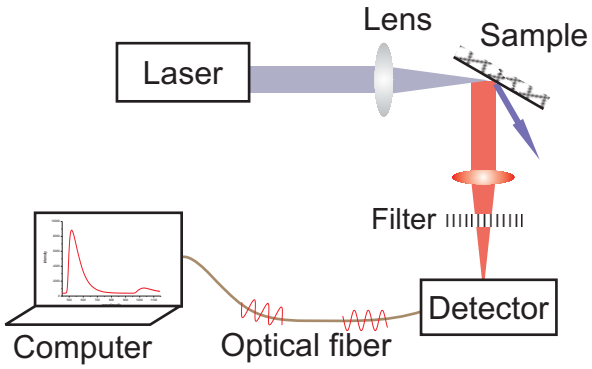

Figure 3.9: Diagram of the photoluminescence experiment.

In a photoluminescence process, photons are focused on the surface of samples, and the incident energy can be absorbed when the photon energy is greater than the band gap of the materials (E > E_g). This leads to a photo-excitation process. The electrons within the samples are excited to higher states, and return to a lower energy state accompanied by the emission of a photon. Photoluminescence spectroscopy is widely used in material science, biochemistry and physics because of the high sensitivity and nondestructive character of this technique.

A photoluminescence experiment consists of an incident laser, a lens, a sample, a spectrometer, a filter, an optical fiber and a computer to record the spectrum, as shown in Figure 3.9. A UV laser with the wavelength 405 nm is used as incident light source, the laser is focused on the sample after passing through several lenses. The photoluminescence signal is collected by a lens and analyzed by a highly sensitive spectrometer (Hamamatsu C9405CA), consistive of optical elements, an image sensor and a drive circuit. The spectral resolution is 1 nm.

3.3.2 Raman scattering experiment

The information obtained from Raman spectra is comparable to that retrieved from IR spectra but complimentary with respect to selection rules. Vibrational modes reveal characteristic information about the material under investigation ("fingerprint") and are, hence, suitable to indentify and quantify these materials. This is in contrast to other optical spectroscopies such as photoluminescence. The disadvantage of Raman spectroscopy is the generally small scattering cross section when compared to, e.g., photoluminescence. This can be overcome, however,

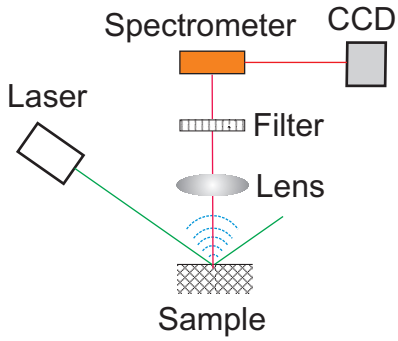

Figure 3.10: Sketch of a Raman scattering experiment [111].

by employing non-linear effects such as phonon-plasmon interactions, for example, using surface enhanced Raman scattering. In a Raman scattering process, incident photons with a frequency ω_i and momentum $\vec{k}_i$ interact with a medium, which leads to scattered photons with ω_s and $\vec{k}_s$, and the scattering medium progresses from an initial state |i> to |f>. The vibrational, rotational and other low frequency modes can be expressed by Raman shifts $\Delta\omega$ in a Raman spectra [112]. Raman scattering is different from photoluminescence with respect to the scattering mechanism. Essentially it is a more rare process with a better defined energy resolution. The formula is given by:

$$\Delta\omega = \omega_{\mathrm{i}} - \omega_{\mathrm{s}} = \left(\frac{1}{\lambda_{\mathrm{i}}} - \frac{1}{\lambda_{\mathrm{s}}}\right) \cdot 2\pi\mathrm{c} \tag{3.2}$$

The basic components of a Raman experimental set up comprise a laser as the light source exciting the inelastic Raman scattering of a sample under investigations, an optical system to collect and separate the Raman signal from the elastically scattered light (Rayleigh scattering), typically a high resolution optical spectrometer and an array detector (CCD) for the detection of the scattered light, as shown in Figure 3.10. In our experiments, the wavelength and power of a frequency-doubled Nd:YAG laser are 532.1 nm and $\mathrm{P_{max}}$ = 20 mW, respectively. Before reaching the sample, the laser light passes through a filter, a polarizer, and a variable slit, producing a well-defined light polarization and accurate power. The well-focused beam forms a spot with a diameter of about 100 μm on the sample. The inelastically scattered light is collected by a lens that focuses the signal onto the entrance slit of a triple grating spectrometer (Dilor XY 500). The Stokes and Anti-Stokes scattered signals are dispersed by this device and guided onto a liquid nitrogen cooled back-illuminated charge-coupled device (Horiba / Jobin Yvon Spectrum one CCD-3000V). The resolution of the spectrometer is 3 - 5 cm^{-1}. For solids, phonons and other excitations are typically located in the range of 30 - 1000 cm^{-1}.

3.3.3 Femtosecond resolved fluorescence spectroscopy

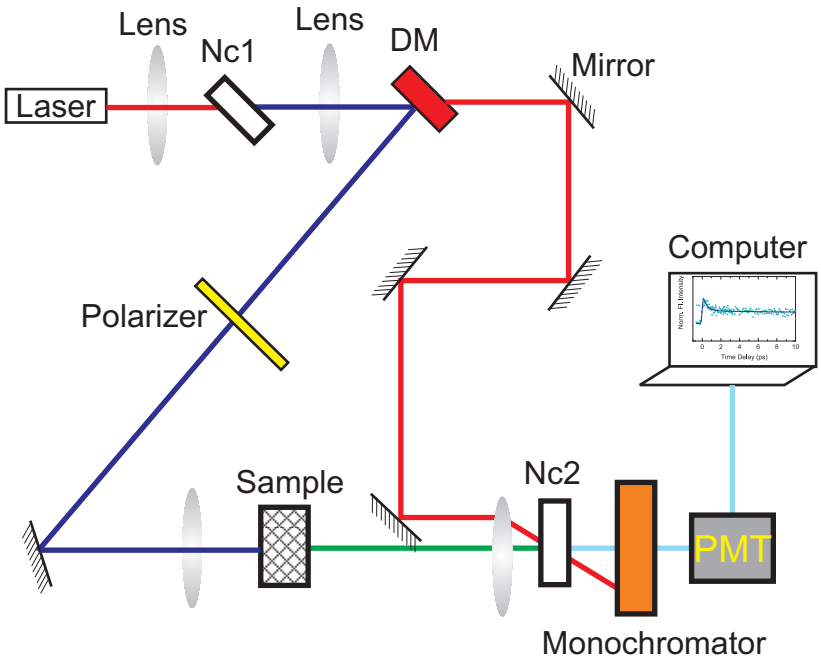

Figure 3.11: Diagram of a femtosecond fluorescence up - conversion experimental setup.

Femtosecond-resolved fluorescence spectroscopy is probed by using a femtosecond upconversion setup (FOG 100, CDP) in which the sample is excited at 375 nm (0.5 nJ per pulse), using the second harmonic of a mode-locked Ti-sapphire laser with an 80 MHz repetition rate (Tsunami, Spectra Physics), pumped by a 10 W Millennia (Spectra Physics). The laser beam is frequency doubled in a nonlinear crystal (Nc1) (1 mm BBO, $\theta = 25°$, $\phi = 90°$). The beam was then focused on the sample after passing through a dichroic mirror (DM) and a mirror. The fluorescence emission was collected and refocused by lenses and mixed with the original laser beam (750 nm) coming through a delay line. Then the fluorescence emitted from the sample is upconverted in a nonlinear crystal (0.5 mm BBO, $\theta = 10°$, $\phi = 90°$) using a gate pulse of the fundamental beam. The upconverted light is dispersed in a double monochromator and detected using photon counting electronics. A cross-correlation function obtained using the Raman scattering from water displayed a full width at half maximum (FWHM) of 165 fs. The femtosecond fluorescence decays are fitted using a Gaussian shape for the exciting pulse. This experiment has been performed in the group of Dr. Samir Pal, SBNC, Kolkata, India.

3.3.4 Absorption spectroscopy

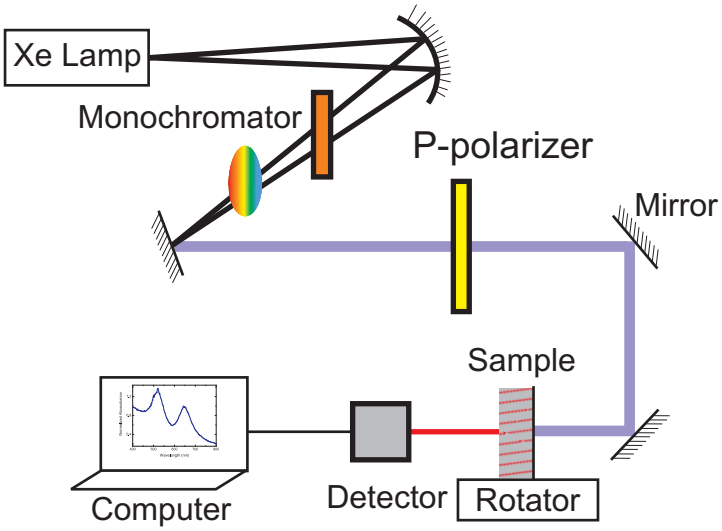

Figure 3.12: Diagram of an absorption spectroscopy setup.

Ultraviolet and visible (UV - Vis) absorption occurs when light passes through a transparent sample. The electrons of the sample transit from their ground state to an excited state by absorbing photons. The atom within the sample can also rotate and vibrate in addition to the electronic excitation. These rotational and vibrational motions can broaden the energy levels. The resulting spectrum is presented as a graph of absorbance (A_λ). The following equation gives the quantity of the absorbance, where I_0 is the intensity of the incident before passing through the samples, and I_1 is the intensity of the light that has passed through the samples.

$$A_\lambda = \log_{10}\left(\frac{I_0}{I}\right) \tag{3.3}$$

The absorption measurement is carried out by using a Cary 50 UV-Vis spectrometer. Figure 3.12 is a simple sketch of the setup. A Xenon flash lamp with a long lifetime of up to 3×10^9 flashes is used as the source of UV - Vis radiation. The intense flashes of the lamp allow that the light can pass through a beam splitter to give simultaneous reference beam correction without producing excess photometric noise. Before the beam is focused on the sample, the beam passes through an excitation monochromator, that is used as a band pass filter. In our experiments, the surface plasmon of Au nanowires along the long axis can only be excited by P - polarized light. Therefore, a P - polarizer is added to the light path. The plasmon intensity of Au is also sensitive to the incident angle. We fixed the sample on a rotator, which can adjust the incident angle from 0° - 60°. The

whole wavelength range is 190 nm - 1100 nm, and the absorbance spectrum of the samples are recorded by the software Cary WinUV.

3.4 Preparation of nanostructured arrays in porous alumina

The preparation of regular nanostructures has attracted a considerable interest due to their wide applications in nano-devices [113, 114, 115]. Porous alumina with self-organized hexagonal ordered nanopores are used for the transfer of nanopore arrangements to other materials. Generally, the preparation of nanodevices may be carried out in two ways: electrochemical deposition and physical deposition. This follows the general scheme of top - down and bottom - up processes. In electrochemical deposition, the nanowires are directly grown in free standing AAO with open pores from bottom to top. The second approach is using AAO as a mask on some special substrate, and nanomaterials grow on the substrates through the open pores.

In this thesis, the preparation of nanomaterials with the assistance of AAO can be divided into nanostructures on Si substrates, magnetic nanowires, and Au nanowires.

3.4.1 Quantum dots and nanorods on Si substrates

Quantum dot arrays on Si substrates are prepared by the evaporation of metals onto the ultrathin AAO template. The advantages of the evaporation method are an easy control of the nanodot growth the and extraction of the template without chemical pollutants.

In section 3.2, we introduced the preparation of free standing ultra thin AAO on an Si substrate. The AAO templates attach directly onto a Si (100) substrate because of van der Waals forces. High purity Ag (99.99%) is degreased and cleaned in aceton and distilled water. The Si substrate (1×1 cm) with AAO on top is installed in the cell. When the pressure of the cell reaches 10^{-7} Pa, the evaporation starts and the deposition time depends on the desired nanodots height (growth rate 20 nm/min). After deposition, the AAO template is simply peeled off with the assistance of tape, leaving the Ag nanodots on the Si substrate. All deposition is done at room temperature.

SEM is performed to determine the size and long range order arrangement of the nanodot arrays. Figure 3.13 shows the Ag nanodots on the Si substrate after removing the AAO templates. The templates grow in oxalic acid and sulfuric acid with pore sizes of 60 nm (a) and 30 nm (b), respectively. A well-ordered, homogeneous Ag nanodot array is shown in Figure 3.13 a. The dot size and inter dot distance match with the templates. Some dots are missing in Figure 3.13 b (as shown in arrows), and the pore size is not homogeneous on a small length scale. We assume that the existence of parts of the barrier layer between the Si

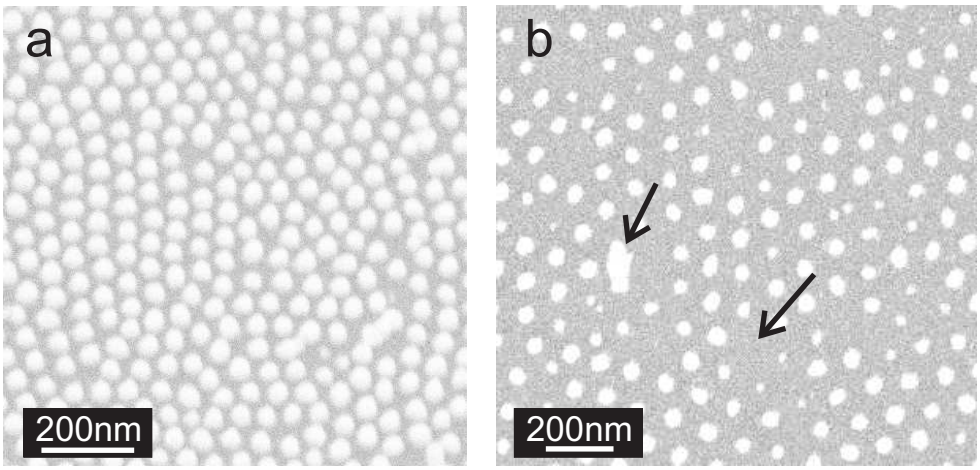

Figure 3.13: SEM image of Ag nanodots on Si substrate after peeling off the templates. The size and arrangement of the nanodots is in agreement with that of the pore arrays. a) nanodots grown in templates anodized in oxalic acid. b) nanodots grown in templates anodized in sulfuric acid.

and the pores results in the partial lack of dots. The quality might be improved by extending the etching time of the barrier layer in H_3PO_4.

Metallic nanorod/nanotube arrays are prepared by electrochemical deposition on directly anodized AAO templates on Si substrates. The advantage of this method over deposition is a stable connection between the nanostructures and Si.

The Si substrates combined with AAO templates are prepared as described in section 3.2. The deposition cell is self-made with a sample size of 1 cm (diameter). A Au plating solution (Au amount 25 g/L) from Sigma is used as the electrolyte, the reaction is controlled by a standard three electrode potentiostat (VersaSTAT 3 from Princeton Applied Research). The current between the reference electrode (Ag/AgCl) and the working electrode is constant at 300 mA. The growth rate is about 2 nm/s, which means that the nanorod length depends in a linear way on the deposition time.

Figure 3.14 shows SEM pictures of Au nanostructures on Si substrates. From the top view picture (Fig 3.14 a), the nanotubes grow from pores and the size and arrangement are fixed by the pores. When the deposition time is too long, Au can overgrow and form a layer on the top of pores, as shown in Fig 3.14 b. The length of the pores is about 200 nm. Au nanorods grow from the bottom of pores and cover the surface. Many techniques are employed to remove this layer, such as Ar etching and plasma etching. Au may form block structures on the top of pores, if the barrier layer is partly remaining on the bottom of pores. In this case, the Au nanorods can not fill all pores, as shown in Fig 3.14 c.

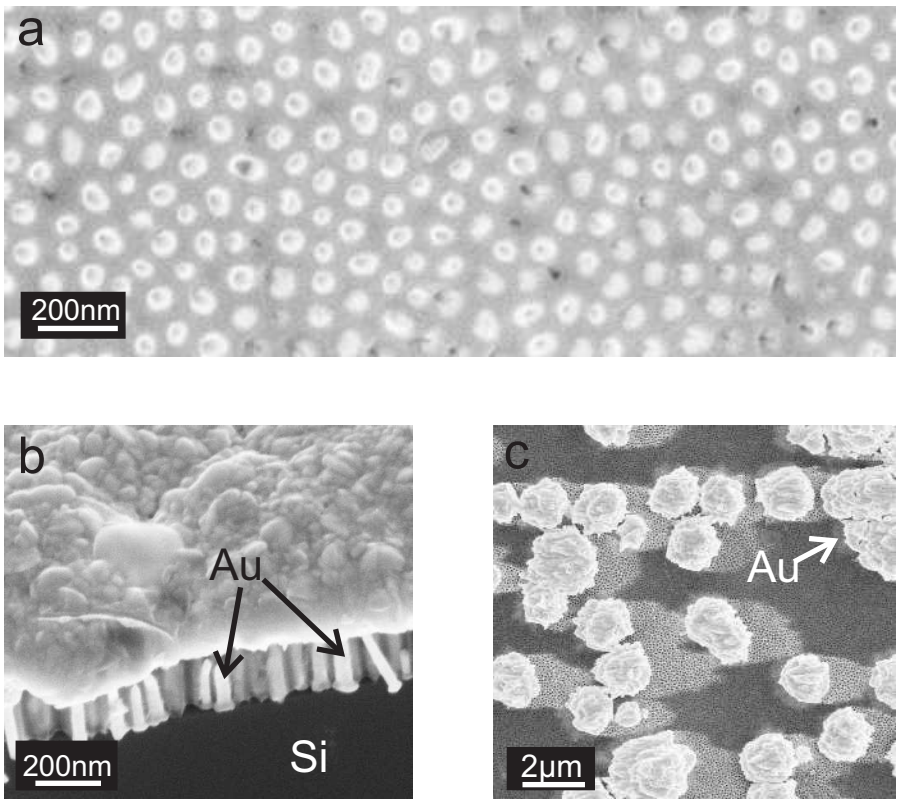

Figure 3.14: SEM image of Au nanorods/nanotubes on a Si substrate with AAO templates. The size and arrangement are controlled by the pores. a) Au nanotube formed in AAO templates on Si substrate. b) Cross view of overgrown Au layer and nanorods on Si substrates. c) Top view of partly overgrown Au blocks on the top of templates from Si substrates. The shadow-like effects are due to the argon etching used to remove the overgrown Au.

3.4.2 Magnetic nanowires

Magnetic nanostructures have stimulated a great deal of scientific, technological and application interest in the field of sensors and data storage [116, 117]. A much stronger magenetic effect has been developed from one dimensional magnetic composites structures, and they have been studied widely in recent decades [118, 119, 120]. In this section, we will introduce the preparation and characterization of magnetic nanowires in free standing AAO templates.

Two approaches are carried out to prepare magnetic nanowires: electrochemical deposition and sol-gel deposition. In both methods, free standing AAO templates with open pores are employed as a mask.

Electrochemical deposition is the better method for high aspect ratio nanowire growth because of the stable growth rate. In our experiment, a Ag film (around

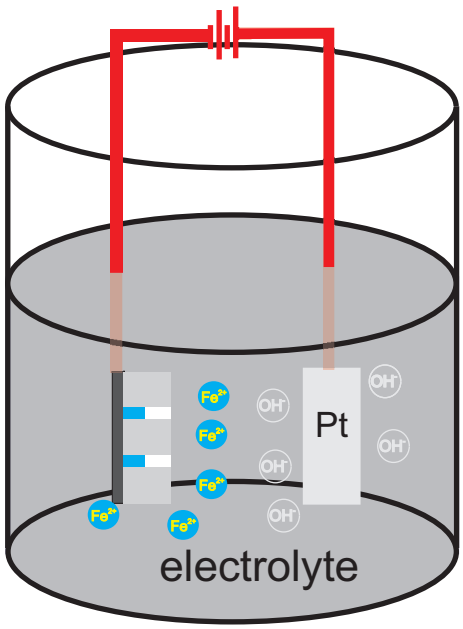

Figure 3.15: Sketch of the electrodeposition setup used to grow magnetic nanowires inside AAO templates.

300 nm thickness) is evaporated on one side of the pores as a contact cathode, then the edge of the samples and the Ag film are covered by nail polish which is insulating, so that only the contact at the bottom of the nanopores is exposed through the pores in the electrolyte, and wires grow from the bottom of the pores. A platinum foil is used as the anode. A sketch of the setup is given in Figure 3.15.

For Fe nanowires, the electrolyte contains 80 g/L $FeSO_4 \cdot 7H_2O$ and 30 g/L H_3BO_4. The deposition potential is 1.5 V, and the growth rate is about 5 nm/second. For the deposition of Ni nanowires, 26 g/L$NiSO_4 \cdot 6H_2O$ and 45 g/L H_3BO_4 is used as electrolyte. All experiments are done at room temperature.

Sol-gel has also been considered as a powerful approach for preparing ceramic materials based on an AAO template [121, 122, 123]. In our experiment, we prepared CoFeO nanowires with the intended spinel stoichiometry $CoFe_2O_4$ in AAO templates using a sol-gel precursor solution by three steps. First, stoichiometric amounts of $Fe(NO_3)_3 \cdot 9H_2O$ (0.032 mol/L), $Co(NO_3)_3 \cdot 6H_2O$ (0.016 mol/L) are dissolved in 10 ml ethylene glycol and stirred at 110°C until a gel is formed as the sol-gel precursor solution. The template is immersed in this solution for more than 30 hours with the assistance of an ultrasonic bath, then the template surface is cleaned with glycol. Next, the templates filled with sol-gel are annealed in air with the annealing temperature linearly increasing by 60°C/hour until 550°C for 12 hours. Finally, the templates are dissolved in a NaOH solution in order to investigate individual wires with electron microscopy.

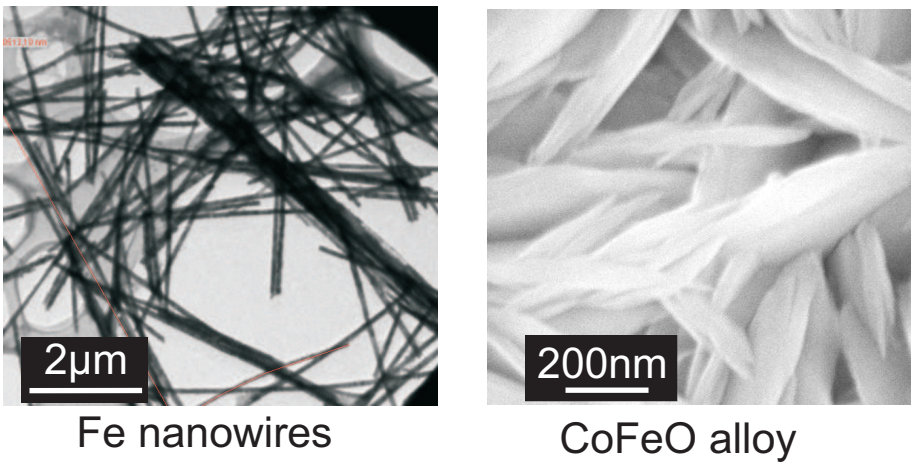

Figure 3.16: Electron microscopy pictures of magnetic and ceramic nanowires after dissolving the templates. Left: Electrochemically deposited Fe nanowires. Right: sol-gel deposited CoFeO nanowires.

Figure 3.16 shows Fe nanowires deposited by the electrochemical approach and CoFeO nanowires deposited by the sol-gel approach. The diameter of the Fe nanowires is essentially controlled by the pore size. The length is approximately 7 μm, leading to an aspect ratio of 1 : 90. The length of CoFeO nanowires is shorter than that of the Fe nanowires because the diffusion of ions is limited by the diameter of the pores. The sharp tip of the nanowires proves this point. We did not check the chemical composition of the wires as we were mainly interested in the relation of template and nanowire geometry and whether the length scales of these objects can be transferred [100].

3.4.3 Au nanowires

Au nanowires are used as a biosensor for targeted species detection because of their high capture efficiency and fast response time [124]. In our experiments, we prepared Au nanowire arrays in AAO templates and studied the coupling between molecular excitons and the specific surface plasmon from Au nanowire arrays. In the following we will introduce the preparation process of Au nanowire arrays.

Before electrodeposition, a 300 nm Ag layer is sputtered on one side of AAO as a conductive layer. Then the electrodeposition of the nanowires is carried out in a standard three electrode electrochemical cell. A platinum mesh is employed as a counter electrode, and a Ag/AgCl (saturated KCl solution) electrode is used as a reference electrode. The electrolyte is Auruna 5000 (gold content 7 g/L) with a pH value of 6. A constant current mode with 382 μA/cm^2 is used to deposit Au nanowires into the pores, and the growth rate is about 3 nm/second. To

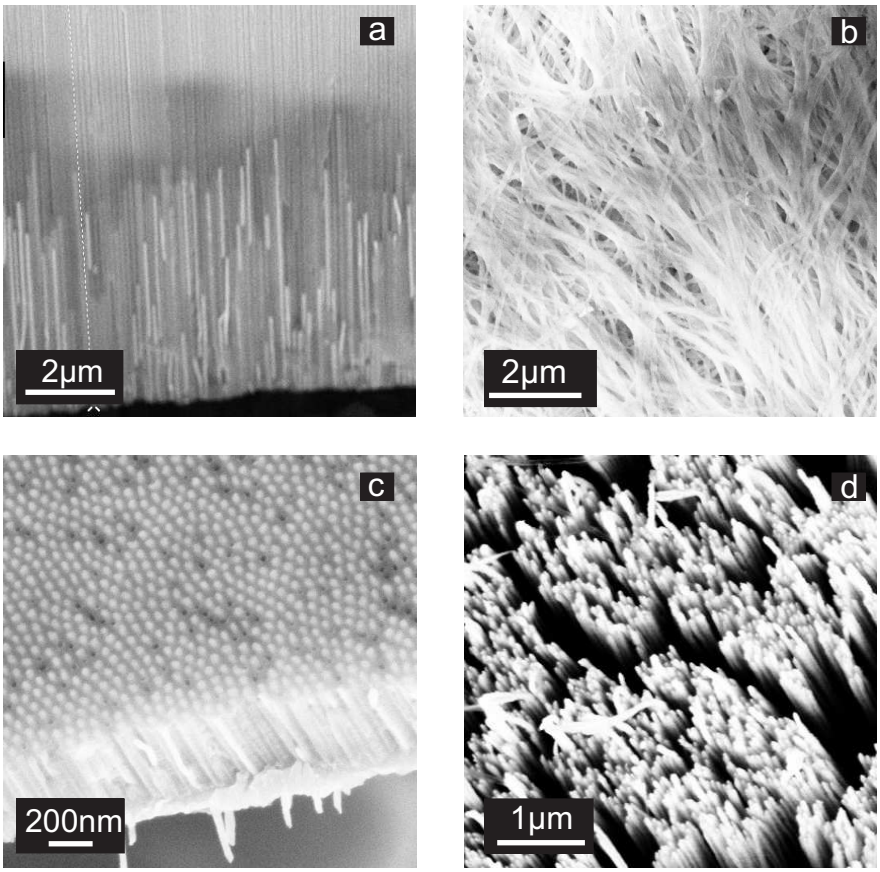

Figure 3.17: SEM images of Au nanowires with different morphology: a) Cross view of Au nanowires in AAO templates; b) Released nanowires from AAO templates; c) Au nanowires in AAO templates after Ar etching; d) Free standing Au nanowires with partly removed AAO. The wires agglomerate because of adhesive forces after removing the AAO template.

liberate the nanowires from the template, the template is immersed in 5% H_3PO_4 for several hours until all of it is dissolved. Then the nanowires are washed with a large amount of deionized water. For studying optical properties, the Ag layer on the template is dissolved by HNO_3, and the sample is thinned down from top to bottom by Ar ions.

The surface and cross views of different kinds of Au nanowires are shown in Figure 3.17. Au nanowires grown in a template prepared in oxalic acid are characterized in Figure 3.17 (a). The white lines are the Au nanowires growing along the pores. After dissolving AAO with H_3PO_4, the nanowires are released, as shown in Figure 3.17 (b). After etching the top empty part of the AAO template, the wires are partially freestanding as shown in Figure 3.17 (c).

It is reported that the wire diameter is significantly smaller after the removal of the Ag layer from the template, which leaves a gap between the nanowires and the pore walls of AAO templates [125]. In later experiments, we deposited molecules in this gap and characterized the coupling between surface plasmons of Au nanowires and excitons of the molecules. Auger electron spectroscopy (AES) was used to detect the element composition of the Au nanowires arrays. This experiment is done in Prof. W. Daum's group, TU Clausthal. Figure 3.18 gives the spectra, and C, Al, O, and Au were detected. The carbon is from the anodizing process, because oxalic acid is used as electrolyte, some oxalates are formed and remain in the alumina.

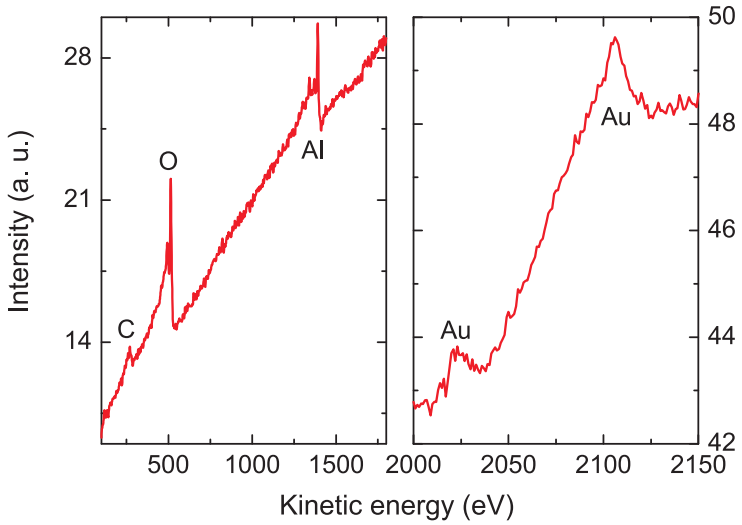

Figure 3.18: Auger spectrum of an Au nanowires array in AAO template, different peaks for C, O, Al and Au are observed.

3.5 Theoretical modeling

In this chapter, we will demonstrate the formation of an external plasmonic mode in Au nanowire arrays based on the finite element method (FEM). JCMwave software from the Zuse Institute Berlin (ZIB) for applied mathematics and computer science is used to simulate the propagation of electromagnetic (EM) waves with an exceptionally high accuracy. The main part of JCMwave is JCMsolve, which allows to handle the EM simulation with 1D, 2D and 3D geometries. JCMgeo is a flexible geometry tool, which automatically generates 1D, 2D and 3D finite element meshes. We define all details of sources, geometries and materials by embedding scripts with Matlab. All parameters can be conveniently changed in the scripts after building the simulation project.

As we have described in chapter 2, the geometry and shape of metallic nanoparticles dominates the surface plasmonic behaviors. In order to interpret the EM coupling between the dipolar longitudinal plasmon resonance we modeled single Au nanowire and Au nanowire arrays in an AAO matrix to simulate their optical properties. In addition, the anisotropic nature of the Au nanowires SPR is observed in the simulation.

In a single nanowire model, a hexagonally shaped 3D AAO cylinder is filled with Au in the center part, and the remaining top and bottom parts are filled with air pillars. There are two exterior infinite air layers located on the top and bottom of the whole model. The dielectric constant of AAO is defined as ε = 2.56, the length and diameter of nanowires are 200 nm and 25 nm, respectively. Through the infinite air layer, the incident light is p polarized with a varying incident angle between 0° and 50°, because the longitudinal mode of Au nanowires can only be excited by p polarized light. The dielectric constant of Au is obtained from Drude's law[134, 135].

$$\varepsilon_{\mathrm{Drude}}(\omega) = 1 - \frac{\omega_{\mathrm{p}}^2}{\omega^2 + \eta^2} + \mathrm{i}\frac{\eta\omega_{\mathrm{p}}^2}{\omega(\omega^2 + \eta^2)} \tag{3.4}$$

where ω_{p} is the plasma frequency, with $\omega_{\mathrm{p}} = 13.8{\cdot}10^{15}\mathrm{s}^{-1}$, and η is the damping constant, with $\eta = 1.075{\cdot}10^{14}\mathrm{s}^{-1}$.

In the Au nanowire arrays model, all nanowires are arranged with a periodic hexagonal arrangement in an AAO matrix with an infinite number of wires. Both inter wire distances and wire length are tunable. There are infinite air layers on the top and bottom of Au-AAO arrays. The periodic geometry greatly reduces the amount of memory required to perform the calculations. The incident source and the dielectric constant of AAO and Au are defined as being the same as for a single nanowire model. Figure 3.19 gives the model geometries. Different materials are marked in different colors, the triangle size defines the accuracy of the calculation. From the top view figures we can see that the Au nanowire is located at the center of the pores. Both models are compared to the samples prepared in our experiments.

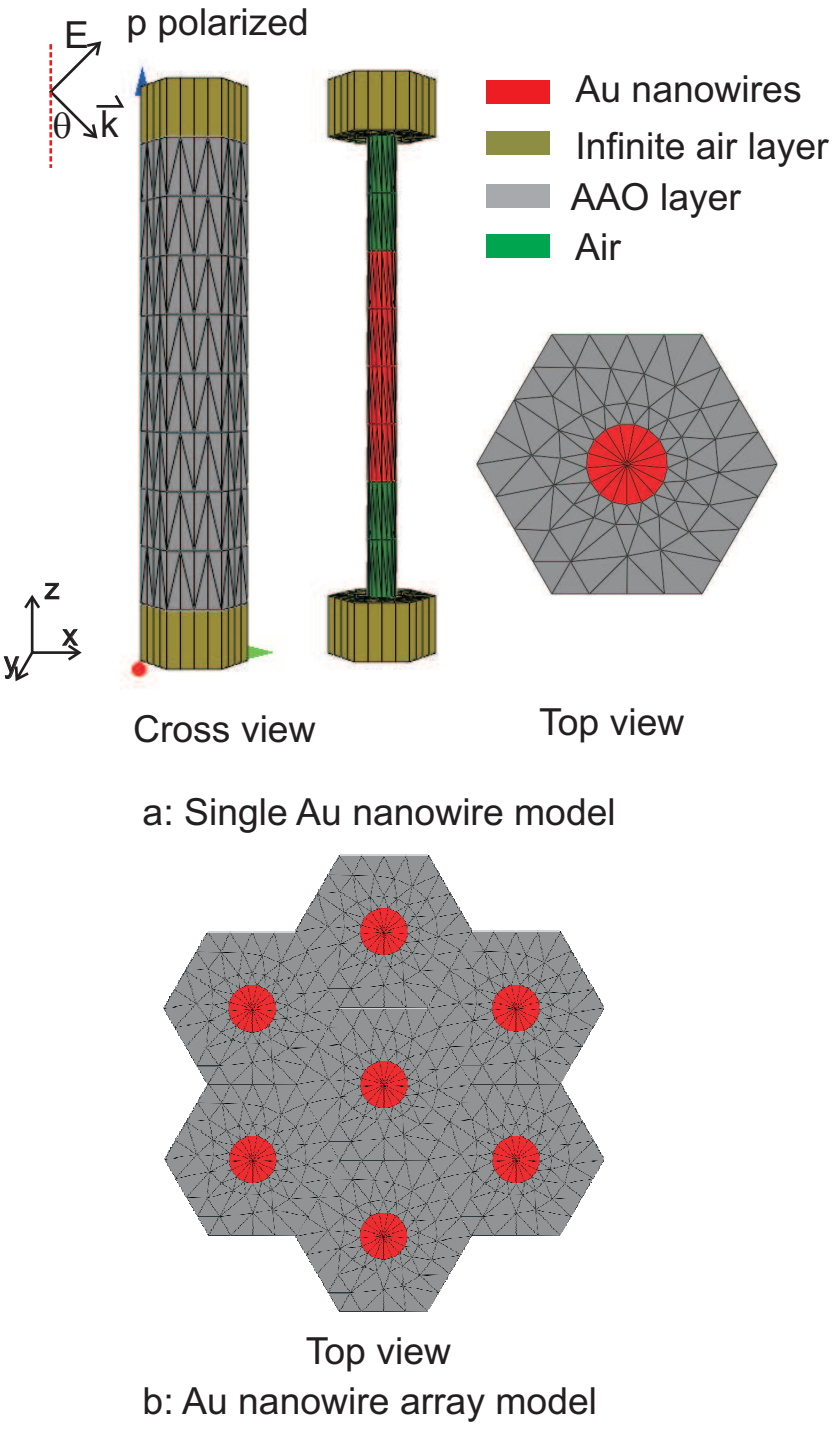

Figure 3.19: a) The single Au nanowire model, shown in side view and top view; b) The Au nanowire array. All nanowires are perpendicular to the infinite air layers with a hexagonal order from the top view.

Chapter 4

Investigations of porous alumina

AAO templates with insulating properties and chemical inertness allow the application of electrochemical and other techniques for preparation of a wide range of nanoscale periodic materials [126, 127]. It is evident that the physical and chemical properties of the AAO influence the characteristics of the nanocomposites. Therefore, they must be investigated and optimized according to preparation techniques and conditions. In this chapter, we will introduce the investigation of AAO templates, including optical properties, crystallization of AAO and Raman spectra. Results of our investigation of optical properties of AAO have been published [128] as well as the results on energy transfer between organic molecules and porous alumina [129].

4.1 Optical properties

4.1.1 Photoluminescence and absorption spectra

Up to now, research focuses mainly on photoluminescence (PL) spectra as the basic information on the optical properties of AAO [130, 131, 132, 133]. These investigations show a blue PL band in the wavelength range of 300 - 600 nm. The origin of this band has been discussed, and it has been found to depend on the preparation conditions of the templates. In the application of plasmonic arrays as sensing devices a possible readout scheme may be based on a fluorescence signal modified by energy resonance transfer involving, e.g., quantum dots or dye molecules which can be further sensitized by plasmonic nanoparticles and wires. In this section, we combine the PL spectra and absorption spectra to investigate the optical properties of AAO.

In our experiments, all PL and absorption data are from AAO templates prepared by a typical two-step anodizing electrochemical procedure, and all annealing processes are carried out in the air. Figure 4.1a presents the PL spectra of as-prepared and annealed AAO templates prepared in oxalic acid, measured with an excitation energy of 405 nm. It can be seen that an intensive and broad PL

emission band appears at about 500 nm. The intensity of this band increases with increasing annealing temperature and reaches a maximum for the sample annealed at 600°C. However, the intensity drops with further increasing of annealing temperatures to 700°C, and the signal even vanishes at 800°C. These optical properties of PL are associated with the density of oxygen vacancies in AAO and the recrystallization processes of AAO annealed at different temperatures. The X-ray diffraction shown below reveals that the AAO transforms into a crystalline phase from the amorphous state after annealing at 800°C.

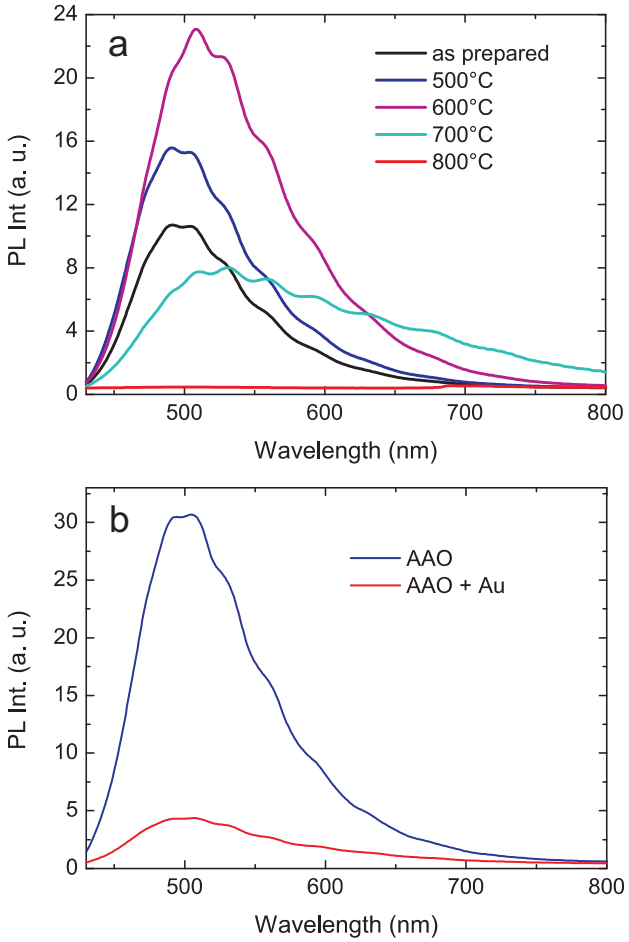

Figure 4.1: a) PL spectra of AAO templates with open pores. The samples are as prepared and annealed at 500°C, 700°C, 800°C, respectively; b) PL spectra of as prepared AAO and Au-AAO templates using 405 nm excitation.

The PL intensity is quenched or suppressed, comparing the as-prepared AAO template with the template that incorporates Au wires of approximately 50 nm length, as shown in Figure 4.1b. This quenching is due to an efficient fluorescent resonance energy transfer [136, 137] between the plasmonic absorption of the Au

wire lattice and the PL band of AAO. Such an energy transfer depends critically on the donator-acceptor separation, which is small due to the spatial proximity of the wires and the AAO. Therefore, within the sensitivity of our setup, we are not able to detect any PL in AAO templates with deposited Au wires with high aspect ratio.

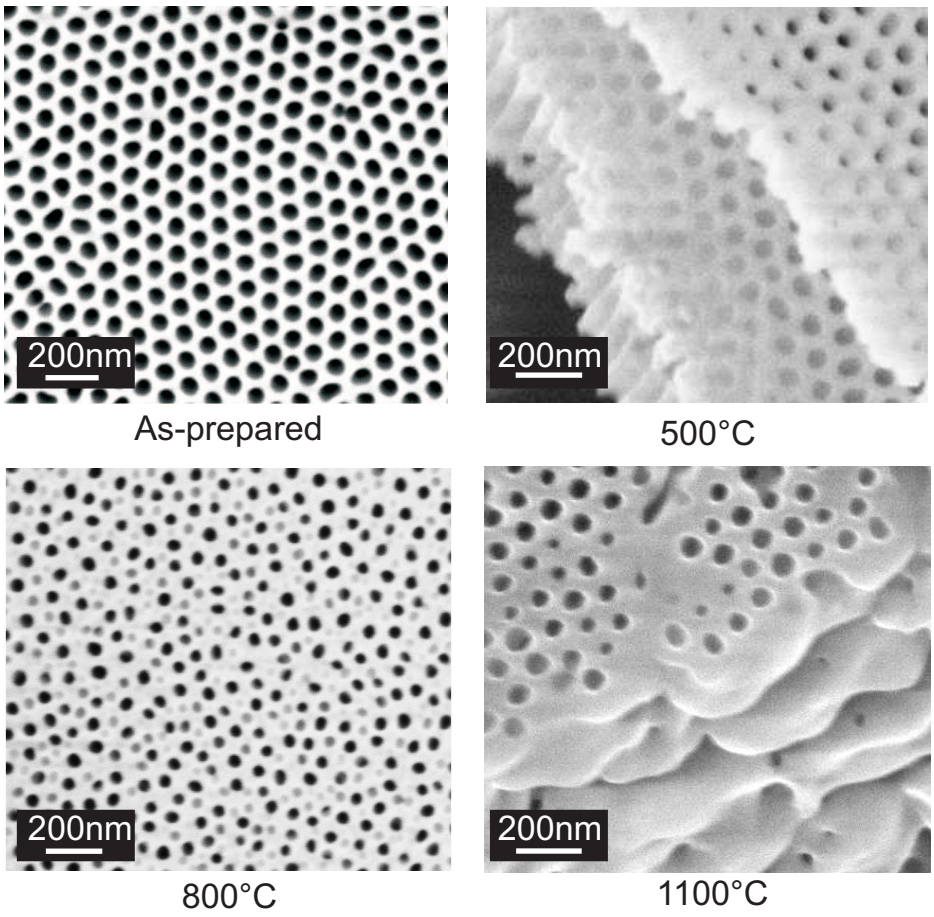

Figure 4.2: SEM pictures of the as-prepared AAO and the templates annealed at 500°C, 800°C and 1100°C, respectively.

The morphology and absorption spectra of as-prepared and annealed AAO are investigated in our experiments to confirm origins of the intensive PL signals. Figure 4.2 gives the SEM pictures of as-prepared AAO and the templates annealed at different temperatures. The as-prepared sample is prepared in oxalic acid with a pore diameter of 60 nm and inter pore distances of 40 nm. After annealing at 500°C, the pores are still ordered, but the template becomes layered. We assume that this is caused by the decomposition of oxalic impurities in AAO. After annealing at 800°C, the pore orientation and distance are less ordered and

fluctuate to a large extent. We attribute this change of appearance to an inhomogeneous volume expansion of Al_2O_3 during the annealing processes in which the remaining aluminum particles are oxidized. After annealing at 1100°C, the pores are not open because of the recrystallization of Al_2O_3. With respect to the macroscopic properties, the templates change from as-prepared transparent film to ceramic-like opacity.

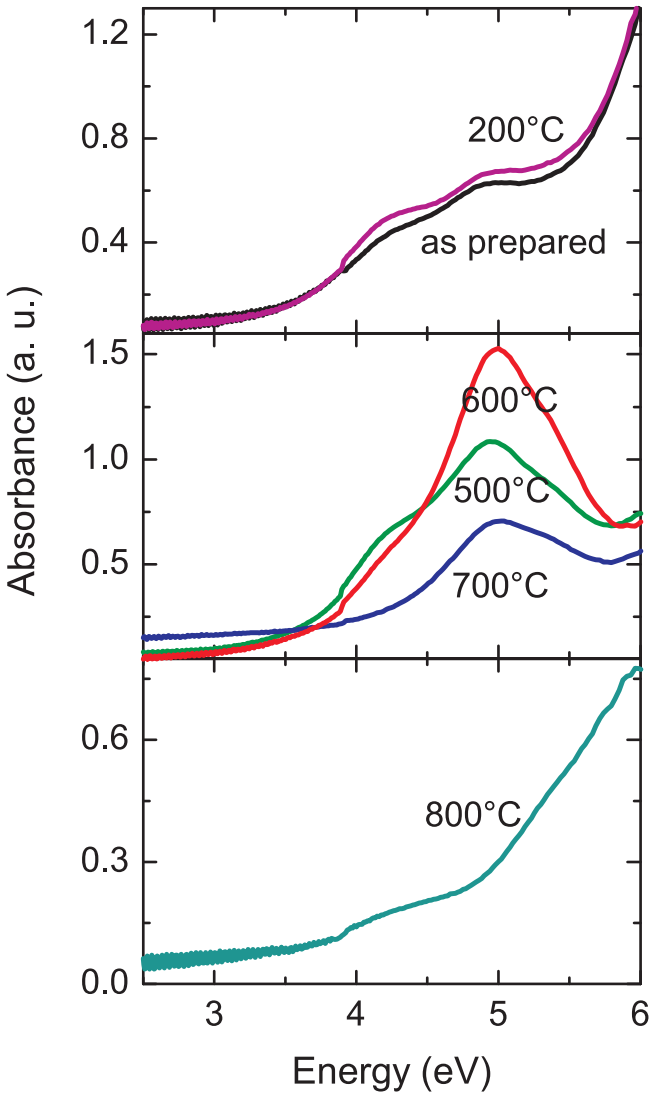

Figure 4.3: Absorption spectra of AAO as prepared and annealed at 200°C, 500°C, 600°C, 700°C, 800°C.

The optical absorption spectra of AAO templates prepared in 0.3M oxalic acid and annealed at different temperatures are shown in Figure 4.3. Due to the treat-

ment, an increase in absorbance is observed, leading to a structured maximum in the spectral range of 4 - 6 eV. With increasing annealing temperatures, it reaches its maximum for an annealing temperature of 600°C and then decreases for annealing at higher temperatures. For annealing temperatures of 800°C and 900°C, the absorption bands decrease. This behavior is similar to the PL spectra of the annealed AAO templates. Higher energy absorption data of as-prepared AAO with one absorption peak at approximately 6 eV is available in Ref [138]. The analysis of this peak has been omitted here as it is close to the high energy limit of our setup.

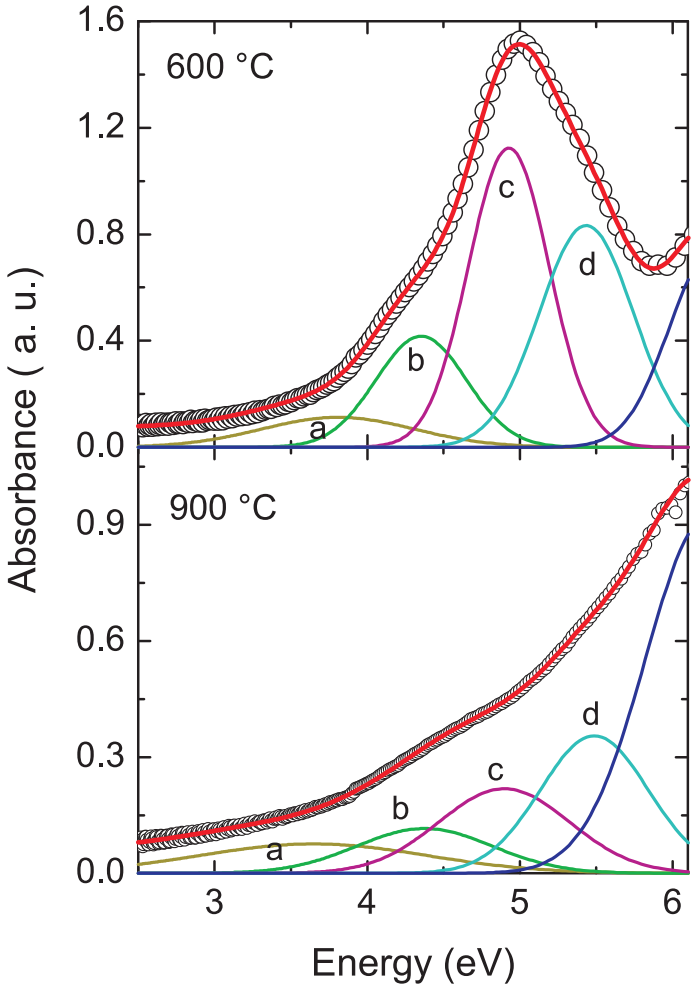

Figure 4.4: Absorption spectra of AAO annealed at 600°C and 900°C, respectively, together with a deconvolution into four processes denoted by a, b, c, d.

Figure 4.4 shows spectra for samples annealed at 600°C and 900°C together with a spectrum deconvolution using four absorption sub-bands at 3.8, 4.3, 4.9,

5.4 and 6.1 eV. These peaks are attributed to various oxygen vacancies in AAO templates. As the intensity of oxygen vacancies changes at different temperatures, they dominate the intensity of PL and absorption spectra. For higher annealing temperatures, a significant change of the absorption and PL is observed as a function of time, as shown in Figure 4.5. This shows some processes based on a chemical reaction taking place in AAO with a temperature close to 700°C.

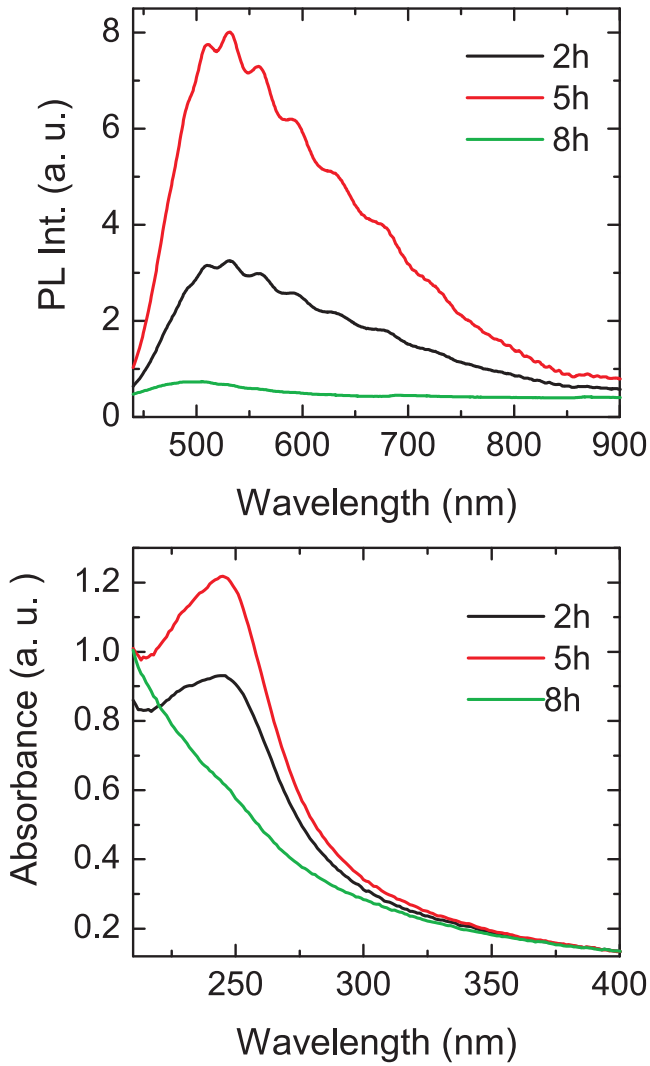

Figure 4.5: Absorption spectra from AAO templates annealed at 600°C and 700°C for 2, 5, and 8 hours, respectively.

The doping of transition metal or rare earth ions into solid state matrices is often used to realize optically active materials, that can be used, e.g. in LASER applications. Examples are Ti:sapphire lasers (Ti:Al_2O_3) and ruby lasers (Cr:Al_2O_3).

As the AAO template allows easily a doping during or after the pore formation, we have investigated briefly the optical properties of the respective materials. We have also noticed that metallic aluminium of inferior purity used to prepare AAO template is often polluted by transition metal ions. In the following we will show that optical absorption of AAO templates can be used to detect such intentional or unintentional dopings.

The chromium doped samples allow us to study the crystallization process during annealing using Cr as an internal sensor. This can be achieved by (S)EXAFS, EXAFS and XANES spectroscopy. These tools reveal the structural environment of the nearest and next-nearest neighbouring crystallographic shells of the tracer atom in a similar way as described by Kizler et al. [139]. In our experiments, templates with open pores are doped with Cr^{3+} by immersing the templates in a $Cr(NO_3)_3$ solution for 8 hours, and then crystallize to the α-Al_2O_3 phase. With excitation at 532 nm, a strong PL signal is observed at about 693 nm and 694 nm, as shown in Figure 4.6. The as-prepared AAO templates give a broad PL spectra, which quenches when the sample is annealed at 900°C. We suppose this behavior is associated with the crystallization process of AAO templates at high temperatures. When the annealing temperature reaches 1100°C, the AAO with doped Cr^{3+} gives a strong sharp peak at around 694 nm. This is obviously related to the R-line of ruby. The inset in Figure 4.6 shows an enlargement near 694 nm. The PL spectrum indicates the successful doping of Cr^{3+} is into the crystallized α-Al_2O_3 phase, and the PL spectra of the samples heavily depend on the structural properties of the host. The phases of AAO are not pure after annealing at 900°C, however, a pure α-Al_2O_3 phase is formed at 1100°C. This crystallization process is confirmed by X-ray diffraction of AAO described in a later section.

4.1.2 Oxygen defects

The PL and absorption properties of undoped AAO are related to the oxygen defects in AAO as the optical gap is very large [140, 141]. Studying the defects, their formation, mechanisms and emission characteristics can help to understand the origin of PL and absorption signals. In this section, we investigate different types oxygen defects in AAO templates. Additionally, we control and vary the defect density by annealing at different temperatures. This allows the clarification and optimization of optical properties of the AAO. As the templates are free-standing and the pores are permeable, no side effects due to supporting agents or substrates exist.

For single crystalline Al_2O_3, extensive studies exist on defect-induced absorption which is naturally present or induced by radiation damage [142, 143, 144]. Such studies were mostly motivated by the high stability and application of Al_2O_3 as a catalyst support. In AAO templates, one might expect analogous defect centers, complex composition and amorphous structures. It is understood that oxygen ions migrate through the barrier layer along a high electric field (10^6 V/cm) by means of a vacancy mechanism [145, 146, 147]. The inhomogeneous electric

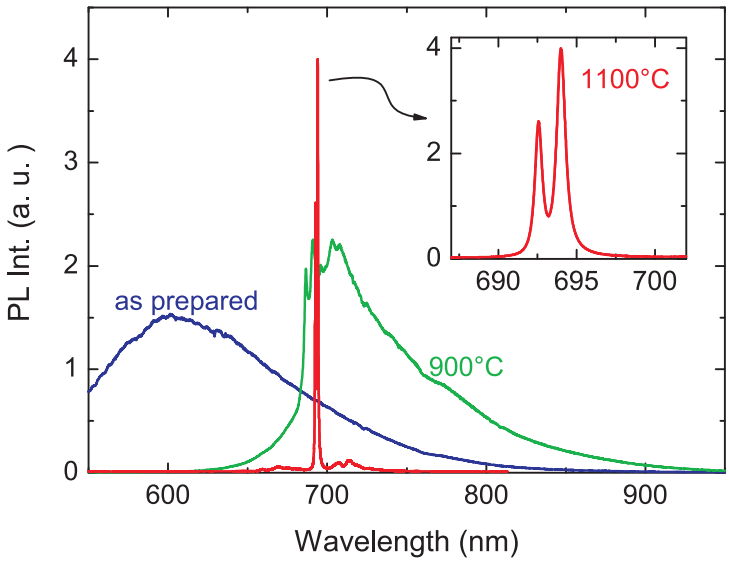

Figure 4.6: The PL spectrum of the as-prepared AAO and annealed AAO obtained with an excitation wavelength of λ = 532 nm. The inset zooms into the PL spectrum from AAO annealed at 1100°C.

potential at the pore centers and towards the pore walls leads to the formation of oxygen vacancies during the self-organized growth of the AAO membranes [148].

We assume that the experimentally observed sub bands (Figure 4.4) in the absorption at 3.8, 4.3, 4.9, 5.4 and 6.1 eV originate from optical transitions between various energy levels of the color centers. To allow an assignment, we compare our data with earlier experimental and theoretical studies on defects in crystalline Al_2O_3. In irradiated Al_2O_3, optical transitions observed at 3.8 eV (a), 4.8 eV (b), and 5.4 eV (c) were attributed to F^+ centers and optical transitions at 6.1 eV were attributed to F centers [149, 150]. The optical transitions in amorphous Al_2O_3 films were also observed in a similar energy range [151, 152, 153]. While single crystalline Al_2O_3 films have a gap of $\Delta \approx 9$ eV [154], the luminescence excitation spectra of amorphous Al_2O_3 shows a broad band gap. The gaps of amorphous Al_2O_3 and alumina vary in the literature from 3 - 7.9 eV [152, 153, 155]. These values depend on the Al coordination number and atomic bond lengths [152, 154] and therefore on the structural relaxation of ions surrounding an oxygen vacancy. The amorphous and relaxed structure of AAO also promotes an enhanced electron-phonon interaction [151, 152, 153, 154]. Figure 4.7 gives the relative energy positions of oxygen vacancies in neutron-irradiated crystalline sapphire.

In addition, the formation energy of defects in AAO is smaller than in single crystalline materials [156, 157]. For annealed Al_2O_3, it has been shown that the concentration of F centers is much larger than that of F^+ centers [158, 159]. The same effect can be expected in AAO, where F centers with high mobility may

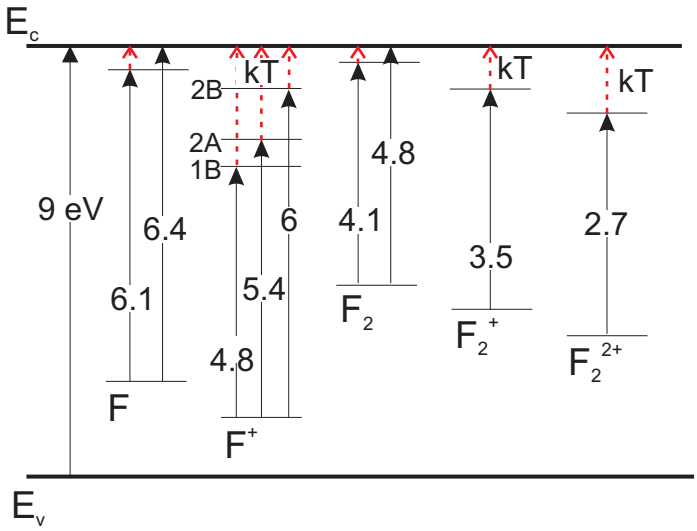

Figure 4.7: The relative energy positions of different oxygen vacancies in sapphire of several charge states [150].

combine and form F_2 centers by annealing, or the electrons in F centers may be excited in the annealing process to form F^+. The aggregation process of F centers is supposed to lead to the band at 4.3 eV based on F_2 centers. The latter have an energy of 4.1 eV in crystalline Al_2O_3. In contrast, the mobility of F^+ centers is too low to allow for a notable aggregation.

Within this scenario we expect a general reduction of the optical absorption with annealing that goes hand in hand with a broadening and shift to lower energies. In contrast we observe a non-monotonous dependence of the absorption area (Figure 4.8). We have integrated the area of the color center F^+ and plotted it together with the area of the peak at 4.3 eV, attributed to F_2. As seen in Figure 4.8, there is a pronounced maximum of F^+ absorption as a function of annealing temperature with a peak at 600°C. The integrated absorption drops for higher annealing temperatures. In contrast, the intensity of F_2 defects is temperature independent in the lower annealing temperature (< 600°C) range. We do not expect that the oscillator strength of the color centers changes with annealing. Therefore the integrated area is a measure of the defect density. To describe the initial increase of integrated absorption and related defect density, we consider that residual metallic Al is left from the electrochemical anodization process [160] during preparation and oxidizes in a subsequent annealing. This leads to spatially inhomogeneous reducing conditions. Al_2O_3 single crystals grown under reducing conditions show a form of $AlAl_2O_4$ spinels as a microcrystalline second phase [161]. The oxidation of nanoscale metallic Al is also consistent with the generation of oxygen vacancies in the surrounding AAO matrix until at higher temperatures also oxygen with longer diffusion paths can be utilized for the oxi-

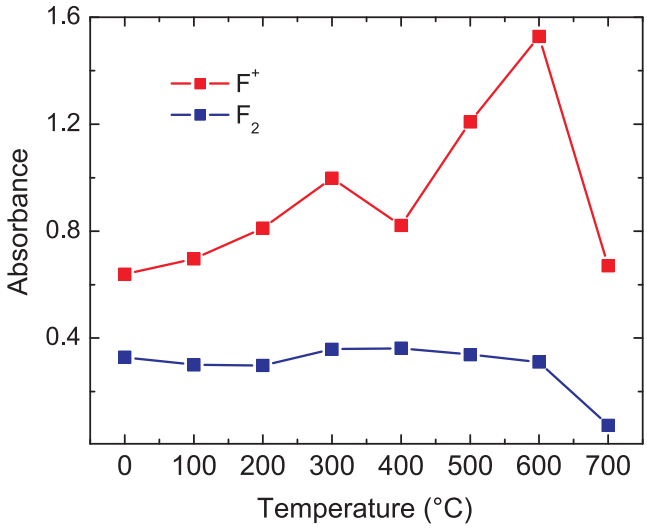

Figure 4.8: Dependence of the summed absorption area from peaks located at (3.8 eV, 4.9 eV and 5.4 eV): F^+ and 4.3 eV: F_2 color centers as function of annealing temperature. The concentration of defects in AAO is proportional to this integrated area.

dation.

The newly formed oxygen defects lead to a maximum as a function of annealing temperature in the integrated optical spectra of absorption and PL, and a broadening of the underlying absorption bands. For higher temperatures, the defect mobility is also the reason for the large change of morphology demonstrated in Figure 4.2. This interplay of both temperature dependent reactivity and diffusivity within a nanoscale inhomogeneous matter leads to interesting dynamics with temperature and time. The similarity of the optical absorption and PL intensity with respect to their dependence on annealing temperature, shown in Figure 4.1 a and Figure 4.3, indicates a relation of the two processes. Above, we have established oxygen vacancies as a primary origin of absorption in the spectral range 3 - 6 eV. It is, however, not clear why the PL band is only at approximately 500 nm $\approx$ 2 eV. The Stokes shift between related absorption and emission processes is due to vibrational coupling and relaxation and is much smaller in molecular systems. We attribute the big Stokes shift ($\Delta\lambda \approx 250$ nm) to a very high number of emitted phonons during non radiative processes and the amorphous structure of AAO [162]. An amorphous solid has a dense spectrum of vibrational and electronic levels, momentum conservation is canceled and randomness leads to back-scattering and localization of light [163, 164]. This combined effect is proposed to increase the electron-phonon coupling and thereby the phonon emission and the Stokes shift.

4.2 Energy transfer between organic molecules and porous alumina

AAO is used as a template for a variety of nanotechnological applications, for example, for growing rare earth wires (Tb, Eu) [165, 166], polymers [167, 168] nanostructures, sensor materials [169], photonic crystals [170], and solar cells [171], magnetic storage [172], cell culturing [173], as well as for drug delivery [174]. We discussed the oxygen vacancies and the photoluminescence properties in earlier sections, which enable us to study the properties of the nanocomposites related to AAO templates. For the last decades, the mechanic properties and the preparation mechanisms [175] of AAO have attracted a vast research attention. The luminescence mechanisms of morin and morin protein embedded into AAO films have been discussed by Jia [177]. The results show that the PL appearance and enhancement are induced by the interaction of morin and the remaining aluminum in AAO as well as by the coexistence of the embedded dye and protein.

Therefore, in this section, photo-induced charge transfer from AAO to different molecules is studied. All AAO templates are anodized in oxalic acid solutions and then annealed at 500°C. This allows a maximum number of color centers and hence strong optical activity. Benzoquinone (BQ, Alfa Aesar) is a well-known electron acceptor [178]. The charge transfer dynamics of AAO templates and BQ as a complexation is investigated using femtosecond-resolved fluorescence upconversion techniques. The Förster resonance energy transfer (FRET) dynamics from AAO templates to nanopore embedded CdSe (Map Red) (EVIDOTS, USA) quantum dots (QDs) and Au nanowires will also be demonstrated in the following experiments. The ion transport channel of the exciton generated in the QD is enhanced by using FRET in inorganic QD based solar cells, as the traditional limitations of charge separation and transport are bypassed by an additional path way [179, 180, 181]. Picosecond-resolved fluorescence spectroscopy and steady state spectroscopy are used to demonstrate that QDs/Au nanowires embedded in AAO can be excited by the color center-induced PL from AAO templates. This is due to the enhancement of light absorption. In this context, another pathway of nonradiative quenching, nano-surface energy transfer (NSET) [182], was found to prevail in AAO-Au composites. We will present a detailed demonstration of the ultrafast excited state deactivation of porous alumina with various fluorescence quenchers in this context. The experiments were performed in the laboratory of S. Pal, SNBC, Kolkata, India.

According to the following equations [183], the Förster distance (R_0) is given to estimate the FRET efficiency of the donor (AAO) and hence to determine distances of donor-acceptor pairs:

$$\mathrm{R}_0 = 0.211 \times \left[\kappa^2 \mathrm{n}^{-4} \mathrm{Q}_\mathrm{D} \mathrm{J}\right]^{\frac{1}{6}} \quad , \tag{4.1}$$

where κ^2 is defined by the relative spatial orientation of the transition dipoles of the donor and acceptor. κ^2 is assumed to be $2/3$ when the donors and acceptors

are randomized by rotational diffusion prior to energy transfer. n is the refractive index of the medium, which is assumed to be 1.4 [129]. The integrated quantum yield of the donor (QD) in the absence of an acceptor is measured to be 5.0×10^{-3}, with respect to a reference dye Proflavine (QD = 0.34). J is a factor describing the degree of spectral overlap between the donor emission intensity (normalized to unit area) [184] and the acceptor absorption, which is given by the following equation:

$$\mathrm{J} = \frac{\int_0^\infty \mathrm{F_D}\left(\lambda\right) \varepsilon_\mathrm{A}\left(\lambda\right) \lambda^4 \mathrm{d}\lambda}{\int_0^\infty \mathrm{F_D}\left(\lambda\right) \mathrm{d}\lambda} \quad , \tag{4.2}$$

where $\mathrm{F_D}(\lambda)$ is the dimensionless fluorescence intensity of the donor in the wavelength range of λ to λ+dλ. $\varepsilon_\mathrm{A}(\lambda)$ is the molar extinction coefficient (in $\mathrm{M^{-1}cm^{-1}}$) of the acceptor at the wavelength λ. In our experiments, Map Red QDs and Au nanowires with extinction coefficients $7{\times}10^{-5}\mathrm{M^{-1}cm^{-1}}$ (λ = 591 nm) [185] and $7.66{\times}10^{-9}$ $\mathrm{M^{-1}cm^{-1}}$ (λ = 528 nm) [186] have been studied as two energy-acceptor molecules. J is in units of $\mathrm{M^{-1}cm^{-1}nm^4}$ for a given wavelength in nm. The donor-acceptor (D-A) distance (r) can be easily calculated using the following equation, if the value of $\mathrm{R_0}$ is known:

$$\mathrm{r}^6 = \frac{\left[\mathrm{R}_0^6\left(1-\mathrm{E}\right)\right]}{\mathrm{E}} \quad , \tag{4.3}$$

here E is the efficiency of the energy transfer that was measured using the relative fluorescence lifetime of the donor, in absence (τ_D) and in presence (τ_DA) of an acceptor.

$$\mathrm{E} = 1 - \frac{\tau_\mathrm{DA}}{\tau_\mathrm{D}} \quad , \tag{4.4}$$

From the average lifetime for the AAO-Map Red or AAO-Au system, we obtain the effective distances between the donor and the acceptor (τ_DA), using equation 4.3 and 4.4.

In order to get a pure AAO template as a molecular host, a thermogravimetric analysis (TGA) is used to study the decomposition processes of oxalic impurities in AAO and the recrystallization processes of AAO. There are three weight loss regimes in the TGA results of the as prepared AAO, shown in Figure 4.9. Similar results were reported by Sun [187]. The first weight loss section extends from room temperature to 335°C, which is mainly attributed to desorption of weakly bound water molecules from the surface and inner walls of nanopores. As the temperature increases to the temperature range of 335 - 615°C, the oxalate impurities are decomposed, which prompts the second weight loss in the figure. The third section results from a phase transition taking place at 855 - 990°C. In later experiments, we observe a phase transition in XRD at T = 900°C. The templates used in this section are annealed at 500°C because all organic oxalate impurities are decomposed and they give the maximum PL intensity.

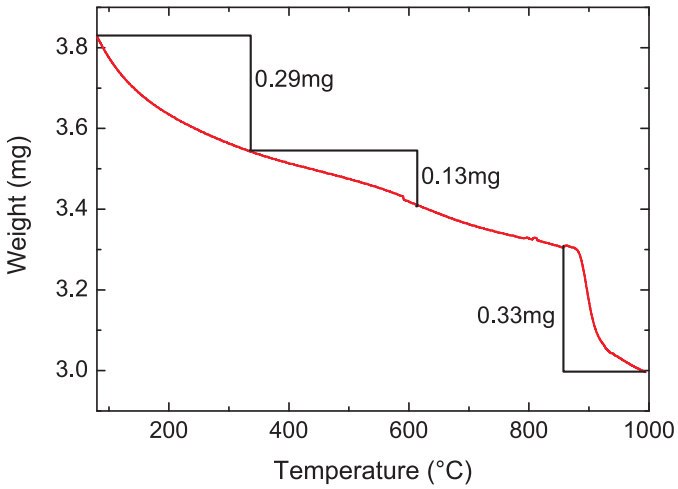

Figure 4.9: Thermogravimetric analysis for the as-prepared AAO template.

In Figure 4.10a, the PL spectra of pure AAO in the absence and the presence of BQ in the nanopores are depicted. The purple line is the excitation spectrum. All experiments are carried out at room temperatures. The frequency of the BQ carbonyl stretch vibration shows a red shift when the BQ is absorbed on a semiconductor surface in the infra spectra as reported by Burda [178]. The absorbed BQ molecules remove the photoexcited electron from the conduction band of the semiconductor faster than the laser pulse duration (< 120 fs) [188, 189, 190]. The electron transfer dynamics from the AAO templates upon excitation is studied by using the BQ as a complexation of the templates in our experiments. Figure 4.10b and c show the picosecond and femtosecond resolved PL quenching of AAO upon complexation with BQ at 450 nm. The picosecond resolved PL spectra of AAO-BQ and pure AAO templates are quite similar. Thus the excited state electron transfer process is too fast to be measured in the picoseconds resolved PL study. Therefore, we performed femtosecond PL spectroscopy to improve the understanding of the excited electron transfer process from the conduction band of AAO to the LUMO of BQ molecules. At the excitation of 375 nm, the fluorescence spectrum of AAO embedded in BQ shows a sharp decay of about 400 fs (59%). Previous studies demonstrated that electron transfer from CdSe quantum dots to surface-attached BQ induces an additional decay channel [190]. This results in a short decay component with a characteristic time constant comparable to the combination CdSe-BQ ($\approx$ 600 fs). The analogous dynamics of the electron transfer of the AAO-embedded BQ system with those of the CdSe-BQ system clearly signify the existence of an ultrafast photo-induced electron transfer dynamics from host AAO to the organic guest molecule BQ.

PL spectra of pure AAO and AAO impregnated with Map Red QDs and Au nanowires are shown in Figure 4.11a. We notice an apparent quenching of the

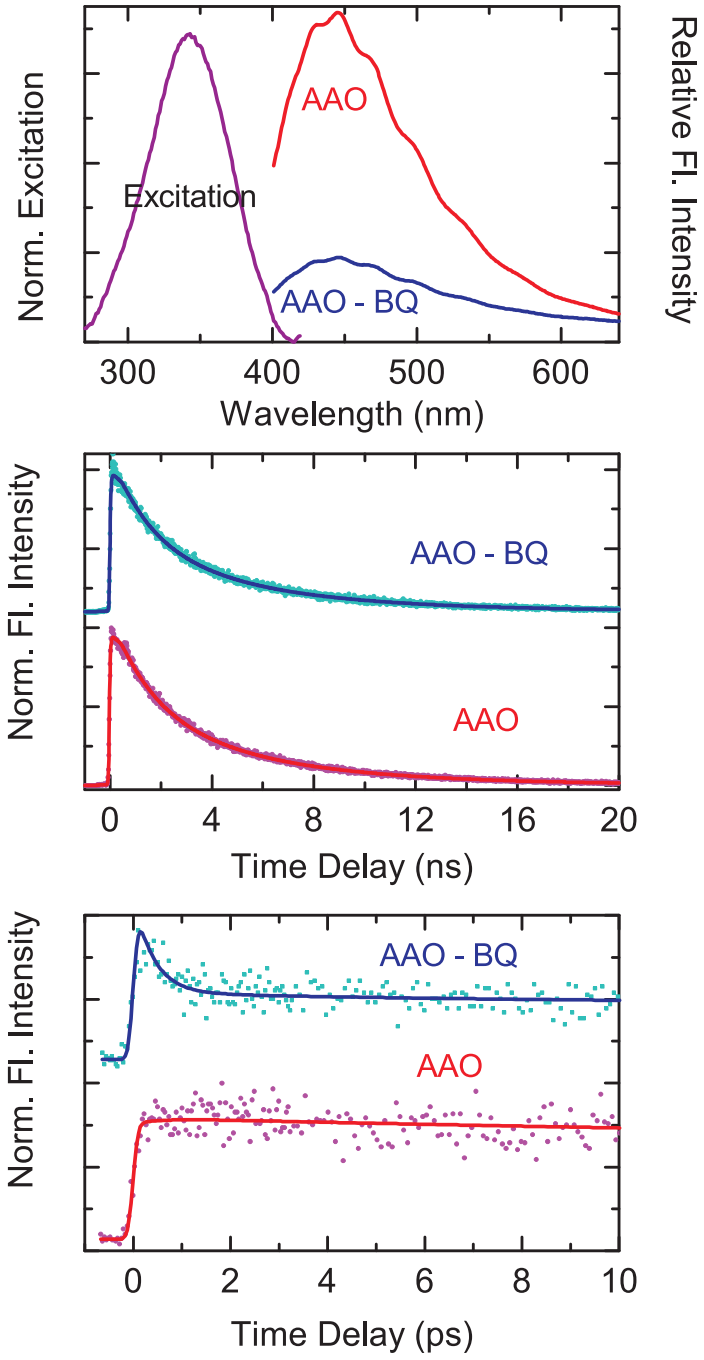

Figure 4.10: (a) Normalized excitation and emission spectra of AAO in the absence and the presence of BQ. (b) Picosecond-resolved fluorescence transients of AAO membranes in the absence (pink) and the presence of BQ (blue) measured at 450 nm (excitation = 375 nm). (c) Femtosecond-resolved fluorescence transients of bare AAO (pink) and BQ impregnated AAO (blue) collected at 450 nm showing a faster decay (excitation at 375 nm).

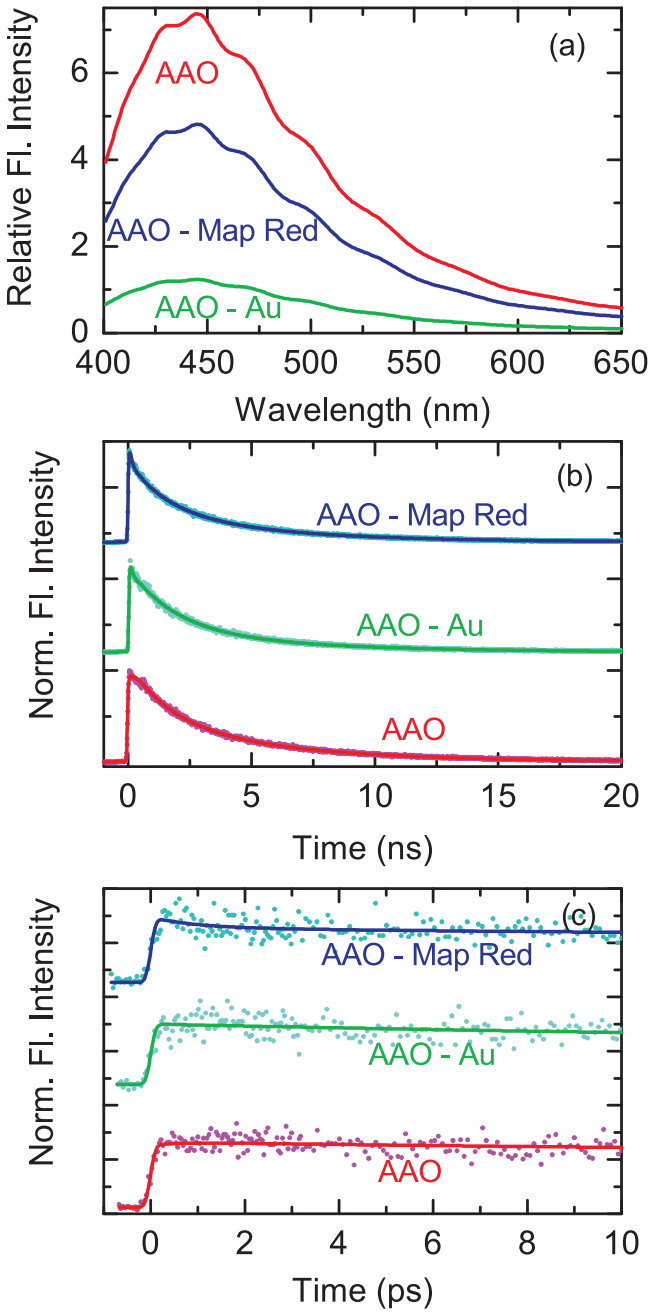

Figure 4.11: (a) Steady state emission spectra of AAO membranes, in the absence and the presence of gold nanowires and Map Red, (b) picosecond-resolved fluorescence transients (excitation at 375 nm, monitored at 450 nm), and (c) femtosecond-resolved fluorescence transients of bare AAO (red), Au nanowires (green), and Map Red (blue) impregnated AAO (excitation at 375 nm) collected at 450 nm.

PL spectra at around 450 nm after the QDs and nanowires are embedded. In the picosecond resolved PL spectra of Figure 4.11b, the lifetime of the AAO-Map red and AAO-gold is shorter than the bare AAO. Here, we suppose FRET takes place from a donor AAO to Map Red or gold acceptors, and it is responsible for the observed inhibition of the emission bands. To study the assessment of distances in numerous biomolecular assemblies, FRET in combination with Förster theory is considered an invaluable tool [183, 191, 192]. The FRET process is based on the concept of treating an excited donor as an oscillating dipole that can undergo energy exchange with a second dipole of a similar resonance frequency [183]. The excitation energy of the donor can directly transfer to the acceptor via the exchange of a virtual photon, if the fluorescence emission spectrum of the donor molecule overlaps the absorption spectrum of the acceptor molecule and the distance between donor and acceptor is small enough (1 - 10 nm). Figure 4.12 show the spectral overlap of the AAO emission spectrum with that of the Map Red and Au absorption spectrum.

Tables 4.1 and 4.2 give details of fitting parameters of the luminescence transients. The effective distance between the donor and the acceptor pairs of AAO - Map Red and AAO - Au complexes are obtained from the average lifetime following equations 4.3 and 4.4. A donor-acceptor distance for AAO - Map Red and AAO - Au has been determined as $\mathrm{r_{DA}} \approx 5.2$ nm and 21.5 nm, respectively. The distance from the donor singly positive oxygen vacancy states to the center of the acceptor QDs is considered as the effective D - A distance for the AAO - Map Red complexation. However, the expected separation of donor and acceptor is supposed to be the radius of Map Red QDs ($\approx$ 3.2 nm) [190]. The donor oxygen centers are estimated to be located within (5.2 - 3.2) nm = 2 nm from the AAO surface boundary in the case that the D - A distance is 5.2 nm in the FRET measurement on an AAO - QD system. Note that the exact position of oxygen vacancy centers in an AAO template is very consistent with the location of defects in ZnO nanoparticles [188, 193, 194]. However, the D - A distance for an AAO - Au system is determined with a much too large value of 21.5 nm compared to the D - A distance between the oxygen vacancy centers and the metal surface. As the donor $\mathrm{F^+}$ center transfers energy to the surface plasmon of the Au nanowires at a distance of 2 nm the validity of FRET in the determination of the D - A distance in the case of an AAO - Au system is doubtful.

Another calculation method, based on nanosurface energy transfer (NSET) [195, 196, 197], is carried out to calculate the D - A separations. The NSET method is based on the model of Persson and Lang [196]. The momentum and energy conservation in the dipole - induced formation of electron hole pairs are of concern in this model. The energy transfer rate is given by the following equation:

$$\mathrm{k_{NSET}} = 0.225 \frac{\mathrm{c}^3 \Phi_\mathrm{D}}{\omega^2 \omega_\mathrm{f} \mathrm{k_f} \mathrm{d}^4 \tau_\mathrm{d}} \ , \tag{4.5}$$

where c is the speed of light, Φ_D is the quantum yield of the donor (0.005), ω is the angular frequency for the donor (4.2×10^{15} $\mathrm{s^{-1}}$), ω_F is the angular frequency

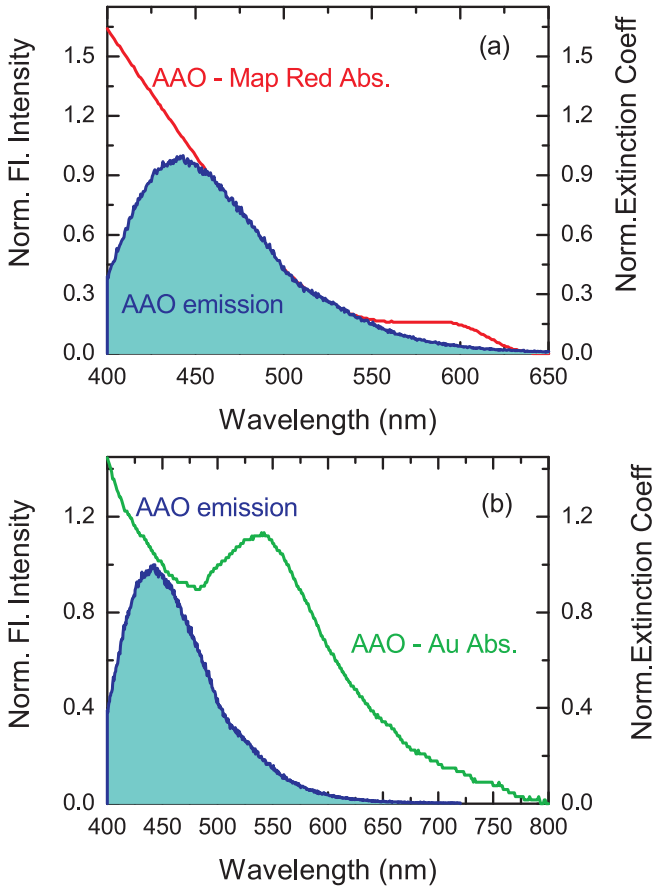

Figure 4.12: (a) Steady state absorption spectra of acceptor Map Red (red) and emission spectra of donor AAO (blue) are shown. (b) Steady state absorption spectra of acceptor gold nanowires (green) and emission spectra of donor AAO (blue). The overlap zones have been shown in light blue, respectively.

Sample	τ_1 (ns)	τ_2 (ns)	τ_3 (ns)	τ_{av} (ns)
AAO	1.47 (46%)	4.54 (48%)	10.5 (6%)	3.49
AAO - BQ	1.42 (49%)	4.54 (46%)	10.5 (5%)	3.30
AAO - Map Red	0.15 (38%)	1.7 (37%)	5.5 (25%)	2.06
AAO - Au	0.79 (37%)	2.9 (50%)	7.8 (13%)	2.76

Table 4.1: Picosecond-resolved luminescence spectra of pure AAO & AAO in the presence of several quenchers.

Sample	τ_1 (ps)	τ_2 (ps)	τ_3 (ps)
AAO	-	44.2 (28%)	1472 (72%)
AAO - BQ	0.40 (59%)	8.4 (6%)	1472 (35%)
AAO - Map Red	0.875 (17%)	12.2 (14%)	1472 (69%)
AAO - Au	-	35.5 (35%)	1472 (65%)

Table 4.2: FS decay periods of luminescence measured with pure AAO& AAO in the presence of several quenchers. τ_3 has been fixed.

for bulk gold (8.4×10^{15} s^{-1}), and d is the distance between donor and acceptor. τ_D is the average lifetime of the donor (3.48 ns), and k_f is the Fermi wave vector for bulk gold (1.2×10^{8} cm^{-1}) [198]. In our experiment, k_{NSET} is defined as:

$$k_{NSET} = \frac{1}{\tau_{donor-acceptor}} - \frac{1}{\tau_{donor}} \quad , \tag{4.6}$$

where $\tau_{donor-acceptor}$ is the average lifetime of the AAO - Au system. Depending on the equations (4.5 and 4.6), the distance between donor and acceptor is 2.7 nm, which is the separation of the oxygen vacancy centers from the Au surface, and the location of the oxygen vacancy centers from the AAO surface is justified ($\approx$ 2 nm from the surface).

From Figure 4.11c, the femtosecond - resolved luminescence transients of AAO - Map Red, it is noted that there is a faster lifetime component of 0.87 ps. We supposed this is related to the excited state of the AAO - Map Red adduct and arises due to charge transfer from AAO to the conduction band of the Map Red quantum dots. In the AAO - Map Red system, both the electron and energy transfer processes are coupled in the deactivation process of the excited AAO. However, the same effects are not detected from the femtosecond - resolved luminescence transients of an AAO - Au system.

4.3 Recrystallization processes

As-prepared AAO templates are amorphous and contain a large number of oxygen vacancies. As described earlier, these oxygen vacancies give a strong photoluminescent signal. In the optical studies of the nanostructures based on AAO templates, this signal might be influenced by the PL of AAO. In order to remove the oxygen vacancies from the templates, we crystallized the templates by annealing. The processes of phase change of AAO with annealing are investigated by X-ray diffraction and Raman spectroscopy.

The templates we measured were prepared in oxalic acid and sulfuric acid which leads to different morphology, as shown in chapter 3. In the pre-treated processes, they are annealed at temperatures between 300°C and 1100°C for 4 hours in air. The X-ray diffraction (CuK_α radiation, λ = 0.15406 nm) patterns

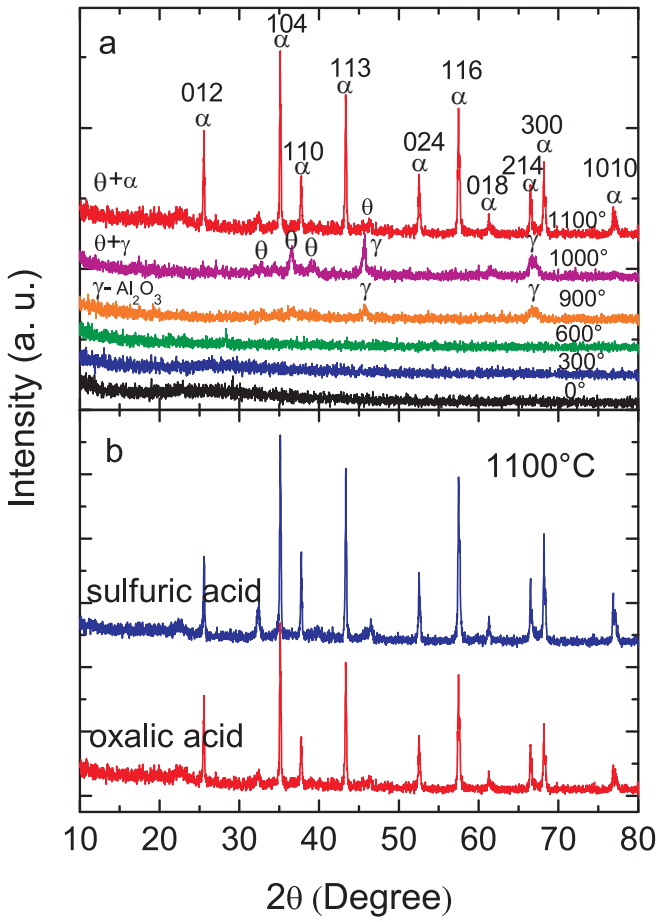

Figure 4.13: a) X-ray diffraction patterns of the as-prepared AAO in oxalic acid and AAO annealed at different temperatures for 4 h in air. Reflexes corresponding to different crystallographic phases are marked. b) X-ray diffraction of the annealed AAO prepared in sulfuric acid and oxalic acid. The annealing temperature is 1100°C.

are given in Figure 4.13 a. The as-prepared templates and the AAO annealed up to temperatures of 600°C are still amorphous. With higher annealing temperatures (900°C), the γ-Al_2O_3 phase appears, indicating a partial crystallization of the AAO. When the annealing temperature is increased even further, crystallization continues and the presence of θ-Al_2O_3 and γ-Al_2O_3 is observed at 1000°C. At 1100°C, a nearly complete phase transformation is achieved with α-Al_2O_3 being the dominant phase. However, other studies have shown that the crystallization and phase transformation temperatures vary as a function of atmospheric and geometrical properties of the AAO templates [187, 199]. With the ongoing crystallization process, the oxygen vacancies vanish quickly, which is shown using

the absorption spectra, see Figure 4.3.

In our experiments, the phase transition of templates prepared in sulfuric acid has similar behavior to templates anodized in oxalic acid. The phase completely transforms when the annealing temperature reaches 1100°C. The XRD figure is given in Figure 4.13 b. The diffraction peaks indexed to γ-Al_2O_3 phase appear, indicating the crystallization of AAO at 1100°C.

The recrystallization behavior of AAO annealed at high temperatures induces a smaller intensity of PL and absorption as well as a change of the morphology of AAO, as shown in Figure 4.2. The recrystallization of AAO is also proven by the Raman spectrum in Figure 4.14. The measurements are conducted at room temperature using a 532 nm laser as excitation. The template anodized in oxalic acid is annealed at 1100°C in the air. Sapphire (α-Al_2O_3) has seven Raman modes [200], and all of them can be observed in this spectrum. The modes are at 418 and 645 cm^{-1} for the A_{1g} and 379, 430, 448, 577 and 751 cm^{-1} for the E_g modes. The blue shift of phonon modes compared to sapphire is caused by the uniaxial pressure from the crystallization process [201]. In the Raman spectra of annealed templates, a small blue shift also appears with respect to bulk sapphire. This is induced by different tensile or stretch stresses during the recrystallization process.

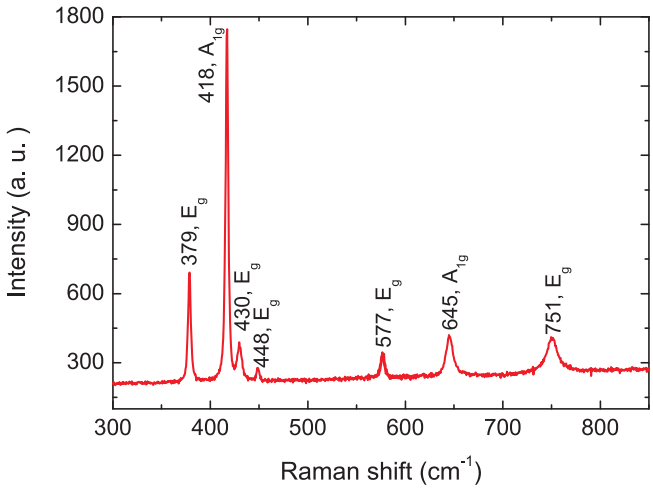

Figure 4.14: Raman spectrum of an AAO template annealed at 1100°C.

The Raman spectra of as-prepared templates and templates annealed at low temperatures only show strong PL signals, because of the oxygen vacancies and the impurities produced during the anodization process.

Chapter 5

Surface plasmon resonance of Au nanowire arrays

5.1 General remarks

As introduced in the second chapter, Au nanowires exhibit strong surface plasmon resonance (SPR) signals with strong anisotropy. The optical properties of Au nanoparties, e. g., gold nanowires [60, 61] and nanoprisms [202] have been reported earlier. The unique coherent oscillations of the electrons from the interaction of single Au nanowires with electromagnetic fields dominate the optical properties of the Au nanowires arrays. This has attracted a significant amount of attention recently. Studies focused on the metal dimers [203], chains [204], and 3D assemblies [205] of plasmonic structures.

In this chapter, we will show the experimental results of the SPR from Au nanowire arrays, which depend on the geometry of nanowires and preparation conditions. The simulation of SPR is carried out based on the finite element method. The results are in qualitative agreement with the experimental results. Results of our investigation of surface plasmon of Au nanowire arrays have been published [206].

Au nanowire arrays are obtained by electrochemical deposition in an AAO template, which is introduced in chapter 3. The geometry of the nanowires is controlled by the nanoporous arrangement of the AAO templates, such as the wire diameter and inter wire distances. The length of nanowires is dominated by the deposition time; briefly, the growth rate is about 2 nm/s. The nanowires are imaged by a scanning electron microscope (SEM).

5.1.1 Absorption spectroscopy

Optical absorption has been used to identify the plasmon energies. The modes are differentiated using the polarization and its angle dependence.

5.1.2 Aspect ratio dependence of SPR

The UV-visible absorption spectroscopy is used to measure the SPR of the gold nanowire arrays, which shows the maximum intensity at a specific electron oscillation energy.

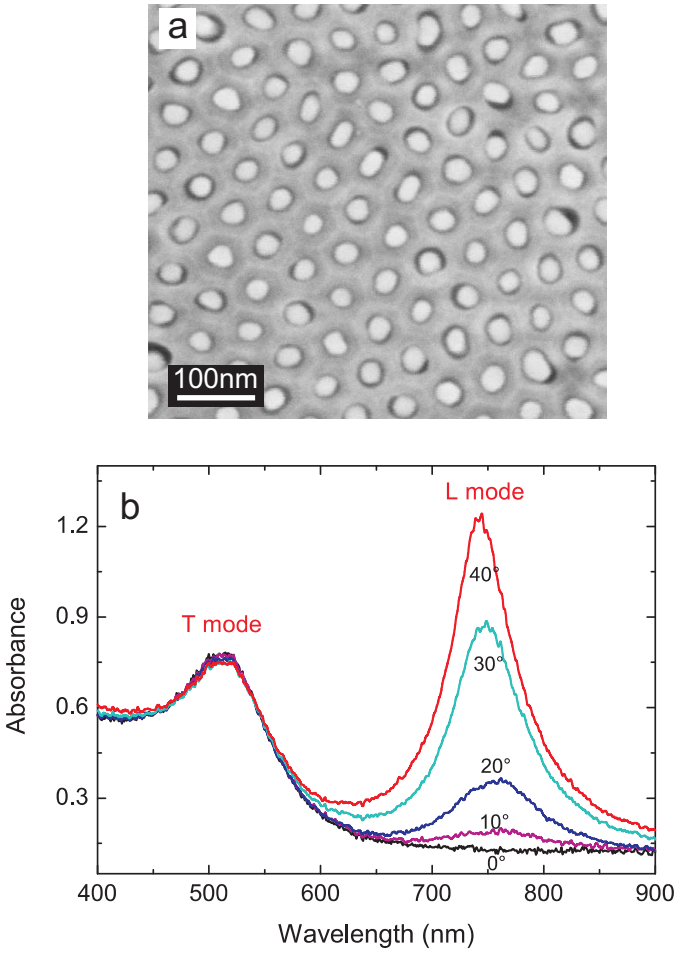

Figure 5.1: a) SEM image of the Au nanowire array in an AAO template. b) UV-visible absorption spectrum of Au nanowire arrays in an AAO template as a function of angle incidence. The incident light is p polarized.

Figure 5.1 (a) is the SEM picture of a typical Au nanowire array in an AAO template. The arrangement of all wires is controlled by the pores, which are parallel to each other and perpendicular to the template surface. The wire diameter and inter wire distance are 25 nm and 30 nm, respectively. The absorption spectra only contain one single peak at around 510 nm, in case of a normal incident or s polarized incident (the electric field of light oscillates perpendicular to the long axis of the nanowires). This resonance is associated with the transverse (T)

mode, which is induced by the electron oscillations along the short axis of the nanowires. However, there are two peaks in the spectra when the incident is oblique with p polarized incident (the electric field of light has a component both parallel and perpendicular to the long axis of the nanowires): T mode and longitudinal (L) mode, which is associated with the oscillation of electrons along the long axis of the nanowires. The L mode becomes prominent with the increase of the angle of incidence because of the enhancement of the electric field component along the long axis. The angular sensitivity of the L mode shown in Figure 5.1 (b) illustrates the strong anisotropy of the structure generated by the orientation of the nanowires. In fact, both of the T mode and L mode energy positions originate from the strong electromagnetic (EM) field coupling between the long axis dipoles of isolated nanowires within the arrays. Later, the simulation results show that the L mode of a single nanowire appears around 2 μm. The coupling of the long axis dipole is also confirmed by the simulation of the EM field distribution along the nanowires in the later part of this chapter. The field is located on the extremities of single wires, while a maximum of the field appears on the middle part of the wire arrays.

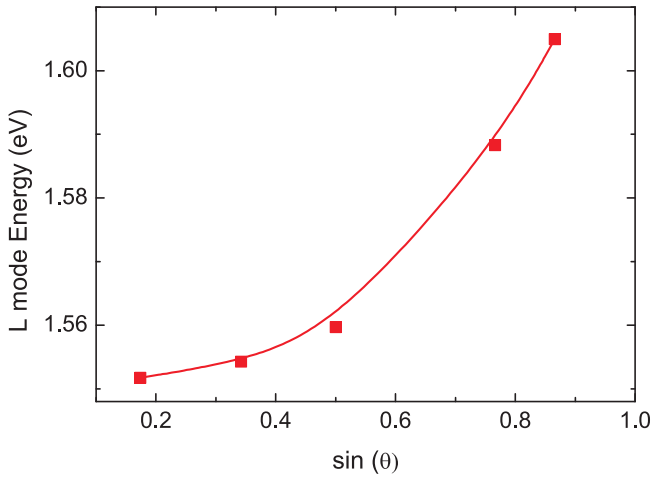

Figure 5.2: Angular dispersion of the L-mode for incidence angles varying from 10° to 60°.

As we see in Figure 5.1 (b), the L mode energy is also related to the angle of incidence, and it shifts to higher energies with an increase of incident angle. The angular dispersion of the L mode is shown in Figure 5.2, and it depends on the coupling strength between the nanowires. With the increase of the effective inter wire distance d', which is defined by the dielectric constant of the medium surrounding the nanowires ϵ and the inter wire distance d [208], the coupling strength decreases [207].

The L mode energy strongly depends on the aspect ratio and the inter rod

distance in the array, which is confirmed by the influence of the shape and geometry [53], and on the dielectric constant of the surrounding material. The shape polarizability of a single wire is given in equation 5.1 [53].

$$\alpha = \frac{\varepsilon_0 \mathrm{V}}{\mathrm{L}} \left(\frac{\varepsilon - \varepsilon_\mathrm{m}}{\varepsilon + \left(\frac{1+\mathrm{L}}{\mathrm{L}}\right) \varepsilon_\mathrm{m}} \right) \tag{5.1}$$

L is a depolarization factor, which is related to the shape of the nanoparticles, V is the volume of the nanoparticles and ε_m is the dielectric constant of the surrounding material.

A red shift of the L mode energy upon an increase of the dielectric constant is observed because the negative real part of the Au dielectric funcition increases with increasing wavelength [61]. Meanwhile, a reduction of the restoring force is caused by the increasing aspect ratio, which can lower the L mode resonance energy [76]. All these results take place within a single nanowire, and there is no other electric field influence except the incident light. In case of a nanowire array, the strong coupling of the electromagnetic field between nanowires dominates the optical properties because of the limited inter wire distance that is realized in the prepared arrays [80, 209, 210, 211].

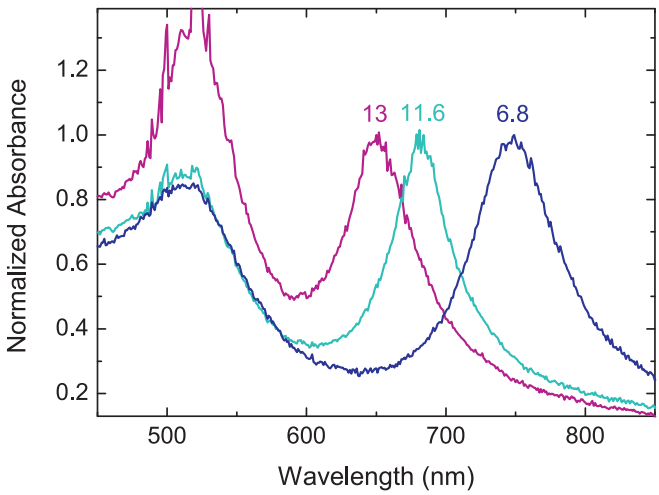

Figure 5.3: Absorption spectra of Au nanowire arrays in an AAO as a function of wire aspect ratio.

The SPR behavior of Au nanowire arrays as a function of aspect ratio is illustrated in Figure 5.3. The L mode position shows an obvious blue shift as the aspect ratio increases, while the T mode energy is relatively stable. The inter wire distance and wire diameter are 35 nm and 25 nm, respectively. The length of the nanowires is tuned by the deposition time in our experiments, which defines the aspect ratio as 13, 11.6 and 6.8. However, the SPR of a single nanowire with the

same aspect ratio gives a longitudinal resonance at a much longer wavelength compared to a nanowire array [212, 213]. The following equation was given by Jain [214] to describe the electric field E′ surrounding each nanowire as the sum of the electric field from the neighboring nanowires and the incident electric field E.

$$\mathrm{E}' = \mathrm{E} + \xi \frac{\mu}{4\pi\varepsilon_{\mathrm{m}}\varepsilon_0 \mathrm{d}^3} \quad , \tag{5.2}$$

where μ is the dipole moment due to the wire plasmon and ξ is an orientation factor. The electric field localized on the nanowire surface is enhanced due to the interaction of the plasmon oscillations.

The dipole-dipole interactions [216, 217] of the individual chromophores in the arrays is described by an exciton coupling theory, which is comparable to a dimerization aggregation of organic molecules and its effect on the optical properties [215]. In this sense the arrangement of nanowires in the assembly is analogous to the H aggregation of the organic molecules [215]. There are two states generated from the coupling of the monomer depending on the arrangement of the dipoles in the dimer, one lower energy level and one higher energy level relative to the excited state of the monomer. The energy splitting 2U is considered as a Coulomb interaction between the interacting monomers. The angle and the distance between the dipoles 1 and 2 influence the quantity of U [218]:

$$\mathrm{U} = \frac{1}{4\pi\varepsilon_0} \frac{|\mu|^2}{\mathrm{n}_{\mathrm{m}}^2 \mathrm{R}^3} \xi \quad , \tag{5.3}$$

where ξ is the orientation factor ξ = cosθ_{12} - 3cosθ_{1R}cosθ_{2R}. For parallel dipoles, such as nanowires in the assembly, θ_{12} = 0°, θ_{1R} = θ_{2R} = 90°, and ξ = 1; $\mathrm{n_m}$ is the refractive index of the surround medium; μ is the transition dipole moment and R is the distance between the dipole centers.

In a 3D Au nanowire array with a hexagonal arrangement, when the inter wire distance between two adjacent wires is 32 nm, the inter wire distance between two next-nearest neighbor wire is only about 60 nm. The sum electric field of every wire is from the overlap of all adjacent wires and next-nearest neighbor wires. When the inter wire distances decrease further, the number of wires which influence the sum electric field dramatically increases and the energy splitting 2U′ becomes broader. The schematic of the energy level splitting resulting from the electric fields interaction of nanowires is shown in Figure 5.4 [208, 213, 216, 219].

$$\mathrm{U}' = \mathrm{U} + \frac{1}{3\sqrt{3}}\mathrm{U} + \frac{1}{8}\mathrm{U} + \cdots \tag{5.4}$$

For parallel nanowires, the spectrum only consists of a single, higher energy band (L mode energy) because the electron transition to the lower energy excited state is forbidden [73]. The interaction between the nanowires is repulsive, as in Figure 5.4. In the absorption spectra, we observe the blue shift of the L mode

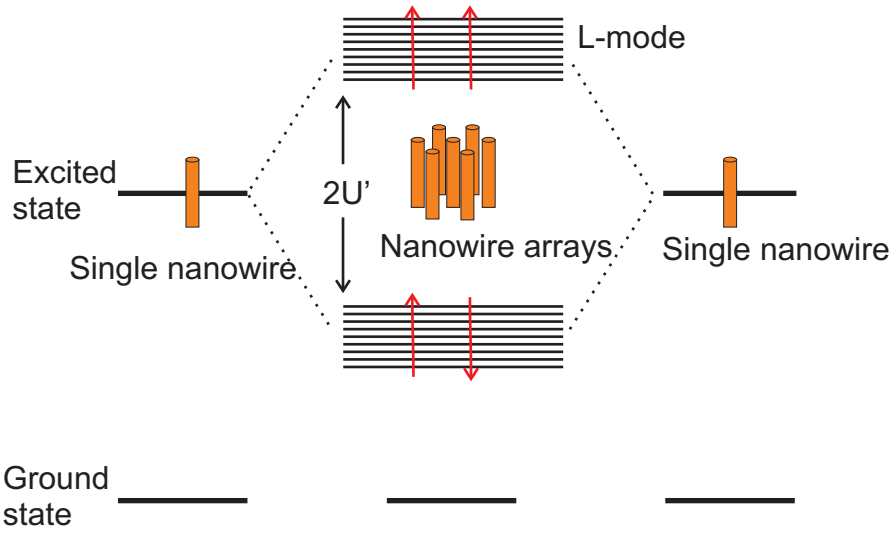

Figure 5.4: Energy diagram of the plasmonic resonances in the Au nanowire arrays with respect to a single nanowire. The arrow is direction of dipole moment.

energy from the Au nanowire arrays with respect to the L mode from the single nanowire.

In our experiment, the Au nanowire is deposited on the Ag film evaporated on the bottom of the pore. Then the Ag film is removed chemically or mechanically. An oxidation of Ag into Ag^{+} may take place when the Au^{3+} touches the Ag film before the electrochemical deposition starts, as equation 5.5 describes.

$$3\mathrm{Ag\,(s)} + \mathrm{AuCl_4^-\,(l)} \rightarrow \mathrm{Au\,(s)} + 3\mathrm{AgCl\,(s)} + \mathrm{Cl^-\,(l)} \quad . \tag{5.5}$$

This reaction leads to the formation of a mixed AuAg film on the bottom of the pores. Next the Ag is resolved by HNO_3, and the nanowires are connected on the top part by the remaining Au network. Figure 5.5 left, gives the top view structures of the nanowires in AAO templates; and the white lines in the figure are Au, the black dots are empty pores, and the white dots are the tops of nanowires.

The spectrum of the connected Au nanowire arrays shows an obvious blue shift of the L mode, and the L mode almost overlaps with the T mode, as shown in Figure 5.5 right. The spectrum is divided into two subbands, one of which relates to the T mode resonance located at 510 nm, while the other relates to the L mode resonance located at 560 nm. We assume that the blue shift of the L mode resonance energy stems from an additional pathway for electrons between different nanowires, which is provided by the Au network between the isolated Au nanowires in the AAO templates.

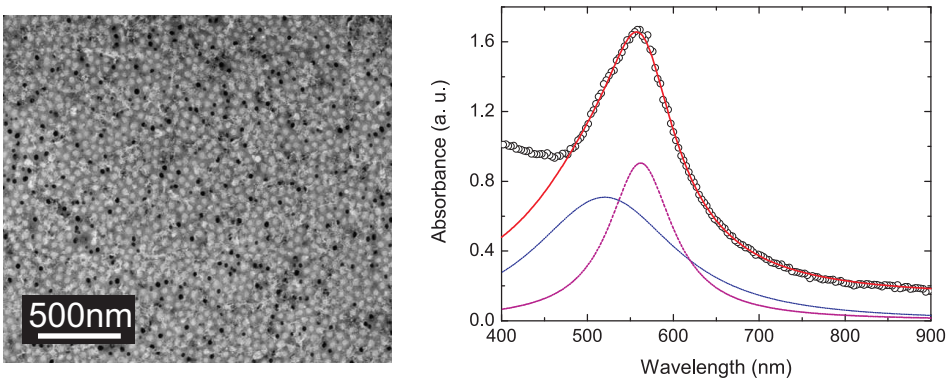

Figure 5.5: Absorption spectra of Au nanowire arrays with connected wire tops in AAO .

5.1.3 Annealing and etching dependence of SPR

The L mode SPR frequency of the Au nanowire arrays depends not only on the aspect ratio, the coupling strength between wires, and the geometry as we described in the last section, but also on the dielectric properties of the surrounding materials [207, 220]. Many groups have studied the optical sensitivies of noble nanoparticles in different dielectric solvents. For instance, Papavassiliou [221] observed the color sensitivities of the Cu, Ag and Au nanoparticles in the solvent with various refractive indices; Ghosh et al. [220] studied the shift of the local surface plasmon resonance spectrum from the Au nanoparticles in an alternate refractive index of the solvent.

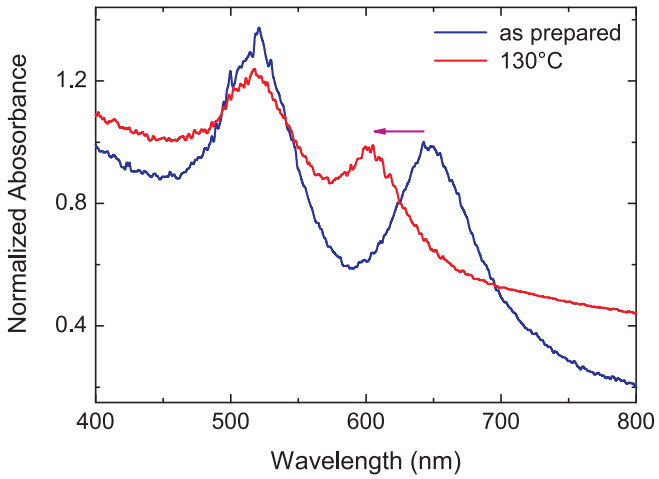

Figure 5.6: Absorption spectra of as-prepared and annealed at 130°C Au nanowire arrays in AAO.

To obtain a uniform air shell around the Au nanowires, the Au nanowire arrays in AAO templates are annealed at 130°C for 4 hours in the air. As we described in the previous chapter, the weight loss after annealing AAO templates at lower than 200°C is induced by the moisture removal from AAO. The evaporation of H_2O results in a shrinking of the alumina volume, which forms an additional air shell around the Au nanowires. Figure 5.6 gives the absorption spectrum of the as-prepared and annealed Au nanowire arrays. The L mode frequency shows an obvious blue shift after annealing because the dielectric constant of air ($\varepsilon_{\mathrm{air}} \approx 1$) is significantly smaller than the dielectric constant of AAO ($\varepsilon_{\mathrm{AAO}} \approx 2.56$).

Depending on the polarizability of Au nanoparticles [58, 59] under an incident, the SPR takes place at around ε_r = -2ε_m, which is given in equation 2.17. The real part of the dielectric function of Au nanoparticles determines the resonance frequency. When the dielectric constant of the surrounding medium ε_m is changed, the resonance frequency shows a shift. In the simulation part, a quantitative shift is also observed after altering the ε_m.

5.2 Results of finite element method simulation

JCMsolve developed by ZIB in Berlin is used to simulate the SPR of Au nanowire arrays. It is based on the finite element method. The models of nanowire arrays and a single nanowire are described in section 3.5. Three dimensional Au cylinders with infinite numbers are inserted in a dielectric medium. The incident source is p polarized, and the dielectric function of Au is defined by the Drude model. In this section, the simulation results as a function of inter wire distances, alteration of the dielectric medium, and the aspect ratio of nanowires are described, depending on the simulated absorption spectrum. The distribution of the electromagnetic field of Au nanowire surface plasmon along the XY profile and YZ profile respectively are also given.

5.2.1 Plasmon coupling strength dependence on inter wire distance

The L mode energy, dependent on the inter wire distance, is shown in Figure 5.7. In the simulation model, the length and diameter of wires are 200 nm and 25 nm, respectively, with a dielectric constant of the AAO ε_{m} = 2.56. The incident angle is set to 50° with p polarized, which can excite the L mode. The influence of the inter wire coupling strength is investigated by tuning the inter wire distances from 148 nm to 27 nm. For the larger inter wire distance 148 nm, the L mode locates at 2175 nm. When the inter wire distance is reduced to 27 nm, the L mode energy moves to 934 nm. Reduction of the inter wire distance leads to an apparent blue shift of the L mode energy, as shown in Figure 5.7a. With reference to the L mode resonance energy, the distribution of the electric field along the long axis of the wires is shown in Figure 5.7b. When the wires are far apart (inter wire distance is larger than 80 nm), the field localizes on both wire extremities with a

symmetric distribution and illumination. The model is analogous to a single wire embedded in the dielectric AAO medium. However, the field distribution moves to the middle part of the wires as the the inter wire distances decrease and the field strength at the wire's extremities simultaneously decreases. The dielectric constant of the whole structure becomes a complex number with a negative real part [208]. The results of the field distribution proves that the strong coupling of the field between the wires is responsible for the optical response of the arrays, and that the surface plasmon can effectively propagate from wire to wire when the inter wire distance is small enough. In contrast to the L mode behavior when decreasing the inter wire distance, the T mode energy only shows a small red shift, which can not be investigated in the experiments because of the accuracy of the instrument.

5.2.2 Plasmon frequency dependence on the dielectric constant

The electric field distribution around the single Au nanowire is calculated. The incident source, the length, and the diameter of wires are the same as those in the arrays. The thickness of the surrounding AAO medium is set to 13.5 nm, as for the nanowire with the inter pore distance of 27 nm. The field distribution localizes with the incident field on the extremities of wire. The field strength and illumination is much lower than in arrays, as shown in Figure 5.7b.

The experimental results show that the dielectric constant ε_{m} of the surrounding medium exerts a strong influence to the L mode energy, which is described in section 5.1.3. A red shift of the L mode is observed as ε_{m} decreases. An analogous behavior of the L mode is proven by the simulation. In the computation, ε_{m} is altered from 1.56 to 4, and the L mode energy shifts from 2.5 eV to 0.97 eV, as shown in Figure 5.8 a. The electric field distribution around the nanowires is given in Figure 5.8 b. We can see that the electric field located on the bottom end of wires becomes weaker with increasing ε_{m}, and a stronger field appears at the middle part of the wires. These results are essentially in accordance to our experimental investigation and motivate further studies using decorated wires with core shell structures.

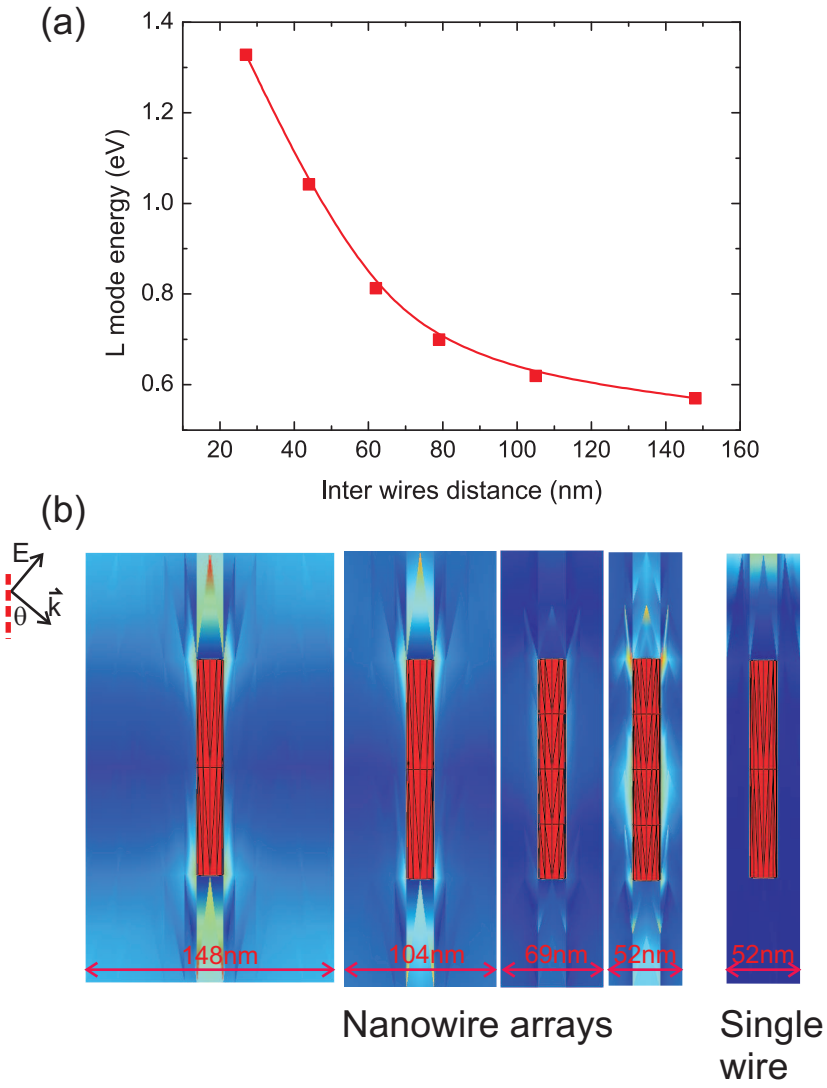

Figure 5.7: a) L mode energy shift of the SPR from Au nanowire arrays as a function of the inter wire distance. b) Electric field distribution of L mode in the Au nanowire arrays for different inter wire distances, and the electric field distribution of L mode in a single Au nanowire surrounded by AAO.

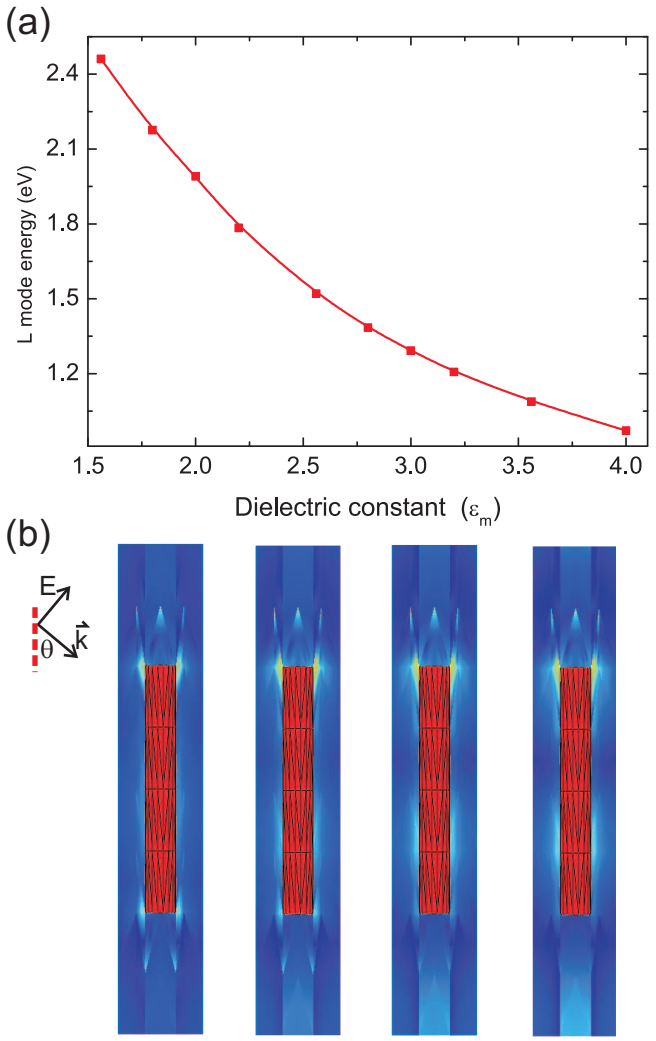

Figure 5.8: a) L mode energy shift of the SPR and b) Electric field distribution of L mode from Au nanowire arrays as a function of the dielectric constant ε_{m} of the surrounding medium. The ε_{m} are 1.56, 2.2, 3, and 4, from the left to right respectively in figure b).

Chapter 6

Plasmons touch molecules

Over the last decades, great developments have been made in the field of biosensors for the application of environmental monitoring, food control, and medical diagnostics [222, 223, 224]. Surface plasmon resonance (SPR)- based biosensors take advantage of the sensitivity of SPR to the molecules [225]. For instance, some biomolecules can be captured by the surface of a noble metal, the binding of which alters the refractive index. This behavior can be observed by the spectroscopy of the SPR [225]. The fluorescence signal from molecules can also be enhanced by the strong local electric field of the SPR [226]. Research on potential biosensing applications [243] is demonstrated by the Alivisatos group, and Sönnichsen [244] who described a "molecular plasmon ruler".

With the development of SPR applications, many theory models have been developed to study the interaction between SPR and molecular excitations. Matsubara presented long range surface plasmon (LRSP) theory [227], Chien described a mode of surface plasmon coupling with a dielectric waveguide [228], and Dostalek presented the Bragg-scattered surface plasmons [229]. These models are usually employed to illuminate specific interactions. We demonstrated the optical spectrum of the SPR from the AAO - Au nanowire arrays in the previous chapter. The longitudinal mode (L-mode) position from the sample is tunable by the aspect ratio and the geometries of the arrays. In this chapter, different molecules are put on the surface of Au and their optical properties are detected to investigate different interaction behaviors between the SPR and molecules.

6.1 Photoluminescence enhancement by MgPC

Fluorescent organic dyes are notably employed as a probe or indicator due to the high sensitivity to the environment. When the dye molecules are doped into various hosts, attractive properties are used for optical data storage, optical sensing, or photocatalysis [230, 231, 232]. Nanoporous hosts provide a specific environment for the molecules because of the confined space of the pores, the large surface areas, and well-defined pore arrangement [233]. Quantum efficiency of light

emission is considered the most important requirement for an efficient fluorescent biosensor. Surface plasmon coupling is available as one of the most advanced techniques to enhance efficiency of the dye emission [234, 235, 236].

For our experiments, magnesium Phthalocyanine (MgPC) is provided by Prof. K. Morgenstern's group at the Institute for Solid State Physics, LU Hannover. The molecules are investigated by dipping the AAO - Au arrays into solution. MgPC is widely used in copy and printer systems [237, 238] because its absorption and emission spectra are located in the red spectral range. Figure 6.1 gives the absorption and emission spectrum of MgPC in PrOH. The molecular structure is also shown in the inset of Figure 6.1. The absorption spectrum of MgPC in PrOH contains three peaks at around 604, 638, and 668 nm. The emission spectrum also contains three bands at around 671, 704, and 742 nm. From literature, the ground electronic 0 - 0 transition in MgPC is attributed to the strongest peak [241, 242], and relatively weak peaks are due to the electronic vibrational transitions.

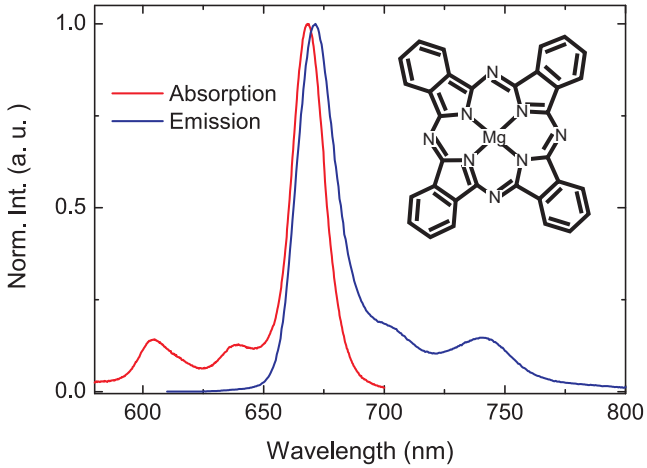

Figure 6.1: Emission spectrum of MgPC in PrOH and schematic molecular structure of MgPC [239, 240].

The AAO template was anodized in sulfuric acid with a pore diameter around 25 nm. Before the deposition of Au nanowires, a Ag film was deposited on one side of the template as a working electrode. Then the Au nanowires were deposited by a standard three-electrode system. The Ag film was dissolved after deposition, which means the Au nanowires are free standing in the pores. Then, the sample was immersed in a MgPC molecular solution with a concentration of 1.86×10^{-3} mol/L for 1 hour. The PL spectrum was investigated after drying the sample in the air. The excitation wavelength was 370 nm. The PL results of pure AAO templates, AAO - MgPC, and AAO - Au - MgPC are shown in Figure 6.2.

Pure AAO templates exhibit a very strong fluorescence signal at around 450 nm, which is induced by the oxygen vacancies in AAO templates formed during the anodization process. When the surface of pure AAO is decorated with the molecules, the intensity of the PL peak from AAO shrinks a little bit, while a new

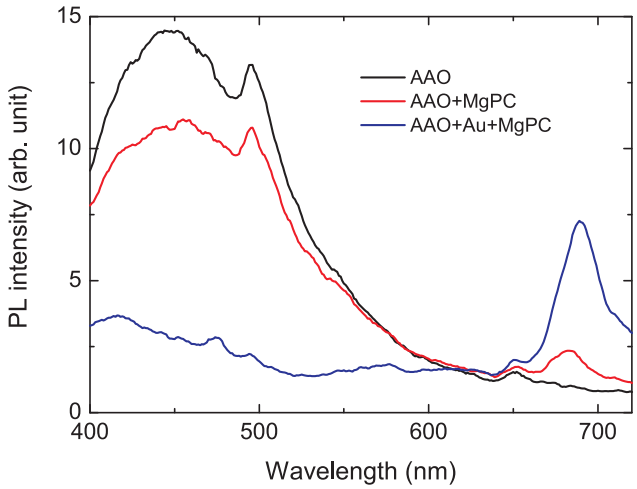

Figure 6.2: Photoluminescence spectra of bare AAO template and Mg - phtalocyanine on different substrates.

PL signal caused by the MgPC appears at around 680 nm. The PL spectra of AAO - Au - MgPC show a strong enhancement of the peak at 680 nm. Meanwhile, the fluorescence peak at 450 nm vanishes. The maximum intensity of the PL of MgPC from the AAO - Au substrate is approximately 3 times larger than that from the AAO substrate. Therefore, the pure AAO templates cannot effectively enhance the PL of MgPC, while the presence of Au nanowires plays a crucial role in the enhancement of the molecular PL.

Previous studies indicated that the electromagnetic density of states can be enhanced by the surface plasmon excitation and that the emission rate of semiconductor and organic materials can be increased as well [245, 246]. However, there are two processes. A nonradiative energy transfer from the molecule to the metal induces a quenching of molecular luminescence, while the presence of a local field enhances the excitation rate [247, 248]. In our case, the nonradiative energy transfer is the dominating process. Therefore, the luminescence quenches when the molecule directly touches the noble metal surface. The dielectric constants of the metal, the surrounding material, and the emission wavelength influence the effective length between the molecules and the metal surface [246]. Therefore, we concluded that most of the MgPC molecules were located on the AAO template surface instead of being absorbed onto the Au surface in our experiments. The increased radiative rates for molecules near the Au nanowires due to the coupling of surface plasmons generated on the Au nanowire is attributed to the enhancement of PL. The quenching of the fluorescence at 450 nm is attributed to the energy transfer between Au nanowires and AAO templates, which was discussed in the last chapter.

6.2 Electron transfer between Aza-BODIPY and Au nanowires

When organic molecules and an inorganic noble metallic surface are combined in a nanostructure, unique functionalities become possible because of the coupling between surface plasmons and the excitons [249, 250]. The absorption of photons creates electrically neutral electron - hole pairs in the organic molecules. The excitonic states of molecules are widely used to store and guide energy for energy conversion, which contributes to the preparation of artificial devices. BODIPY derivatives currently attract a significant amount of attention for organic solar cell applications [251, 252] because of their convenient synthesis. In our experiments, we investigate Aza-BODIPY for the coupling of surface plasmons. Figure 6.3 shows the absorption and emission spectra of Aza-BODIPY. We found the maximum absorption peaks of Aza-BODIPY on pure AAO templates has the same position as in the solvent.

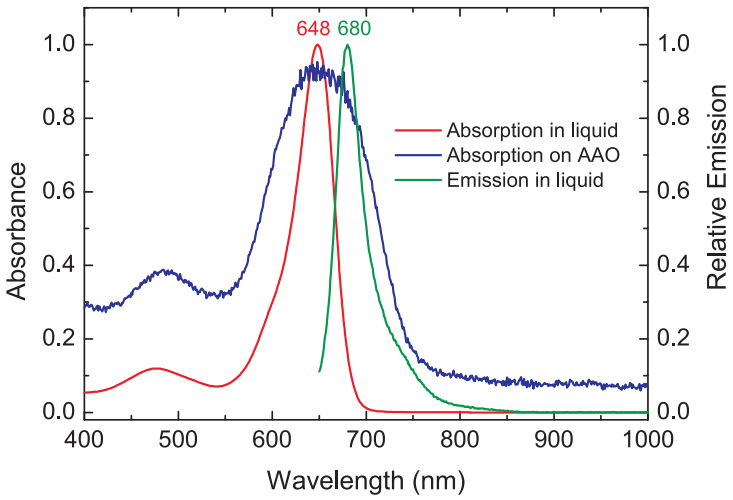

Figure 6.3: The absorption and emission spectra of Aza-BODIPY. The blue line is the absorption spectrum of Aza BODIPY on as-prepared AAO templates.

Au nanowire arrays provide plasmonic fields. The preparation of Au nanowires arrays was described in the previous chapter. The Au nanowires are grown in the AAO templates, by electrochemical deposition. Then the Ag layer is dissolved by HNO_3. In this section, the templates with a diameter of 25 nm and pore distances of 25 nm were employed. The diameter and spacing of nanowires are decided by the geometry of the AAO templates. The rod length can be tuned using the deposition time. The nanowire arrays are strongly uniaxially anisotropic with wires parallel to each other and perpendicular to the surface of the templates. The optical properties of the Au nanowire arrays can be tuned by the aspect ratio of wires in the red and near infrared range. As shown in Figure 5.1, the absorption spectra consist of two resonances, the L mode and the T

mode. Aza BODIPY was diluted in chloroform to prepare a solution. Then a 6 μL Aza-BODIPY solution with concentration of 1×10^5 mol/L was dropped on the surface of Au-AAO. The templates were then dried in the air before optical investigations. Previous studies proved that a space was left between the Au nanowires and the pore walls after dissolving the Ag layer [125], which means the molecules can be absorbed onto the Au nanowire surface after chloroform evaporation.

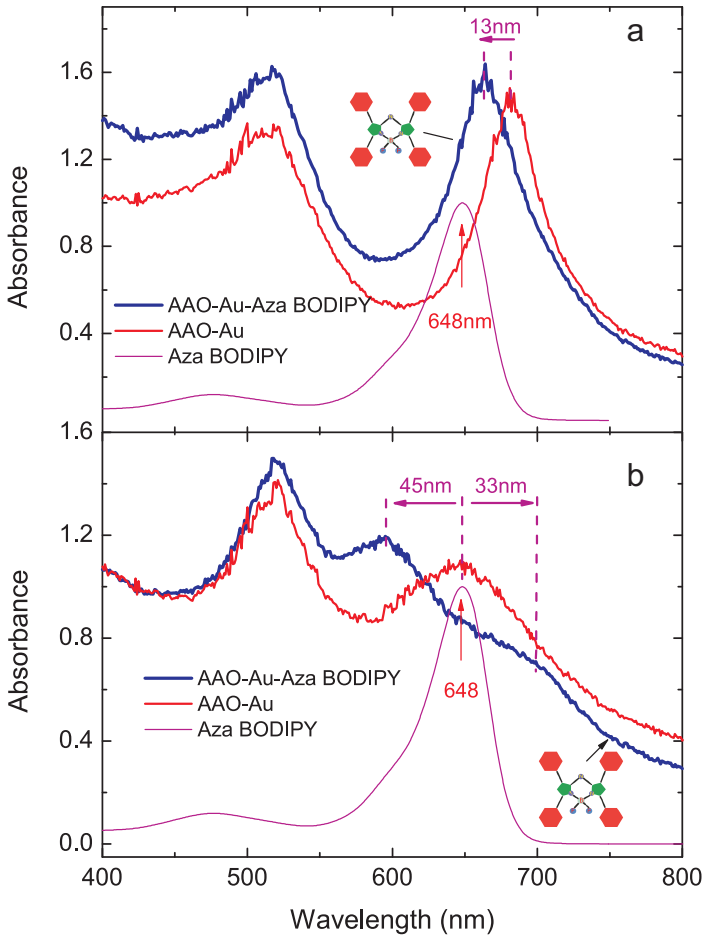

Figure 6.4: a) Absorption spectrum of the hybrid Au nanowire arrays with weak plasmon-exciton coupling. b) Absorption spectrum of the hybrid Au nanowire arrays with strong plasmon - exciton coupling.

We used Au-AAO matrices with L mode plasmonic resonances at 647 nm and 682 nm as substrates to investigate the coupling strength as a function of overlap area between plasmons and excitons. Figure 6.4a and b show absorption spectra of hybrid systems. When the overlap area is small, weak coupling is observed, as shown in Figure 6.4a, the L mode plasmonic resonance wavelength is λ = 682 nm and the exciton wavelength of a molecule is λ = 648 nm because the hybrid sys-

tem is determined by the resonances of the isolated systems. Conversely, figure 6.4b shows a strong coupling behavior. The L mode plasmonic resonance wavelength is λ = 648 nm and overlaps with the molecular excitons. The hybrid states show a pronounced decrease at 648 nm because the Au electronic polarization is scrambled by the exciton transition dipole of the molecules [253, 254].

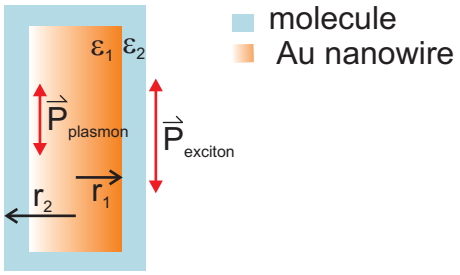

Figure 6.5: Sketch of the electronic polarization in Au nanowires with the excitonic polarization of molecules. [253]

Figure 6.5 shows a model of the nanowire coated with molecules. In the frequency range of interest, the interaction between electronic dipoles and excitonic dipoles takes place. The absorbance peak frequency depends on the effective polarizability α_{eff} of the hybrid system, which is defined by the effective dielectric constant ε_{eff} [253]. The following equations present expressions for the quantities of α_{eff} and ε_{eff} as obtained from Mie scattering theory [53, 253].

$$\varepsilon_{\text{eff}} = \frac{\varepsilon_2}{\varepsilon_{\text{m}}} \frac{(\varepsilon_1 + 2\varepsilon_2) + 2(\varepsilon_1 - \varepsilon_2)(\text{r}_1/\text{r}_2)^3}{(\varepsilon_1 + 2\varepsilon_2) - (\varepsilon_1 - \varepsilon_2)(\text{r}_1/\text{r}_2)^3} \quad , \tag{6.1}$$

$$\alpha_{\text{eff}} = 4\pi\varepsilon_{\text{m}}\text{r}_2^3 \frac{\varepsilon_{\text{eff}} + 1}{\varepsilon_{\text{eff}} - 2} \quad , \tag{6.2}$$

where ε_1 and ε_2 are the dielectric constants of Au and the molecules, and ε_m is the dielectric constant of the surrounding medium. The sum of the intraband transitions (free electronic motions in the conduction band) and interband transitions (electronic transitions between the valence band and the conduction band) dominates the dielectric constant of the metal ε_1. When the excitonic transitions of molecules coherently couple with the interband transitions, strong coupling takes place [253]. In other case, the excitons couple to the free electrons and weak coupling takes place [253]. The asymmetry, hybrid peak shape and larger bandwidth are due to the inhomogeneous local field on the particle surface.

In Figure 6.4, only the L mode was observed to couple with the excitons of molecules and produce the hybrid state. In our experiments, the L mode energy was modified by the aspect ratio to tune the overlap between the plasmon resonance energy and the transition energy of molecule, which directly influence the coupling strength. Four hybrid states would be observed if both T mode and L

mode of SPR from Au nanowire arrays were to be coupled with the excitons of molecules [254].

These studies show that that excitation dynamics of the composite AAO-Au-molecule can be tailored to a big extend via spectral overlap. The spectra overlap is again tuned by size effects. Thereby the advantageous properties of nanoscale materials are demonstrated.

Chapter 7

Summary

In this thesis we further developed the preparation techniques of AAO, including the fabrication of free standing AAO as well as ultra thin AAO. The pore size and geometry have been controlled by the type of electrolyte and anodization voltage. Free standing templates have the advantage that they can be used in simple transmission or diffusion experiments. Open pores allow transport and the growth of nanoscale objects. On the other side, free standing templates tend to a geometrical waviness that prevents scanning probe investigations or nonlinear optics with full resolution. To circumvent such problems, we have used argon ion etching to flatten the templates. Ultra thin AAO templates have the advantage that they can be used as a mask to prepare quantum dots on a flat surface.

Within the free standing AAO templates, arrays of metallic nanowires have been deposited by electrochemical methods. Spinel nanowires have been prepared by sol-gel methods. Metallic nanodots with plasmonic properties have been deposited on Si wafers using ultra thin AAO as a mask. Meanwhile, the structural and physical properties of AAO have been tailored to a certain extend.

The physical properties of AAO templates have been studied using optical spectroscopy, X-ray diffraction (XRD) and Raman spectroscopy. Oxygen vacancies in AAO give a strong blue emission signal, which indicates that the templates could be a good host for energy transfer studies. Different organic molecules and semiconducting quantum dots have been doped into AAO to evaluate the role of Förster resonance energy transfer on picosecond and femtosecond resolved photoluminescence. This has been performed in collaboration with the group of S. K. Pal, Kolkata, India. Optical absorption spectra give information about changes of oxygen vacancy density, e.g. as a function of annealing temperature. The structure evolution has been independently checked by XRD measurements.

Plasmonic excitations of Au nanowire arrays are detected in the optical absorption. Sharp maxima at different energies define longitudinal and transverse modes. These excitations also have different polarization selection rules. The frequency, linewidth and coupling strength of the longitudinal plasmons have been tailored by the aspect ratio and other geometrical factors of the Au nanowires.

Calculations of the electric field distribution in the nanowire arrays have been performed using a finite element method in collaboration with Dr. S. Burger, Zuse Institute of Berlin (ZIB). The following table gives a summary of the molecules used within this thesis. Combining nanomaterials with biomolecules such as Mg-phtalocyanine and Aza-BODIPY is the basis of studying contacts in nanosystems and their metrological aspects as promoted by our work in the NTH School and the International Graduate School of Metrology.

Table 7.1: Coupling between molecules and nanostructures, used techniques and spectral features

Host	**Guest**	**Manipulation / Type of investigation, etc.**	**Spectral and electronic features**	**Comments**
AAO annealed (1100°C)	Cr^{3+}ions and annealing at 1100°C	PL, Raman	Ruby modes, Al_2O_3 phonon modes	Amorphous AAO is crystallized
AAO	CdSe (Maple red) QD	PL, picosecond PL, femtosecond PL	Abs. of Map Red and PL of AAO (450 nm) show overlap	Förster resonance energy transfer (FRET) from AAO to QDs
AAO	Benzoquinone (BQ)	PL, picosecond PL, femtosecond PL	BQ is an electron acceptor	Charge transfer from AAO to BQ
AAO	Au nanowires	PL, picosecond PL, femtosecond PL	Abs. of Au (520 nm) and PL of AAO (450 nm) show overlap	1. PL of AAO is quenched 2. Nanosurface energy transfer from AAO to Au nanowires
AAO	Au nanowires	Absorption spectroscopy (Abs.)	Spectral shift, Quenching of color center PL	Aspect ratio, surrounding medium influences mode energy
AAO+Au	Mg-phtalocyanine (MgPC)	PL	PL of MgPC is at 690 nm	1. PL of AAO is quenched 2. PL of MgPC is enhanced by the Au nanowire array surface plasmon
AAO+Au	Aza-BODIPY	Absorption spectroscopy	1. Weak coupling: L mode (684 nm) and Abs. of molecules (648 nm) show partial overlap 2. Strong coupling: L mode and Abs. (648 nm) of molecules (648 nm) fully overlap	1. Weak coupling induces the blue shift (13 nm shift) of absorption 2. Strong coupling leads to the formation of two hybrid energy states (596 nm and 700 nm)

Appendix A

Lebenslauf

Persönliche Daten:

Name:	Hongdan Yan
Geburtsdatum:	14 Oktober 1981
Geburtsort:	Rongcheng, Shandong, China
Nationalität:	Chinesisch
Telefon:	0049-17640150535
E-Mail:	hd.yan@tu-bs.de

Ausbildung:

09. 1993 - 07. 1997	Middle school, 21^{st} school of Rongcheng, Shandong, China.
09. 1997 - 07. 2000	High school, 5^{th} school of Rongcheng, Shandong, China.
09. 2000 - 07 2004	Bachelor of Science in Physics, Ludong University, Yantai, China.
09. 2004 - 05. 2007	Master of Materials Science in Physics and Chemistry, Kunming University of Science and Technology, Yunnan, China.
09. 2007 - present	Ph. D student in physics, group of Prof. Peter Lemmens at the Institute for Condensed Matter Physics, TU Braunschweig, Germany.

Mitgliedschaften:

12. 2007 - present	Member of the International Graduate School of Metrology, Braunschweig, Germany.
02. 2010 - present	Member of the NTH School for Contacts in Nanosystems, Germany.

Publikationen:

- *Iron/Nickel nanowire growth in anodic aluminum oxide templates: Transfer of length scales and periodicity*, H. D. Yan, P. Lemmens, H. Dierke, S. C. White, F. Ludwig, and M. Schilling, J. Phys.: Conf. Series, **145**, 012079 (2009).

- *Light Harvesting Semiconductor Core-Shell nanocrystals: Ultrafast Charge Transport Dynamics of CdSe-ZnS Quantum Dots*, A. Makhal, H. Yan, P. Lemmens, S. K. Pal, J. of Phys. Chem. C, **114**, 627 - 632 (2010).

- *Tailoring defect structure and optical absorption of porous anodic aluminum oxide membranes*, H. Yan, P. Lemmens, D. Wulferding, J. Shi, K. D. Becker, C. T. Lin, A. Lak, M. Schilling, J. Mat. Chem. Phys., **135**, 206 - 211 (2012).

- *Ultrafast excited state deactivation of doped porous anodic alumina membranes* , A. Makhal, S. Sarkar, H. Yan, P. Lemmens, D. Wulferding, F. Cetin, S. K. Pal, Nanotechnology, **in print**, (2012).

- *High-density array of Au nanowires coupled by plasmon modes*, H. Yan, P. Lemmens, J. Ahrens, M. Bröring, S. Burger, W. Daum, G. Lilienkamp, S. Korte, A. Lak, M. Schilling, Acta Physica Sinica, **submitted**, (2012).

Bibliography

[1] G. Q. Lu and X. S. Zhao, *Nanoporous materials*, **4**, Imperial College Press, Series on Chemical Engineering.

[2] F. Keller, M. S. Hunter and D. L. Robinson, J. Electrochem. Soc. **100**, 414, (1953).

[3] H. Masuda and K. Fukuda, Science, **268**, 1466, (1995).

[4] A. A. Wang, J. Lee, G. Jenikova, A. Mulchandani, N. V. Myung and W. Chen, Nanotechnology, **17**, 3375, (2006).

[5] G. E. Thompson and G. C. Wood, Nature, **290**, 230, (1981).

[6] L. F. Liu, W. Y. Zhou, S. S. Xie, O. Albrecht and K. Nielsch, Chem. Phys. Lett., **466**, 165, (2008).

[7] A. R. Despic, J. Electroanal. Chem. **191**, 417, (1985).

[8] J. P. O'Sullivan and G. C. Wood, Proc. Roy. Soc. Lond. A, **317**, 511, (1970).

[9] G. E. Thompson and G. C. Wood, *Treatise on Materials Science and Technology*, Academic Press new York, **23**, 205, (1983).

[10] A. Despic and V. P. Parkhutik, *Modern Aspects of Electrochemistry*, Edited by J. O. Bockris, R. E. White, and B. E. Conway, Plenum, New York, Vol. 20, 401, (1989).

[11] J. W. Diggle, T.C.Downie and C. W. Goulding, Chem. Rev. **69**, 365, (1969).

[12] H. Takahashi, K. Fujimoto and M. Nagayama, J. Electrochem. Soc. **135**, 1349, (1988).

[13] A. Pakes, G. E. Thompson, P. Skeldon, P. C. Morgan and K. Shimizu, Trans. IMF. **77**, 171, (1999).

[14] G. E. Thompson, Thin Solid Films, **297**, 192, (1997).

[15] X. F. Zhu, D. D. Li, Y. Song and Y. H. Xiao, Mater. Lett. **59**, 3160, (2005).

[16] A. Mozalev, A. Poznyak, I. Mozaleva and A. W. Hassel, Electrochem. Commun. **3**, 299, (2001).

[17] Y. Jia, H. Zhou, P. Luo, S. Luo, J. Chen and Z. Kuang, Surf. Coat. Technol. **201**, 513, (2006).

[18] S. Shingubara, K. Morimoto, H. Sakaue and T. Takahagi, Electrochem. Solid-State Lett. **7**, 15, (2004).

[19] W. Baumann, Z. Physik, **59**, 102 (1936).

[20] W. Baumann, Z. Physik, **707**, 111 (1939).

[21] J. F. Murphy and C. E. Michaelson, Processding Conference on Anodizing, University of Notthingham, UK, *Aluminum Development Association*, London, 83, (1961).

[22] G. E. Thompson, Thin Solid Films, **297**, 192, 1997.

[23] I. De Graeve, H. Terryn and G. E. Thompson, J. Appl. Electrochem., **32**, 73, 2002.

[24] J. Sieika and C. Ortega, J. Electrochem. Soc., **124**, 883, (1977).

[25] H. Masuda and M. Satoh, Jph. J. Appl. Phys, **35**, 126, (1996).

[26] H. Wu, X. Zhang and K. R. Hebert, J. Electrochem. Soc., **147**, 2126, (2000).

[27] M. Nagayama, K. Tamura and H. Takahashi, Cooros. Sci., **10**, 617, (1970).

[28] L. E. Fratila-apachitei, H. Terryn, P. Skeldon, G. E. Thompson, J. Duszczyk and L. Katgerman, Electrochim. Acta, **49**, 1127, (2004).

[29] L. Zhang, H. S. Cho, F. Li, M. R. Metzger and W. D. Doyle, J. Mater. Sci. Lett. **17**, 291, (1998).

[30] S. Nakamura, M. Saito, L. F. Huang, M. Miyagi and K. Wada, Jpn. J. Appl. Phys., **31**, 3589, (1992).

[31] R. S. Alwitt, C. K. Dyer and B. Noble, J. Electrochem. Soc., **129**, 711, (1982).

[32] Y. Jia, H. Zhou, P. Luo, S. Luo, J. Chen and Y. Kuang, Surf. Coat. Technol., **201**, 513, (2006).

[33] O. Jessensky, F. Müller and U. Gösele, J. Electrochem. Soc., **144**, 3735, (1998).

[34] H. Masuda, F. Hesegwa and S. Ono, J. Electrochem. Soc., **144**, 127, (1997).

[35] A. P. Li, F. Müller, A. Birner, K. Nielsch and U. Gösele, J. Vac. Sci. Technol. A, **17**, 1428, (1999).

[36] H. Masuda, K. Yada and A. Osaka, Jpn. J. Appl. Phys., **37**, 1340, (1998).

[37] S. Shingubara, O. Okino, Y. Sayama, H. Sakaue and T. Takahagi, Jpn. J. Appl. Phys., **36**, 7791, (1997).

[38] S. Ono, M. Saito, M. Ishiguro and H. Asoh, J. Electrochem. Soc., **151**, 473, (2004).

[39] K. Ebihara, H. Takahashi and M. Nagayama, J. Met. Finish. Soc. Japan (Kinzoku Hyomen Gijustu), **34**, 548, (1983).

[40] K. Ebihara, H. Takahashi and M. Nagayama, J. Met. Finish. Soc. Japan (Kinzoku Hyomen Gijustu), **33**, 156, (1982).

[41] K. Nielsch, J. Choi, K. Schwirn, R. B. Wehrspohn and U. Gösele, Nano Lett., **2**, 677, (2002).

[42] G. D. Sulka and K. G. Parkoia, Electrochim. Acta, **52**, 1880, (2007).

[43] S. Wernick, R. Pinner and P. G. Sheasby, ASM International, Finishing Publication Ltd., 5th edition, *The surface treatment and finishing of aluminum and its alloys*, 289, (1987).

[44] W. Lee, R. Ji, U. Gösele and K. Nielsch, Nature Mat., **5**, 741, (2006).

[45] S. Ono and N. Masuko, Surf. Coat. Technol., 139-142, 169-170, (2003).

[46] S. Ono, H. Asoh, M. Saito and M. Ishiguro, Electrochemistry, (in Japanese), **71**, 105, (2003).

[47] P. Bocchetta, C. Sunseri, A. Bottino, G. Capannelli, G. Chiavarotti, S. Piazza and F. Di Quarto, J. Appl. Electrochem., **32**, 977, (2002).

[48] L. M. Liz-Marzan, Materials, **7**, 26, (2004).

[49] S. Link and M. A. El-Sayed, Annu. Rev. Phys. Chem., **54**, 331, (2004).

[50] S. Padovani, C. Sada, P. Mazzoldi, BG. Brunetti, I. Borgia, A. Sgamellotti, A. Giulivi, F. d'Acapito and G. Battaglin, J. Appl. Phys., **93**, 10058, (2003).

[51] M. Faraday, Philos. Trans. R. Soc. London, **147**, 145, (1857).

[52] K. E. Sapsford, L. Berti and I. L. Medintz, Angew. Chem. Int. Ed., **45**, 4562, (2006).

[53] C. F. Bohren and D. R. Huffman, *Absorption and scattering of light by small particles*, New York: Wiley, (1983).

[54] T. Klar, M. Perner, S. Grosse, G. Von Plessen, W. Spirkl and J. Feldmann, Phys. Rev. Lett., **80**, 4249, (1998).

[55] R. H. Ritchie and H. B. Eldridge, Phys. Rev., **126**, 1935, (1962).

[56] W. L. Barnes, J. Opt. A: Pure Appl. Opt., **8**, 87, (2006).

[57] E. Kretschmann, Z. Phys. **241**, 213, (1971).

[58] K. L. Kelly, E. Coronado, L. L. Zhao and G. C. Schatz, J. Phys. Chem. B, **107**, 668, (2003).

[59] U. Kreibig and C. V. Fragstein, Z. Physik, **224**, 307, (1969).

[60] S. Link and M. A. El-Sayed, Int. Rev. Phys. Chem., **19**, 409, (2000).

[61] S. Link and M. A. El-Sayed, J. Phys. Chem. B, **103**, 4212, (1999).

[62] S. Nie and S. R. Emory, Science, **275**, 1102, (1997).

[63] K. Kneipp, Y. Wang, H. Kneipp, L. T. Perelman, I. Itzkan, R. R. Dasari and M. S. Feld, Phys. Rev. Lett., **78**, 1667, (1997).

[64] S. Neretina, W. Qian, E. Dreaden, M. El-sayed, R. A. Hughes, J. S. Preston and P. Mascher, Nano Lett., **8**, 2410, (2008).

[65] G. V. Hartland, M. Hu, O. Wilson, P.Mulvaney and J. E. Sader, J. Phys. Chem. B, **106**, 743, (2002).

[66] W. Huang, W. Qian and M. A. El-Sayed, Nano Lett., **4**, 1741, (2004).

[67] W. Huang, W. Qian and M. A. El-Sayed, J. Phys. Chem. C, **109**, 18881, (2005).

[68] G. Mie, Ann. Phys., **25**, 377, (1908).

[69] N. W. Ashcroft and N. D. Mermin, Solid state Physics, *Saunders College, Philadelphia, PA 19105*, (1976).

[70] N. L. Rosi and C. A. Mirkin, Chem. Rev., **105**, 1547, (2005).

[71] J. M. Bruchez, M. Moronne, P. Gin, S. Weiss and S. P. Alivisatos, Science, **281**, 2013, (1998).

[72] M. M. Alvarez, J. T. Khoury, G. Schaaff, M. N. Shafigullin, I. Vezmar and R. L. Whetten, J. Phys. Chem. B, **101**, 3706, (1997).

[73] P. K. Jain, *Plasmons in Assembled metal nanostructures: Radiative and nonradiative properties, near-field coupling and its universal scaling behavior*, Ph.D thesis, (2008).

[74] V. N. Pustovit and T. V. Shahbazyan, J. Opt. Soc. Am. A, **23**, 1369, (2006).

[75] J. Turkevich, P. C. Stevenson and J. Hillier, Discuss. Faraday Soc., **11**, 55, (1951).

[76] S. Link, M. B. Mohamed and M. A. El-Sayed, J. Phys. Chem. B, **103**, 3073, (1999). Erratum: J. Phys. Chem. B, **109**, 10531, (2005).

[77] N. R. Jana, L. Gearheart and C. J. Murphy, Langmuir, **17**, 6782, (2001).

[78] N. R. Jana, L. Gearheart and C. J. Murphy, J. Adv. Mater, **13**, 1389, (2001).

[79] B. Nikoobakht and M. A. El-Sayed, Chem. Mater., **15**, 1957, (2003).

[80] E. Hao and C. Schatz George, J. Chem. Phys., **120**, 357, (2004).

[81] J. C. Hulteen and R. P. Van Duyne, J. Vac. Sci. Technol. A, **13**, 1553, (1995).

[82] R. Resnick and R. Eisberg, *Quantum physics of atoms, molecules, solids, nuclei and particles (2nd Edition)*, John Wiley&Sons, (1985).

[83] M. R. Roussel, *Molecular energy levels*, (2009).

[84] A. Treibs and F. H. Kreuzer, Justus Liebigs Ann. Chem., **718**, 208, (1968).

[85] BODIPY Dye Series, life technologies. *http://de-de.invitrogen.com/site/de/de/home/References/Molecular-Probes-The-Handbook/Fluorophores-and-Their-Amine-Reactive-Derivatives/BODIPY-Dye-Series.html*, opened on 19th, June, 2012.

[86] K. E. Beatty, J. Szychowski, J. D. Fisk and D. A. Tirrell, *A BODIPY-cyclooctyne for protein imaging in live cells*, ChemBioChem, **12**, (14), 2137, ISSN 1439-4227.

[87] P. Bandhuvula, Z. Li, R. Bittman and J. D. Saba, Biochemical and Biophysical Research Comm., **380**, 366, (2009).

[88] G. Sathyamoorthi, M. L. Soong, T. W. Ross and J. H. Boyer, Heteroat. Chem., **4**, 603, (1993).

[89] S. O. McDonnell and D. F. O'Shea, Org. Lett., **8**, 3493, (2006).

[90] W. Zhao and E. M. Carreira, Angew. Chem., Int. Ed., **44**, 1677, (2005).

[91] A. Loudet and K. Burgess, Chem. Rev., **107**, 4891, (2007).

[92] T. E. Wood and A. Thompson, Chem. Rev., **107**, 1831, (2007).

[93] S. Hattori, K. Ohkubo, Y. Urano, H. Sunahara, T. Nagano,Y. Wada, N. V. Tkachenko, H. Lemmetyinen and S. Fukuzumi, J. Phys. Chem. B, **109**, 15368, (2005).

[94] D. Kumaresan, R. Thummel, T. Bura, G. Ulrich and R. Ziessel, Chem.-Eur. J., **15**, 6335, (2009).

[95] T. Rousseau, A. Cravino, T. Bura, G. Ulrich, R. Ziessel and J. Roncali, Chem. Commun., 1673, (2009).

[96] F. De Angelis, S. Fantacci and R. Gebauer, J. Phys. Chem. Lett., **2**, 813, (2011).

[97] J. Meyer, A. Wadewitz, Lokamani, C. Toher, R. Gresser, K. Leo, M. Riede, F. Moresco and G. Cuniberti, Phys. Chem. Chem. Phys., **13**, 14421, (2011).

[98] F. S. Tautz, Prog. Surf. Sci., **82**, 479, (2007).

[99] F. Pump, R. Temirov, O. Neucheva, S. Soubatch, S. Tautz, M. Rohlfing and G. Cuniberti, Appl. Phys. A: Mater. Sci. Process., **93**, 335, (2008).

[100] H. D. Yan, P. Lemmens, H. Dierke, S. C. White, F. Ludwig and M. Schilling, J. of Phys.: Conference series, **145**, 012079, (2009).

[101] W. Lee, R. Ji, U. Gösele and K. Nielsch, Nature Materials, **5**, 741, (2006)

[102] A. Eftekhari, *Nanostructured Materials in Electrochemistry*, Wiley-VCH, ISBN: 978-3-527-31876-6

[103] Ch. Brändli, T. F. Jaramillo, A. Ivanovskaya and E. W. McFarland, Electrochim. Acta, **47**, 553, (2001).

[104] L. Ba and W. S. Li, J. Phys. D: Appl. Phys., **33**, 2527, (2000).

[105] L. E. Rehn, B. J. Kestel, P. M. Baldo, J. Hiller, A. W. Mccormick and R. C. Birchter, Nuc. Instrum. Meth. Phys. Res. B, **206**, 490, (2003).

[106] T. Xu, G. Zangari and R. M. Metzger, Nano Lett. **2**, 37, (2002).

[107] A. P. Li, F. Müller, A. Birner, K. Nielsch and U. Gösele, J. Appl. Phys., **84**, 6023, (1998).

[108] M. Theodoropoulou, P. K. Karahaliou, S. N. Georgia, C. A. Krontiras, M. N. Pisanias, M. Kokonou and A. G. Nassiopoulou, Ionics, **11**, 236, (2005).

[109] E. P. Briggs, A. R. Walpole, P. R. Wilshaw, M. Karlsson and E. Palsgard, J. Mater. Sci. Mater. Med., **15**, 1021, (2004).

[110] K. Yasui, Y. Sakamoto, K. Nishio and H. Masuda, Chem. Lett., **34**, 342, (2005).

[111] K. Y. Choi and P. Lemmens, *Scattering: Inelastic Scattering Technique - Raman*, (2004).

[112] D. J. Gardiner, *Practical Raman spectroscopy*, (1989).

[113] H. Temkin, G. J. Dolan, M. B. Oanish and N. G. Chu, Appl. Phys. Lett., **50**, 413, (1987).

[114] H. G. Craighead and G. A. Niklasson, Appl. Phys. Lett., **44**, 1134, (1984).

[115] T. Sato, K. Himura, M. Shirai, K. Tominaga, K. Haraguchi, T. Katsuyama and T. Shimada, Appl. Phys. Lett., **66**, 159, (1995).

[116] J. G. Wan, X. W. Wang, Y. J. Wu, M. Zeng, Y. Wang, H. Jiang, W. Q. Zhou, G. H. Wang and J. M. Liu, Appl. Phys. Lett., **86**, 122501, (2005).

[117] H. Zheng, J. Wang, S. E. Lofland, Z. Ma, L. Mohaddes-Ardabili, T. Zhao, L. Salamanca-Riba, S. R. Shinde, S. B. Ogale, F. Bai, D. Viehland, Y. Jia, D. G. Schlom, M. Wuttig, A. Roytburd and R. Ramesh, Science, **303**, 661, (2004).

[118] J. T. Hu, T. W. Odom and C. M. Lieber, Acc. Chem. Res., **32**, 435, (1999).

[119] J. S. Jung, J. H. Lim, K. H. Choi, S. L. Oh, Y. R. Kim, S. H. Lee, D. A. Smith, K. L. Stokes, L. Malkinski and C. J. O'Connor, J. Appl. Phys., **10**, 97, (2005).

[120] G. B. Ji, S. L. Tang, B. L. Xu, B. X. Gu and Y. W. Du, Chem. Phys. Lett., **379**, 484, (2003).

[121] M. Steinhart, J. H. Wendorff, A. Greiner, R. B. Wehrspohn, K. Nielsch, J. Schilling, J. Choi and U. Gösele, Science, **296**, 1997, (2002).

[122] Y. Luo, I. Szafraniak, N. D. Zakharov, V. Nagarajan, M. Steinhart, R. B. Wehrspohn, J. H. Wendorff, R. Ramesh and M. Alexe, Appl. Phys. Lett., **83**, 440, (2003).

[123] B. A. Hernandez, K. S. Chang, E. R. Fisher and P. K. Dorhout, Chem. Mater., **14**, 480, (2003).

[124] S. Aravamudhan, N. S. Ramgir and S. Bhansali, Sensor and Actuators B: Chemical, **127**, 29 (2009).

[125] L. Liu, W. Lee, Z. Huang, R. Scholz and U. Gösele, Nanotechnology, **19**, 335604 (2008).

[126] L. P. Carignan, C. Lacroix, A. Ouimet, M. Ciureanu, A. Yelon and D. Menard, J. Appl. Phys., **102**, 023905, (2007).

[127] H. Masuda, T. Yanagishita, K. Yasui, K. Nishio, I. Yagi, T. N. Rao and A. Fujishima, Adv. Mater., **13**, 247, (2001).

[128] H. D. Yan, P. Lemmens, D. Wulferding, J. Shi, K. D. Becker, C. Lin, A. Lak and M. Schilling, J. Mat. Chem. Phys., **135**, 206, (2012).

[129] A. Makhal, S. Sarkar, H. D. Yan, D. Wulferding, F. Cetin, P. Lemmens and S. K. Pal, Nanotechnology, (submitted), 2012.

[130] Y. Du, W. L. Cai, C. M. Mo, J. Chen, L. D. Zhang and X. G. Zhu, Appl. Phys. Lett., **74**, 2951, (1999).

[131] G. S. Huang, X. L. Wu, L. W. Yang, X. F. Shao, G. G. Siu and P. K. Chu, Appl. Phys. A: Mater. Sci. Process., **81**, 1345, (2005).

[132] T. Gao, G. W. Meng and L. D. Zhang, J. Phys: Cond. Matter, **15**, 2071, (2003).

[133] X. Y. Sun, F. Q. Xu, Z. M. Li and W. H. Zhang, J of Luminesc., **121**, 588, (2006).

[134] P. Drude, *Zur Elektronentheorie der metalle*, **306 (3)**, 566, (1900).

[135] J. M. Pitarke, V. M. Silkin, E. V. Chulkov and P. M. Echenique, Rep. Prog. Phys., **70**, (2007).

[136] Z. Gueroui and A. Libchaber, Phys. Rev. Lett., textbf93, 166108, (2004).

[137] T. Pons, I. L. Medintz, K. E. Sapsford, S. Higashiya, A. F. Grimes, D. S. English and H. Mattoussi, Nano Lett., **7**, 3157, (2007).

[138] M. E. Nasir and B. Hamilton, J. Phys. D: Appl. Phys., **42**, 195404, (2009).

[139] P. Kizler, J. He, D. R. Clarke and P. R. Kenway, J. Am. Ceram. Soc., **79**, 3, (1996).

[140] X. Sun, F. Xu, Z. Li and W. Zhang, J. of Luminescence, **121**, 588, (2006).

[141] K. J. Caulfield, R. Cooper and J. F. Boas, Phys. Rev. B, **47**, 55, (1993).

[142] P. W. Levy, Phys. Rev., 123, 1226, (1961).

[143] E. W. J. Mitchell, J. D. Rigden and P. W. Townsend, Phil. Mag., **5**, 1013, (1960).

[144] B. J. Jeffries, J. D. Brewer and G. P. Summers, Phys. Rev. B, **24**, 6074, (1981).

[145] J. W. Diggle, T. C. Downie and C. W. Goulding, Chem. Rev. (Washington, DC), **69**, 365, (1969).

[146] C. Cherki and J. Siejka, J. Electrochem. Soc., **120**, 784, (1973).

[147] J. Siejka and C. Ortega, J. Electrochem. Soc., **124**, 883, (1977).

[148] V. P. Parkhutik and V. I. Shershulsky, J. Phys. D: Appl. Phys., **25**, 1258, (1992).

[149] B. D. Evans and M. Stapelbroek, Phys. Rev. B, **18**, 7089, (1978).

[150] G. J. Pogatshnik, Y. Chen and B. D. Evans, IEEE Trans. Nucl. Sci., **34**, 1709, (1987).

[151] T. V. Perevalov, O. E. Tereshenko, V. A. Gritsenko, V. A. Pustovarov, A. P. Yelisseyev, C. Park, J. H. Han and C. Lee, J. Appl. Phys., **108**, 013501, (2010).

[152] A. Stashans, E. Kotomin and J. -L. Calais, Phys. Rev. B, **49**, 14854, (1994).

[153] V. A. Pustovarov, T. V. Perevalov, V. A. Grisenko, T. P. Smirnova and A. P. Yelisseyev, Thin Solid Films, **519**, 6319, (2011).

[154] A. I. Surdo, V. S. Kortov, V. A. Pustovarov and V. Yu. Yakovlev, Phys. Status Solidi. C, **2**, 527, (2005).

[155] H. Momida, T. Hamada, Y. Takagi, T. Yamamoto, T. Uda and T. Ohno, Phys. Rev. B, **73**, 054108, (2006).

[156] J. Carrasco, J. R. B. Gomes and F. Illas, Phys. Rev. B, **69**, 064116, (2004).

[157] J. Carrasco, N. Lopez, C. Sousa and F. Illas, Phys. Rev. B, **72**, 054109, (2005).

[158] B. D. Evans, J. Nucl. Mater., **219**, 202, (1995).

[159] K. H. Lee and J. H. Crawford, Jr., Appl. Phys. Lett., **33**, 274, (1978).

[160] Z. Gueroui and A. Libchaber, Phys. Rev. Lett., **93**, 166108, (2004).

[161] A. Ya. Dan'ko, N. S. Sidel'nikova, G. T. Adonkin, A. T. Budnikov, S. V. Nizhankovskii and S. I. Krivonogov, Cryst. Reports, **49**, 240, (2004).

[162] M. E. Nasir and B. Hamilton, J. Phys. D: Appl. Phys., **42**, 195404, (2009).

[163] P. Lodahl, A. P. Mosk and A. Lagendijk, Phys. Rev. Lett., **95**, 173901, (2005).

[164] D. S. Wiersma, P. Bartolini, A. Lagendijk and R. Righini, Nature, **390**, 671, (1997).

[165] J. C. Pivin, N. V. Gaponenko, I. Molchan, R. Kudrawiec, J. Misiewicz, L. Bryja, G. E. Thompson and P. Skeldon, J. Alloys. Compd., **341**, 272, (2002).

[166] I. Molchan, N. V. Gaponenko, R. Kudrawiec, J. Misiewicz and G. E. Thompson, Mater. Sci. Eng. B, **105**, 37, (2003).

[167] Y. Zhao, D. Yang, C. Zhou, Q. Yang and D. Que, J. Lumin., **105**, 57, (2003).

[168] T. P. Nguyena, S. H. Yanga, P. L. Rendua and H. Khan, Compos. Part A-Appl. S., **105**, 37, (2003).

[169] F. Rumiche, H. H. Wang, W. S. Hu, J. E. Indacochea and M. L. Wang, Sens. Acuators B: Chem., **134**, 869, (2008).

[170] H. Masuda, M. Ohya, H. Asoh, M. Nakao, M. Nohtomi and T. Tamamura, Jpn. J. Appl. Phys., **38**, L1403, (1999).

[171] A. Aguilera, V. Jayaraman, S. Sanagapalli, R. S. Singh, V. Jayaraman, K. Sampson and V. P. Singh, Sol. Energy Mater. Sol. Cells, **90**, 713, (2006).

[172] K. Nielsch, R. B. Wehrpohn, J. Barthel, J. Kirschner, U. Gösele, S. F. Fischer and H. Kronmuller, Appl. Phys. Lett.,**79**, 1360, (2001).

[173] J. Hua, J. H. Tiana, J. Shia, F. Zhanga, D. L. Heb, L. Liuc, D. J. Jungc, J. B. Baib and Y. Chen, Microelectron. Eng., **88**, 1714, (2001).

[174] S. Simovic, D. Losic and K. Vasilev, Chem. Commun., **46**, 1317, (2010).

[175] C. R. Martin, Science, **266**, 1961, (1994).

[176] G. Shi, C. M. Mo, W. L. Cai and L. D. Zhang, Solid State Commun., **115**, 253, (2000).

[177] R. Jia, Y. Shen, H. Luo, X. Chen, Z. Hu and D. Xue, Appl. Surface Sci., **233**, 343, (2004).

[178] C. Burda, T. C. Green, S. Link and M. A. El-Sayed, J. Phys. Chem. B, **103**, 1783, (1999).

[179] Y. X. Liu, M. A. Summers, S. R. Scully and M. D. McGehee, J. Appl. Phys., **99**, 093521, (2006).

[180] S. Lu and A. Madhukar, Nano Lett., **7**, 3443, (2007).

[181] Y. Yang, W. Rodríguez-Córdoba, X. Xiang and T. Lian, Nano Lett., **12**, 303, (2012).

[182] C. S. Yun, A. Javier, T. Jennings, M. Fisher, S. Hira, S. Peterson, B. Hopkins, N. O. Reich and G. F. Strouse, J. Am. Chem. Soc., **127**, 3115, (2005).

[183] J. R. Lakowicz, *Principles of Fluorescence Spectroscopy; 2nd ed.*, Kluwer Academic/ Plenum Publishers,: New York, (1999).

[184] S. E. Braslavsky, E. Fron, H. B. Rodriguez, E. S. Roman, G. D. Scholes, G. Schweitzer, B. Valeur and J. Wirz, **7**, J. Photochem. Photobiol. Sci., 1444, (2008).

[185] W. W. Yu, L. Qu, W. Guo and X. Peng, Chem. Mater., **15**, 2854, (2003).

[186] P. K. Jain, K. S. Lee, I. H. El-Sayed and M. A. El-Sayed, J. Phys. Chem. B, **110**, 7238, (2006).

[187] X. Y. Sun, F. Q. Xu, Z. M. Li and W. H. Zhang, J. of Luminesc., **121**, 588, (2006).

[188] A. Makhal, S. Sarkar, T. Bora, S. Baruah, J. Dutta, A. K. Raychaudhuri and S. K. Pal, J. Phys. Chem. C, **114**, 10390, (2010).

[189] Y. Lou, X. Chen, A. C. Samia and C. Burda, J. Phys. Chem. B, **107**, 12431, (2003).

[190] A. Makhal, H. Yan, P. Lemmens and S. K. Pal, J. Phys. Chem. C, **114**, 627, (2010).

[191] R. M. Clegg, Methods Enzyoml., **211**, 353, (1992).

[192] D. M. J. Lilley and T. J. Wilson, Curr. Opin. Chem. Biol., **4**, 507, (2000).

[193] A. Makhal, S. Sarkar, T. Bora, S. Baruah, J. Dutta, A. K. Raychaudhuri and S. K. Pal, Nanotechnology, **21**, 265703, (2010).

[194] S. Sarkar, A. Makhal, T. Bora, S. Baruah, J. Dutta, A. K. Raychaudhuri and S. K. Pal, Phys. Chem. Chem. Phys., **13**, 12488, (2011).

[195] M. Montalti, N. Zaccheroni, L. Prodi, N. O'Reilly and S. L. James, J. Am. Chem. Soc., **129**, 2418, (2007).

[196] B. N. J. Persson and N. D. Lang, Phys. Rev. B, **26**, 5409, (1982).

[197] J. Gersten and A. Nitzan, J. Chem. Phys., **75**, 1139, (1981).

[198] M. A. H. muhammed, A. K. Shaw, S. K. Pal and T. Pradeep, J. Phys. Chem. C, **112**, 14324, (2008)

[199] T. Li, S. G. Yang, L. S. Huang, J. R. Zhang, B. X. Gu and Y. W. Du, J. Phys.: Condens. Matter, **16**, 2463, (2004).

[200] S. P. S. Porto and R. S. Krishnan, J. Chem. Phys., **47**, 1009, (1967).

[201] S. H. Shin, F. H. Pollak and P. M. Raccah, *in Proceedings of 3rd International Conference on Light Scattering in Solids*, Paris, 401, (1975).

[202] J. E. Millstone, S. Park, K. L. Shuford, L. Qin, G. C. Schatz and C. A. Mirkin, J. Am. CHem. Soc. **127**, 5312, (2005).

[203] K. H. Su, Q. H. Wei, X. Zhang, J. J. Mock, D. R. Smith and S. Schultz, Nano Lett., **3**, 1087, (2003).

[204] S. Lin, M. Li, E. Dujardin, C. Girard and S. Mann, Adv. Mater., **17**, 2553, (2005).

[205] A. A. Lazarides and G. C. Schatz, J. Phys. Chem. B., **104**, 460, (2000).

[206] H. Yan, P. Lemmens, J. Ahrens, M. Bröring, S. Burger, W. Daum, G. Lilienkamp, S. Korte, A. Lak and M. Schilling, Acta Phys. Sinica, (submitted), (2012).

[207] P. R. Evans, G. A. Wurtz, R. Atkinson, W. Hendren, D. O'Connor, W. Dickson, R. J. Pollard and A. V. Zayats, J. Phys. Chem. C, **111**, 12522, (2007).

[208] G. A. Wurtz, W. Dickson, D. O'Connor, R. Atkinson, W. Hendren, P. Evans, R. Pollard and A. V. Zayats, Optics Express, **16**, 7460, (2008).

[209] J. J. Storhoff, A. A. Lazarides, R. C. Mucic, C. A. Mirkin, R. L, Letsigner and G. C. Schatz, J. Am. Chem. Soc., **122**, 4640, (2000).

[210] J. Aizpurua, G. W. Bryant, L. J. Richter, F. J. Garcia de Abajo, B. K. Kelley and T. Mallouk, Phys. Rev. B., **71**, 235421, (2005).

[211] K. H. Su, Q. H. Wei, X. Zhang, J. J. Mock, D. R. Smith and S. Schultz, Nano Lett., **3**, 1087, (2003).

[212] S. W. Prescott and P. Mulvaney, J. Appl. Phys., **99**, 123504, (2006).

[213] J. J. Xiao, J. P. Huang and K. W. Yu, Phys. Rev. B, **71**, 045404, (2005).

[214] P. K. Jain, W. Huang and M. A. El-Sayed, Nano Lett., **7**, 2080, (2007).

[215] O. Valdes-Aguilera and D. C. Neckers, Acc. Chem. Res., **22**, 171, (1989).

[216] M. Kasha, Radiat. Res., **20**, 55, (1960).

[217] M. Kasha, H. R. Rawls and M. A. El-Bayoumi, Pure Appl. Chem., **11**, 371, (1965).

[218] B. Z. Packard, D. D. Toptygin, A. Komoriya and L. Brand, Phys. Chem. B, **102**, 752, (1998).

[219] P. K. Jain, S. Eustis, M. A. El-Sayed, J. Phys. Chem. B, **110**, 18243, (2006).

[220] S. K. Ghosh, S. Nath, S. Kundu, K. Esumi and T. Pal, J. Phys. Chem. B, **108**, 13963, (2004).

[221] G. Papavassiliou, Solid state Chem., **12**, 185, (1980).

[222] M. A. Gonzalez-Martinez, R. Puchades and A. Maquieira, Analytical and Bioanalytical Chemistry, **387**, 205, (2007).

[223] A. Rasooly and K. E. Herold, Journal of Aoac International, **89**, 873, (2006).

[224] T. Vo-Dinh and B. Cullum, Fresenius Journal of Analytical Chemistry, **366**, 540, (2000).

[225] T. Liebermann and W. Knoll, Colloids and surfaces A - Physicochemical and Engineering Aspects, **171**, 115, (2000).

[226] S. Ekgasit, F. Yu and W. Knoll, Sensors and Actuators B, **104**, 294, (2005).

[227] K. Matsubara, S. Kawata and S. Minami, Optics Letters, **15**, 75, (1990).

[228] F. C. Chien and S. J. Chen, Optics Letters, **31**, 187, (2006).

[229] J. Dostalek, P. Adam, P. Kvasnicka, O. Telezhnikova and J. Homola, Optics Letters, **32**, 2903, (2007).

[230] P. Yang, G. Wimsberger, H. C. Huang, S. R. Cordero, B. Scott, M. D. Mcgehee, T. Deng, G. M. Whitesides, G. F. Chmelka, S. K. Buratto and G. D. Stucky, Science, **287**, 465, (2000).

[231] M. Ganschow, M. Wark, D. Weohrle and Schulz-Ekloff, Angew. Chem. Int. Ed., **39**, 161, (2000).

[232] G. Wirnsberger and G. D. Stucky, Chem. Phys. Chem., **1**, 89, (2000).

[233] C. T. Kresge, M. E. leonowicz, W. J Roth and J. S. Beck, Nature, **359**, 710, (1999).

[234] T. D. Neal, K. Okamoto and A. Scherer, Optic. Exp., **13**, 5522, (2005).

[235] S. Kalele, A. C. Deshpande, S. B. Singh and S. K. Kulkarni, Bull. Mater. Sci., **31**, 541, (2008).

[236] Y. Jiang, H. Y. Wang, H. Wang, B. R. Gao, Y. W. Hao, Y. Jin, Q. D. Chen and H. B. Sun, J. Phys. Chem. C, **115**, 12636, (2011).

[237] T. Enokida and R. Hirohashi, J. Imaging Sci. Technol., **35**, 235, (1991).

[238] S. Tsuchiya, A. Omote, M. Murakami and S. Yoshimura, J. Imaging Sci. Technol., **39**, 294, (1995).

[239] H. Du, R. A. Fuh, J. Li, A. Corkan and J. S. Lindsey, Photochem. Photobiol., **68**, 141, (1998).

[240] J. M. Dixon, M. Taniguchi and J. S. Lindsey, Photochem. Photobiol., **81**, 212, (2005).

[241] A. N. Terenin, Nauka, Leningrade (In Russian), 616, (1967).

[242] G. P. Gurinovich, A. N. Sevchenko and K. N. Solov'ev, Nauka i Tekhnika, Minsk (In Russian), Minsk, (1968).

[243] A. P. Alivisatos, K. P. Johnsson, X. Peng, T. E. Wilson, C. J. Loweth, M. P. Bruchez and P. G. Schultz, Nature, **382**, 609, (1996).

[244] C, Sönnichsen, B. M. Reinhard, J. Liphardt and S. P. Alivisatos, Nat. Biotechnol., **23**, 741, (2005).

[245] K. Y. Yang, K. C. Choi and C. W. Ahn, App. Phys. Lett., **94**, 173301, (2009).

[246] K. Okamoto, I. Niki, A. Scherer, Y. Narukawa, T. Mukai and A. Scherer, Nature Mater., **3**, 601, (2004).

[247] H. J. Park, D. Vak, Y. Y. Noh, B. Lim and D. Y. Kim, Appl. Phys. Lett., **90**, 161107, (2007).

[248] P. Anger, P. Bharadwaj and L. Novotny, Phys. Rev. Lett., **96**, 113002, (2006).

[249] Y. Kang, K. J. Erickson and T. A. Taton, J. Am. Chem. Soc., **127**, 13800, (2005).

[250] G. Wang, R. W. Murray, Nano Lett., **4**, 95, (2004).

[251] T. Rousseau, A. Cravino, T. Bura, G. Ulrich, R. Ziessel, J. Roncali, Chemical Communications, 1673, (2009).

[252] B. Kim, B. W. Ma, V. R. Donuru, H. Y. Liu, J. M. J. Frechet, Chemical communications, **46**, 4148, (2010).

[253] G. P. Wiederrecht, G. A. Wurtz and J. Hranisavljevic, Nano Letters, **4, No. 11,** 2121, (2004).

[254] G. A. Wurtz, P. R. Evans, W. Hendren, R. Atkinson, W. Dickson, R. J. Pollard and A. V. Zayats, Nano Letters, **7, No. 5,** 1297, (2007).

Acknowledgements

My work at the Institute for Condensed Matter Physics (Institut für Physik der Kondensierten Materie, IPKM), TU Braunschweig has benefitted from many collaborations, important discussions and a friendly environment.

First and foremost, I am cordially thankful to my advisor Prof. Peter Lemmens, whose encouragement and guidance has supported me in developing this very interesting topic since he took me into his group. He also taught me how to appreciate research and science, to have an open vision, to think independently, and to communicate ideas. Prof. Lemmens has always welcomed scientific discussions and supported my pursuit both experimentally and theoretically. Without his support, none of this work would have been possible.

I would like to thank all my current and past colleagues: Dirk Wulferding, Fatih Cetin, Katharina Schnettler, Dr. Pushpendra Kumar, Seth White, Dr. Viorel Felea, Johannes Dühn, Anshuma Pathak, and Ingrid Ringler for accommodating me and creating an excellent atmosphere for research and learning. I thank Dirk Wulferding for his help with Raman measurements and his valuable advice in my research and study. I have had many helpful discussions with our guests Dr. Vladimir Gnezdilov, Prof. Yurii Pashkevich, Prof. Kwang-Yong Choi, and Dr. Manash Kumar Ghosh. I have also benefited from Dr. Dirk Menzel, Prof. Jochen Littest, Prof. Stefen Süllow, Manuela Bosse, Dr. Dezhen Li for the last five years. I am also grateful to the help from our workshop and technical colleagues, Tilo Lampe, Lutz Nagatz, Arno Ellermann.

I thank Prof. Martin Bröring, Prof. Klaus-Dieter Becker, Dr. Jianmin Shi, Johannes Ahrens, and Katharina Schartz for the absorption spectra measurements, and with whom I have learnt the chemistry and molecular knowledge. I thank Dr. Samir Kumar Pal from SNBC, Kolkata, India for the picosecond and femtosecond PL measurements. I thank Dr. Chengtian Lin, MPI-Stuttgart for the XRD measurements.

In addition, I would like to thank Prof. Winfried Daum, Dr. Gerhard Lilienkamp, Sandra Korte, TU Clausthal for Auger spectroscopy, Prof. Andreas Hangleiter, Lars Hoffmann, Dr. Hanno Dierke for transmission electron microscopy, Prof. Meinhard Schilling, Dr. Frank Ludwig, and Aidin Lak, TU-BS for scanning electron microscopy, Prof. Karina Morgenstern and Fatih Kalkan, LU-Hannover for scanning tunneling microscopy, and Prof. Herbert Pfnür, Ulrich Krieg, Jens Baringhaus, LU-Hannover as well as Prof. Andreas Waag, Stephan

Merzsch, Doris Rümmler and Prof. Marc Tornow, and Anshuma Pathak, IHT, TU Braunschweig for thin metallic layer deposition.

Important discussions and help came from Prof. Bernd Güttler, PTB, and Dr. Lifeng Liu, MPI for Microstructures, Halle. I am thankful to Dr. Sven. Burger, Konrad-Zuse-Zentrum für Informationstechnik, Berlin for introducing me to plasmon simulation.

Our work was supported by the International Graduate School of Metrology (IGSM) and the NTH School for Contacs in Nanosystems at Braunschweig, Clausthal and Hannover.

Last but not the least, I would like to thank my parents, who gave me an excellent upbringing and support for my study in Germany, and my husband Bianying Song for his continuing support and limitless patience.